STRATEGIES FOR SOLAR SAIL MISSION DESIGN IN THE CIRCULAR RESTRICTED THREE-BODY PROBLEM

A Thesis

Submitted to the Faculty

of

Purdue University

by

Allan I. S. McInnes

In Partial Fulfillment of the

Requirements for the Degree

of

Master of Science in Engineering

August 2000

Dedicated to the memory of Robert A. Heinlein.

Here he lies where he longed to be,
Home is the sailor, home from sea,
And the hunter home from the hill.
- Robert Louis Stevenson

ACKNOWLEDGMENTS

The research that I have been conducting for past two years, under the direction of Professor Kathleen C. Howell, has been, at different times, challenging, frustrating, and exhilarating. I would like to thank Professor Howell for her guidance, in both the direction of my research and the direction of my career, as well has for her seemingly infinite patience. I am extremely grateful for being given the opportunity to work with her, and for the time and effort she has devoted to my graduate education.

I would also like to thank the other members of my graduate committee, Professors James M. Longuski, and John J. Rusek, for their interest and input.

The members of my research group (Belinda, Brian, Eric, Jason, Jin Wook, José, and Mark), have given me assistance, support, and friendship. For this I thank them, and wish them the best of luck wherever their careers take them.

The writings of Robert A. Heinlein have, throughout my life, provided inspiration, motivation, and education. Sadly, Mr. Heinlein passed away before I could thank him personally for all he has done.

Through all of my endeavors, both past and present, my parents have encouraged, supported, and guided me. My parents gave me the desire to set myself goals worth achieving, and the education with which to achieve those goals. I am eternally grateful for all that they have done for me.

I am also grateful for the financial support provided to me by Purdue University. This support has come in the form of a Frederick N. Andrews Fellowship, and a Warren G. Koerner Fellowship. These fellowships have assisted greatly in allowing me to pursue a graduate education.

TABLE OF CONTENTS

Page

Page

LIST OF TABLES

LIST OF FIGURES

ABSTRACT

McInnes, Allan I. S., M.S.E., Purdue University, August, 2000. Strategies for Solar Sail Mission Design in the Circular Restricted Three-Body Problem. Major Professor: Dr. Kathleen C. Howell.

The interaction between the naturally rich dynamics of the three-body problem, and the "no-propellant" propulsion afforded by a solar sail, promises to be a useful one. This dynamical interaction is explored, and several methods for incorporating it into mission designs are investigated. A set of possible "artificial" libration points is created by the introduction of a solar sail force into the dynamical model represented in the three-body problem. This set is split into two subsets: the on-axis libration points, lying along the Sun-Earth axis; and a complementary set of off-axis libration points. An analytical approximation for periodic motion in the vicinity of the on-axis libration points is developed, and then utilized as an aid in exploring the dynamics of the new halo families that result when a solar sail force is exploited. The changing shape and stability of these new halo families is investigated as the level of thrust generated by a sail is increased. A stationkeeping algorithm is then developed to maintain a spacecraft in the vicinity of a nominal halo orbit using changes in the solar sail orientation. The off-axis libration points are determined to be generally unstable, and lacking first order periodic solutions. Thus, variations in the orientation of the solar sail are used to produce asymptotically stable and bounded motion. Sail orientation changes are also utilized in a proposed algorithm for generating transfers between the Earth and on-axis halo orbits.

1. Introduction

The human species stands on the edge of a new frontier, the transition from a planet-bound to a space-faring civilization. Just as the transition from hunter-gatherer to farmer necessitated new approaches to solve new problems, so the expansion into space, in terms of both human and robotic applications, requires the development of innovative new technologies and mission design strategies. Solar sail propulsion is one such new technology that promises to be useful in overcoming the challenges of moving throughout the solar system.

Using solar radiation pressure (SRP) as a method of spacecraft propulsion, although not yet fully exploited in an actual mission, is by no means a new idea. The concept dates back at least as far as the writings of Konstantin Tsiolkovsky in the 1920's [1]; it has now matured sufficiently to warrant serious consideration in the form of actual solar sail propulsion systems. The major advantage of a solar sail is clear: there is no propellant expenditure. Thus, the "thrust" is applied continuously, and the maneuvering capability of the spacecraft is limited only by the longevity of the materials from which the sail is constructed. For a solar sail spacecraft, the combination of these factors allows a huge variety of flight paths that are non-Keplerian in nature. However, techniques to efficiently design these trajectories are not yet available.

Exploiting solar sails in the context of multiple gravitational fields is yet another challenge. However, the "libration point" trajectories that exist in regimes defined by multiple gravitational fields are extremely useful for mission design, and have been incorporated into baseline trajectories that support various scientific objectives. Even the three-body problem has been studied extensively for several hundred years, and has inspired many new developments in the mathematical theory of differential equa-

tions and dynamical systems. These new developments, as well as recent significant insights into trajectory design that exploit three-body dynamics, have led to innovative non-Keplerian trajectories in the vicinity of the libration points, and missions such as ISEE-3 [2], WIND [3], Genesis [4], Triana [5], and others now in development.

The continuous thrust, long duration nature of solar sail propulsion is ideally suited to the dynamical interactions of a multi-body system. In concert with the tools of three-body trajectory design, solar sails offer a rich new set of trajectory options for mission designers. The focus of this research effort is the identification of some of these new trajectory options, and the development of methodologies to aid in the design of missions utilizing these trajectories.

1.1 Problem Definition

1.1.1 Circular Restricted Three-Body Problem

Traditional mission design focuses on a model of the system that is consistent with the two-body problem, usually comprised of some massive central body and a much less massive spacecraft. Ultimately, this approach leads to spacecraft equations of motion that result in the familiar conic sections of Keplerian motion. The gravitational fields of any additional bodies are then modelled as perturbations to the conic solution. Preliminary analysis for more ambitious missions is accomplished through a sequence of two-body arcs linked via the "patched conic" method.

A more general formulation of the problem that incorporates one additional gravitational interaction can be modelled as the three-body problem in orbital mechanics, and dates back to Newton's investigations in the 17th century [6]. Unlike the two-body problem, there is no closed form analytical solution for the differential equations governing the motion in the three-body problem. However, it is still possible, although not easy, to gain insight into the qualitative nature of the solutions in this system. This task is more tractable if several simplifying assumptions are introduced.

In reducing the general three-body equations, the first assumption is that the mass of one of the bodies is infinitesimal, that is, it does not affect the motion of the other two bodies. Thus, the two massive bodies, or primaries, move in Keplerian orbits

about their common center of mass. This reduced model is denoted the "restricted three-body problem," and was formalized by Euler in the late 18th century [6]. The problem is further simplified by constraining the primaries to move in *circular* orbits about their center of mass. The resulting simplified model is usually labelled the circular restricted three-body problem (CR3BP). Although a less complex dynamical model than the general problem (in terms of the number of equations and the number of dependent variables), analysis in the circular problem offers further understanding of the motion in a regime that is of increasing interest to space science, as well as new options for mission design.

Unfortunately, even with the simplifying assumptions, no general closed form solution to the CR3BP is available. However, particular solutions can be determined. Of notable interest are the equilibrium solutions, first identified by Lagrange in 1772, which represent locations where the infinitesimal particle remains fixed, relative to a frame of reference that rotates with the primaries.

1.1.2 Libration Points

If the restricted problem is formulated in terms of a coordinate frame that rotates with the primaries, it is possible to identify five equilibrium solutions, also known as libration or Lagrange points. Three of these points are collinear, and lie along the line joining the primaries. The other two points form equilateral triangles with the primaries, in the plane of primary motion.

The focus of most investigations into the three-body problem is the motion of the infinitesimal particle in the vicinity of the equilibrium points. The collinear points, in particular, have recently attracted much interest as a consequence of the three-dimensional bounded motion in their vicinity. These solutions, periodic halo orbits [7] and quasi-periodic Lissajous trajectories [8], exist in a region of the solution space that is not accessible through a two-body model, and they enable the design of mission scenarios that were not considered feasible previously.

In general, any initial analysis of motion in the vicinity of the libration points does not include solar radiation pressure. The magnitude of the SRP force is assumed to

be sufficiently small such that it can be accommodated as a perturbation in the latter stages of the trajectory design process. The inclusion of a solar sail, a device designed specifically to generate propulsively significant forces and to direct them appropriately using SRP, will transform solar radiation pressure from a mere perturbation into a critical force component. Thus, in this context, SRP must be incorporated at a much earlier phase of the trajectory design process.

1.1.3 Solar Radiation Pressure and Solar Sails

The fact that electromagnetic radiation can "push" matter is contrary to everyday experience, but commonplace in the solar system. Perhaps the most well known example is the dust tail created behind comets by solar radiation pressure [9]. In mission design, it is well known that the influence of SRP must be incorporated into the trajectory design process [10]. As accomplished for observational data, electromagnetic radiation pressure can also be derived from both Maxwell's electromagnetic theory and quantum theory [1]. Thus, theoretical tools for the analysis and design of devices utilizing SRP do exist.

From the perspective of quantum mechanics, solar radiation pressure can be conceptualized as the force generated by the the transfer of momentum from reflected photons to some reflective surface. Photons represent the discrete packets of energy that compose electromagnetic radiation. Although they possess zero rest mass, photons transport energy, and, thus, the mass-energy equivalence of special relativity implies that they also transport momentum. However, the momentum transported by an individual photon is relatively small. Thus, to generate a significant impact, it is desirable to use a large reflective area to capture as many photons as possible. Minimizing the mass of the reflective surface maximizes the resulting acceleration. This requirement for a high area-to-mass ratio implies that the ideal SRP-based propulsive device is a large, very thin reflective sheet. Hence, the name "solar sail". To date, SRP has been successfully used to generate attitude control torques [11, 12], but no spacecraft have yet flown that employ solar sails to derive primary propulsion.

1.2 Previous Contributions

1.2.1 The Restricted Problem

As mentioned, Leonhard Euler first formulated the restricted three-body problem in 1772, with his introduction of a rotating coordinate system [13]. Also in 1772, Joseph L. Lagrange identified the triangular libration points as a particular solution in the general three-body problem. Based on these results, Lagrange predicted the existence of the Sun-Jupiter Trojan asteroids; observations verified the prediction 134 years later [14].

Although apparently unaware of Euler's formalism and, thus, using a sidereal (non-rotating) coordinate system, Carl G. J. Jacobi was able to demonstrate the existence of a constant of the motion in 1836. This constant relates the square of the relative velocity of the "massless" particle to a pseudo-potential function derived from the centrifugal and gravitational potentials [6]. In the late 1800's, Henri Poincaré investigated the problem and concluded that the restricted three-body problem is non-integrable, but periodic solutions do exist. In the process, Poincaré laid the foundations for modern dynamical systems theory [6, 14].

1.2.2 Libration Point Orbits

In 1902, Henry C. Plummer, using an approximate, second-order analytical solution to the differential equations in the circular restricted three-body problem, produced a family of two-dimensional periodic orbits near the collinear libration points [15]. Forest R. Moulton, in studies performed between 1900 and 1917, numerically integrated periodic orbits, for several specific mass ratios, in the vicinity of the triangular libration points. Moulton's results also included three-dimensional periodic solutions to the linearized equations of motion relative to the collinear points [6]. Further work in this direction was hindered by the tedious computations required for both higher order analytical solutions and numerically integrated trajectories. Thus, researchers in this field did not progress significantly until the introduction of high-speed computers in the middle of the 20th century.

The 1967 publication of Victor G. Szebehely's book, *Theory of Orbits: The Re-*

stricted Problem of Three Bodies [6], brought together various strands of research, and effectively summarized the state of the art at that time. Szebehely's comprehensive treatise includes a survey of the numerically integrated trajectories then identified, and an introduction to the "three-dimensional" and "elliptic" formulations of the restricted three-body problem.

During the 1960's, Robert W. Farquhar initiated an analytical investigation into a class of precisely periodic three-dimensional trajectories known today as halo orbits [16]. These trajectories are associated with the collinear points, and are a special case of the more general libration point orbits frequently denoted as Lissajous trajectories. Working in conjunction with Ahmed A. Kamel, Farquhar developed analytical approximations for quasi-periodic solutions associated with L_2, the Earth-Moon libration point on the far side of the Moon, published in 1973 [8]. In 1975, David L. Richardson and Noel D. Cary derived a third-order approximation for motion near the interior Sun-Earth libration point [17] in the restricted problem. This was followed in 1980 by Richardson's third-order approximation to represent halo orbits near the collinear points in the circular restricted problem [18].

Beyond higher order analytical approximations, numerical investigations have refocused many of the studies of this problem since the 1970's. In 1979, considering motion in the vicinity of the collinear points, John V. Breakwell and John V. Brown could numerically extend the work of Farquhar and Kamel to produce a family of periodic halo orbits [7]. The discovery of a set of stable orbits in Breakwell and Brown's halo family motivated a search for stable orbits in the families associated with all three collinear points by Kathleen C. Howell, in collaboration with Breakwell, in 1982 [19]. Howell used the numerical technique of continuation to produce orbits beyond the range of validity of the analytical approximations. A range of "stable" periodic orbits appear in each libration point family [20, 21].

Given the three-dimensional halo families of precisely periodic orbits, Howell and Henry J. Pernicka sought numerical techniques to efficiently compute the quasi-periodic trajectories earlier identified by Farquhar [8]. A scheme to compute such

bounded trajectories successfully emerged in 1988 [22]. The technique developed by Howell and Pernicka relies on an iterative process to update some set of target states that lie at specified intervals along the trajectory.

In any actual mission scenario, unmodelled perturbations and injection errors, coupled with the generally unstable nature of libration point orbits, will cause a spacecraft to drift from the nominal trajectory. Consequently, in 1993, Howell and Pernicka developed a flexible stationkeeping strategy for libration point orbits [23]. The resulting methodology is also applicable to transfer arc and maneuver design [4, 24], as well as error analysis [25].

1.2.3 Solar Sails

It is generally agreed that the earliest suggestion that spacecraft could be propelled by sunlight appears in Konstantin E. Tsiolkovsky's 1921 publication *Extension of Man into Outer Space* [26]. An innovator in the application of scientific ideas, Tsiolkovsky was one of the first to consider many of the problems involved in space travel, and ultimately made a number of important contributions in aviation as well. Fridrickh Tsander, Tsiolkovsky's student and co-worker, published the first practical paper on solar sailing in 1924 [1].

After the early efforts by Tsiolkovsky and Tsander, the field remained relatively dormant for nearly 30 years. Then, in 1951, Carl Wiley, using the pseudonym Russell Sanders to protect his professional credibility, published an article about the feasibility and design of solar sails in *Astounding Science Fiction* [27]. Later, in 1958, Richard L. Garwin published the first paper on solar sailing in a technical archival journal, *Jet Propulsion* [28]. Garwin's optimistic evaluation of the practicality of solar sailing led several other researchers to explore the concept [1, 29, 30].

The next major advance appeared in the early 1970's. Jerome L. Wright, as part of some low-priority NASA studies on solar sails, discovered a trajectory that would allow a rendezvous with Halley's comet [1]. This prompted a formal proposal for a rendezvous mission in 1976, and led to the production of much practical research on solar sail construction and trajectories. However, solar sails are a technologically

risky proposition, and NASA endorsed an alternate solar-electric propulsion concept at the time. Eventually, due to escalating costs, any plans for a low-thrust rendezvous mission were halted.

An interesting conceptual leap appeared in 1991 in a paper by Robert L. Forward, who proposed using solar sails, not to propel a spacecraft, but to maintain it in a stationary position [31]. Forward's "statites" are suggested in response to the crowding of geosynchronous orbit, using solar radiation pressure to generate "levitated," non-Keplerian geosynchronous trajectories.

Throughout the 1990's, Colin R. McInnes has been extremely active in studying the dynamics of solar sails. McInnes is primarily concerned with analytical techniques for developing a first approximation for these non-Keplerian trajectories [26, 32, 33], including some work in the restricted three-body problem [34] as well as control issues [35]. Additionally, his investigations include the effects of more accurate solar radiation models [36]. In 1999, McInnes published *Solar Sailing* [1], summarizing in one book the state of the art in all aspects of solar sail design, construction, and trajectory design.

For application specifically to libration point missions, Julia L. Bell examined the effects of solar radiation pressure on the interior Sun-Earth libration point as well as the associated Lissajous trajectories in 1991 [37]. This work was not specifically focused on solar sails, but did include some preliminary results for the computation of halo orbits that incorporate some additional small magnitude force. Her force model is consistent with a solar sail in both magnitude and direction. More recently, extending the work of Bell and McInnes, Jason S. Nuss formulated a study of the dynamics of solar sails within the framework of the three-body problem [38]. His analysis includes periodic motion in the vicinity of points along the Sun-Earth axis, and he introduces the use of methodologies such as invariant manifold theory for the design of transfers to and from these periodic orbits.

1.3 Present Work

The focus of this current investigation is the development of methodologies for the design of solar sail trajectories within the context of the circular restricted three-body problem. This work expands upon the efforts of McInnes, Bell, and Nuss.

The approach is focused on the motion of the infinitesimal particle (i.e., the spacecraft) in the vicinity of the *new* libration points that result from the introduction of solar radiation pressure into the dynamical model. The first step in this process is the characterization of the dynamics of solar sails near these points. This process generates qualitative insight into the type of trajectories that may be feasible. Once an understanding of the dynamical structure is available, techniques for generating various kinds of libration point trajectories can be developed. As a starting point, methodologies that have previously been applied in the classical circular restricted three-body problem can be adapted to incorporate solar radiation pressure. However, the addition of a solar sail introduces new capabilities and thus may require new methodologies as well.

This work is arranged as follows:

CHAPTER 2: BACKGROUND

> The mathematical model corresponding to the classical circular restricted three-body problem is presented, and equations of motion are derived. An introduction to three-body trajectory analysis is presented, along with an example of a numerically generated libration point trajectory obtained through the analysis techniques being described. A force model for solar radiation pressure is also defined. Three-body equations of motion incorporating the effects of a solar sail are then derived. Expressions for the required sail orientation and performance capabilities to utilize a specific libration point are developed. New options are suggested through an understanding of the range of new "artificial" libration points generated by the addition of a solar sail.

CHAPTER 3: ON-AXIS SOLUTIONS

The effects of a solar sail on the locations of the familiar collinear libration points in the Sun-Earth system is examined. An approximation for motion in the vicinity of these points is developed from an existing approximation that did not include solar radiation pressure. The approximation is used to generate initial guesses for several numerical investigations. Families of periodic orbits are numerically determined and characterized. A stationkeeping algorithm useful in the transition to more representative models for the design of solar sail missions is developed and tested.

CHAPTER 4: OFF-AXIS SOLUTIONS

The stability and controllability of the off-axis libration points is reviewed. State feedback controllers are designed and used to stabilize the motion of a particle located at a libration point, and to generate periodic trajectories relative to an artificial equilibrium point. The use of discrete maneuvers to maintain bounded trajectories is discussed.

CHAPTER 5: TRANSFERS

The effects of solar radiation pressure on stable and unstable manifolds is examined. A technique for computing transfers to and from libration point orbits generated by incorporating a solar sail force is proposed.

CHAPTER 6: CONCLUSIONS

The conclusions of this investigation are summarized. Suggestions for future work are presented and discussed.

2. Background

The next few decades promise unprecedented growth in the exploration and exploitation of space. This inevitably requires a corresponding growth in capabilities. Challenging new mission scenarios will require innovative trajectory designs. The combination of libration point orbits and solar sails can create some unique trajectory options to support some of these complex scientific and engineering goals. This chapter includes a description of the circular restricted three-body model, and the development of the differential equations that govern three-dimensional motion of a small mass, i.e., a spacecraft, in this system. Particular solutions to the equations of motion are introduced, in the form of the five known equilibrium points. Analytical approximations for periodic orbits, and numerical techniques for refining them, are also described. The derivation of the force model for a solar sail is presented and it is incorporated into the equations of motion.

2.1 Circular Restricted Three-Body Problem

2.1.1 Assumptions

The general three-body problem, as formulated by Newton, consists of three bodies of arbitrary mass moving under their mutual gravitational influence. This system requires 18 scalar first-order differential equations to completely describe the resulting motion. The formulation of the *restricted* problem was originally suggested to Euler by the approximately circular motion of the planets about the Sun and the small masses of the asteroids relative to these larger bodies [6]. The application of a specific set of assumptions or constraints in the restricted problem reduces the system to 6 first-order differential equations, yielding an analysis that is far more tractable.

The fundamental assumption in reducing the general three-body problem to the

restricted problem concerns the mass distribution. Two of the bodies, labelled primaries (designated P_1 and P_2), are massive with respect to the third body (designated P_3). Thus, the third body is assumed to have infinitesimal mass relative to the primaries, and, therefore, does not affect the primary motion. All bodies are assumed spherically symmetric, and can therefore be represented as point masses. The masses of P_1, P_2, and P_3 are denoted by M_1, M_2, and M_3, respectively. The convention adopted in the following analysis for the relative size of the bodies is somewhat arbitrary, that is, $M_1 > M_2 \gg M_3$.

If the gravitational effects of P_3 are neglected, the determination of the motion of the primaries, P_1 and P_2, is reduced to the solution of a two-body problem. Therefore, the primary motion is Keplerian relative to their common center of mass, or barycenter. The two-body motion is further simplified by constraining the primaries to circular orbits about the barycenter, thus, the motion of P_3 becomes a solution to the circular restricted three-body problem.

2.1.2 Geometry

To formulate a mathematical expression for the motion of P_3, it is necessary to define several reference frames and position vectors. (See Figure 2.1.) Denote vectors with an overbar (e.g., $\overline{v}$) and unit vectors with a caret (e.g., $\hat{v}$).

Observe in the figure that the inertial reference frame I is comprised of the right-handed triad $\hat{X} - \hat{Y} - \hat{Z}$, such that the origin B is defined at the barycenter of the primary system. Frame I is oriented such that the $\hat{X} - \hat{Y}$ plane coincides with the plane of primary motion. Additionally, a synodic frame S is introduced such that the triad $\hat{x} - \hat{y} - \hat{z}$ is right-handed, with the origin at the barycenter. Frame S is initially coincident with frame I, but rotates such that the $\hat{x}$-axis is always directed from P_1 toward P_2. The angle between I and S is designated θ. Since the primary motion is constrained to be circular, the rate of change of θ, that is, $\dot{\theta}$, is equal to n, the mean motion of the P_1-P_2 system. The vector $\overline{R}$ represents the position of P_3 relative to B. Vectors $\overline{R}_1$ and $\overline{R}_2$ then locate P_3 relative to P_1 and P_2, respectively.

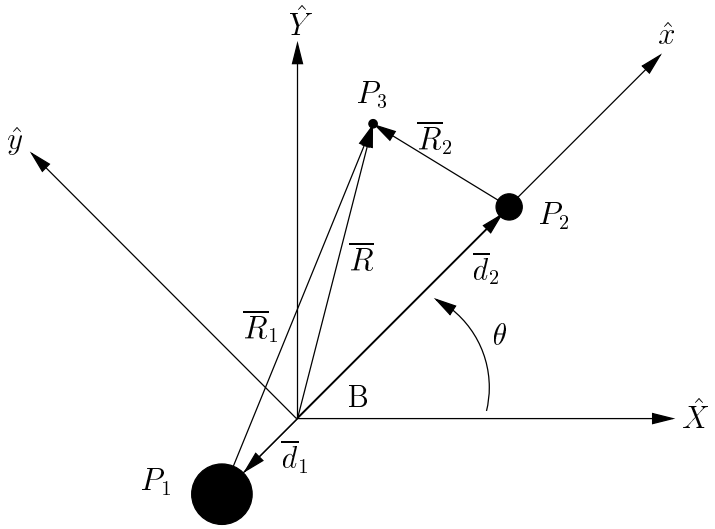

Figure 2.1. Geometry of the three-body problem

2.1.3 Equations of Motion

The differential equations in the circular restricted three-body problem are the mathematical expressions describing the motion of the infinitesimal mass P_3. The most significant forces that determine this motion are the gravitational forces on P_3 due to the primaries P_1 and P_2. Given Newton's Law of Gravity, these forces can be represented in the following form,

$$\overline{F}_{P_1} = -\frac{GM_1M_3}{R_1^2}\frac{\overline{R}_1}{R_1}\,, \tag{2.1}$$

and

$$\overline{F}_{P_2} = -\frac{GM_2M_3}{R_2^2}\frac{\overline{R}_2}{R_2}\,, \tag{2.2}$$

where G is the universal gravitational constant. The symbols R_1 and R_2 (without overbars) represent the magnitudes of the vectors $\overline{R}_1$ and $\overline{R}_2$. Thus, from Newton's Second Law, the general expression for the vector equation that governs the motion of P_3 is

$$\Sigma\overline{F} = M_3\frac{{}^I d^2\overline{R}}{dt^2} = -\frac{GM_1M_3}{R_1^2}\frac{\overline{R}_1}{R_1} - \frac{GM_2M_3}{R_2^2}\frac{\overline{R}_2}{R_2}\,, \tag{2.3}$$

where the superscript I denotes differentiation in the inertial frame.

To simplify and generalize the solution of this equation, it is useful to nondimensionalize the system of equations by introducing various characteristic quantities. These quantities include the characteristic length L^*, characteristic mass M^*, and characteristic time T^*. The characteristic length is defined as the distance between the primaries, that is, $L^* = |\overline{d}_1| + |\overline{d}_2|$. The sum of the primary masses serves as the characteristic mass such that $M^* = M_1 + M_2$. Then, the definition of the characteristic time is selected to be

$$T^* = \sqrt{\frac{L^{*3}}{GM^*}} \ . \tag{2.4}$$

This definition for T^* yields values of the gravitational constant, G, and the mean motion, n, that are both equal to one in terms of the nondimensional units. Using the characteristic quantities, and suitable additional nondimensional variables, equation (2.3) can be rewritten in nondimensional form as

$$\frac{{}^I d^2\overline{r}}{dt^2} = -\frac{(1-\mu)}{r_1^3}\overline{r}_1 - \frac{\mu}{r_2^3}\overline{r}_2 \ , \tag{2.5}$$

where $\overline{r} = \frac{\overline{R}}{L^*}$, $\overline{r}_1 = \frac{\overline{R}_1}{L^*}$, and $\overline{r}_2 = \frac{\overline{R}_2}{L^*}$. The mass ratio μ is also introduced as $\mu = \frac{M_2}{M^*}$ and, thus, $(1-\mu) = \frac{M_1}{M^*}$. The nondimensional vector form of the second-order differential equations is complete.

To determine the scalar equations of motion, the kinematic expressions on the left side of equation (2.5) must be expanded. The kinematic analysis begins with position. The position vector $\overline{r}$ is defined in terms of nondimensional components in the rotating frame, that is,

$$\overline{r} = x\hat{x} + y\hat{y} + z\hat{z} \ . \tag{2.6}$$

The first derivative of equation (2.6), with respect to nondimensional time and relative to an inertial observer, becomes

$${}^I\dot{\overline{r}} = \frac{{}^I d\overline{r}}{dt} = \frac{{}^S d\overline{r}}{dt} + {}^I\overline{\omega}^S \times \overline{r} \ , \tag{2.7}$$

where ${}^I\overline{\omega}^S$ is the angular velocity of the rotating frame, S, with respect to the inertial frame, I. As a consequence of the assumed circular motion of the primaries, this

angular velocity is constant and of the following form,

$$^I\overline{\omega}^S = n\hat{z} \ . \tag{2.8}$$

Furthermore, the nondimensional mean motion is equal to one, and, thus, the nondimensional angular velocity is most simply expressed as the unit vector $\hat{z}$. Evaluating equation (2.7) in terms of the scalar components yields,

$$^I\dot{\overline{r}} = (\dot{x} - y)\hat{x} + (\dot{y} + x)\hat{y} + \dot{z}\hat{z} \ . \tag{2.9}$$

Proceeding to the second derivative of $\overline{r}$, the acceleration of P_3 in the inertial frame is produced from the following operation,

$$^I\ddot{\overline{r}} = \frac{^Id^I\dot{\overline{r}}}{dt} = \frac{^Sd^I\dot{\overline{r}}}{dt} + ^I\overline{\omega}^S \times ^I\dot{\overline{r}} \ . \tag{2.10}$$

In terms of the scalar components, this results in the kinematic expression,

$$^I\ddot{\overline{r}} = (\ddot{x} - 2\dot{y} - x)\hat{x} + (\ddot{y} + 2\dot{x} - y)\hat{y} + \ddot{z}\hat{z} \ . \tag{2.11}$$

Expressions for $\overline{r}_1$ and $\overline{r}_2$ in terms of nondimensional scalar components are now available. The positions of the primaries with respect to the barycenter can be written in the form

$$\overline{d}_1 = -\frac{M_2}{M_1 + M_2}L^*\hat{x} = -\mu\hat{x} \ , \tag{2.12}$$

$$\overline{d}_2 = \frac{M_1}{M_1 + M_2}L^*\hat{x} = (1 - \mu)\hat{x} \ , \tag{2.13}$$

where $\overline{d}_1$ and $\overline{d}_2$ are defined in Figure 2.1. Thus, the resulting expressions for the components of $\overline{r}_1$ and $\overline{r}_2$ are

$$\overline{r}_1 = \overline{r} - \overline{d}_1 = (x + \mu)\hat{x} + y\hat{y} + z\hat{z} \ , \tag{2.14}$$

$$\overline{r}_2 = \overline{r} - \overline{d}_2 = (x - (1 - \mu))\hat{x} + y\hat{y} + z\hat{z} \ . \tag{2.15}$$

The scalar form of the second-order differential equations of motion in equation (2.5) is then

$$\ddot{x} - 2\dot{y} - x = -\frac{(1 - \mu)(x + \mu)}{r_1^3} - \frac{\mu(x - (1 - \mu))}{r_2^3} \ , \tag{2.16}$$

$$\ddot{y} + 2\dot{x} - y = -\frac{(1-\mu)y}{r_1^3} - \frac{\mu y}{r_2^3} , \tag{2.17}$$

$$\ddot{z} = -\frac{(1-\mu)z}{r_1^3} - \frac{\mu z}{r_2^3} . \tag{2.18}$$

A more compact notation may be developed by defining a pseudo-potential function U such that

$$U = \frac{(1-\mu)}{r_1} + \frac{\mu}{r_2} + \frac{1}{2}(x^2 + y^2) . \tag{2.19}$$

Then, the scalar equations of motion may be rewritten in the form

$$\ddot{x} - 2\dot{y} = U_x , \tag{2.20}$$

$$\ddot{y} + 2\dot{x} = U_y , \tag{2.21}$$

$$\ddot{z} = U_z , \tag{2.22}$$

where the symbol U_j denotes $\frac{\partial U}{\partial j}$. Equations (2.16)-(2.18) or equations (2.20)-(2.22) comprise the dynamical model for the circular restricted three-body problem.

2.1.4 Libration Points

From the equations of motion derived previously (equations (2.20),(2.21) and (2.22)), it is apparent that an equilibrium solution exists relative to the rotating frame S when the partial derivatives of the pseudo-potential function (U_x, U_y, U_z) are all zero, i.e., $\overline{\nabla} U = 0$. These points correspond to the positions in the rotating frame at which the gravitational forces and the centrifugal force associated with the rotation of the synodic reference frame all cancel, with the result that a particle positioned at one of these points appears stationary in the synodic frame.

There are five equilibrium points in the circular restricted three-body problem, also known as Lagrange points or libration points. Three of the libration points (the collinear points) lie along the $\hat{x}$-axis: one interior point between the two primaries, and one point on the far side of each primary with respect to the barycenter. The other two libration points (the triangular points) are each positioned at the apex of an equilateral triangle formed with the primaries. The notation frequently adopted denotes the interior point as L_1, the point exterior to P_2 as L_2, and the L_3 point

as exterior to P_1. The triangular points are designated L_4 and L_5, with L_4 moving ahead of the $\hat{x}$-axis and L_5 trailing the $\hat{x}$-axis as the synodic frame rotates relative to frame I. (See Figure 2.2.)

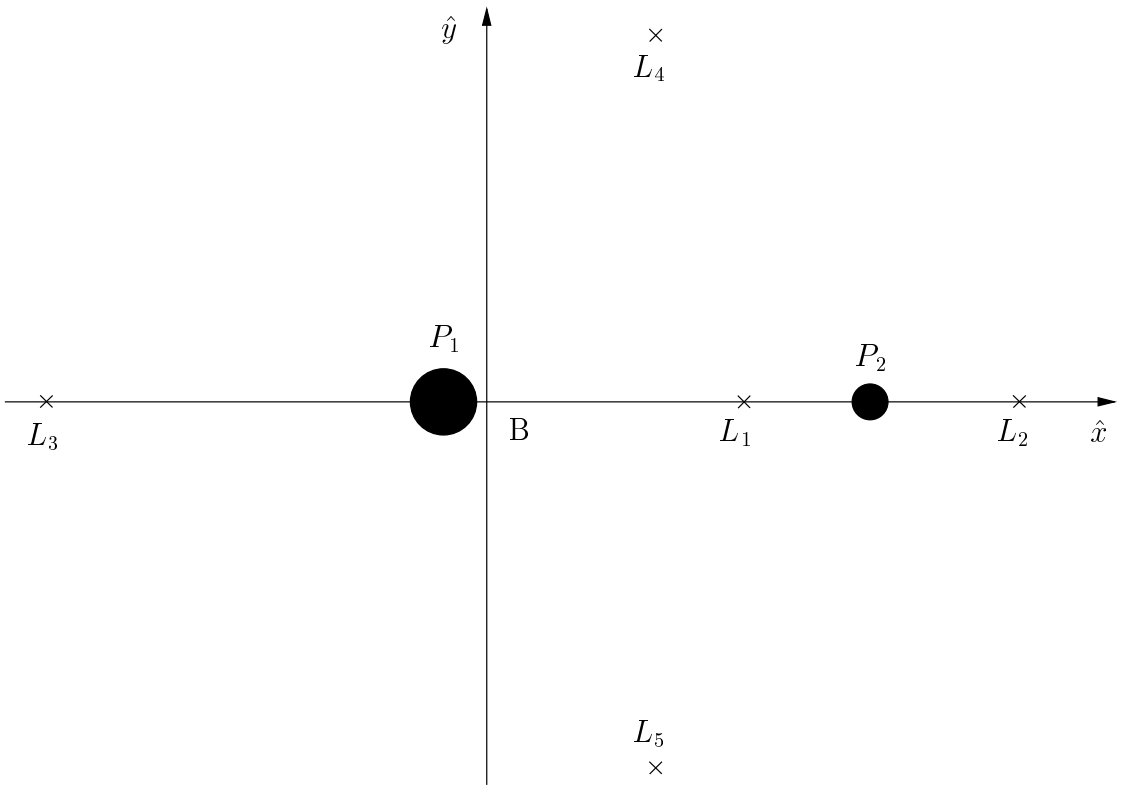

Figure 2.2. Position of the libration points corresponding to $\mu = 0.1$

The libration points are particular solutions to the equations of motion as well as equilibrium solutions. Of course, information about the stability of an equilibrium point in a nonlinear system can be obtained by linearizing and producing variational equations relative to the equilibrium solutions [39]. Thus, a limited investigation of the motion of P_3 in the vicinity of a libration point can be accomplished with linear analysis. The linear variational equations associated with libration point L_i, corresponding to the position $(x_{L_i},\ y_{L_i},\ z_{L_i})$ relative to the barycenter, can be determined through a Taylor series expansion about L_i, retaining only first-order terms. To allow

a more compact expression, the variational variables (ξ, η, ζ) are introduced such that

$$\xi = x - x_{L_i} \ , \quad \eta = y - y_{L_i} \ , \quad \text{and} \quad \zeta = z - z_{L_i} \ .$$

The resulting linear variational equations for motion about L_i are written as follows,

$$\ddot{\xi} - 2\dot{\eta} = U^*_{xx}\xi + U^*_{xy}\eta + U^*_{xz}\zeta \ , \tag{2.23}$$

$$\ddot{\eta} + 2\dot{\xi} = U^*_{yx}\xi + U^*_{yy}\eta + U^*_{yz}\zeta \ , \tag{2.24}$$

$$\ddot{\zeta} = U^*_{zx}\xi + U^*_{zy}\eta + U^*_{zz}\zeta \ , \tag{2.25}$$

where $U_{jk} = \frac{\partial U}{\partial j \partial k}$ and $U^*_{jk} = U_{jk}|_{L_i}$. The expressions corresponding to each of these partial derivatives appear in Appendix A.

Analysis of the variational equations is more convenient if they appear in state space form. This is accomplished by rewriting the system of three second-order differential equations (equations (2.23), (2.24), and (2.25)) as a system of six first-order equations. Defining the six-dimensional state vector as

$$\overline{\xi} \equiv \left[\xi \ \ \eta \ \ \zeta \ \ \dot{\xi} \ \ \dot{\eta} \ \ \dot{\zeta}\right]^T \ ,$$

the variational equations can be written in state space form as

$$\dot{\overline{\xi}} = \mathbf{A}\overline{\xi} \ , \tag{2.26}$$

where the bold typeface denotes a matrix, and the matrix $\mathbf{A}$ has the general form

$$\mathbf{A} \equiv \begin{bmatrix} \mathbf{0} & \mathbf{I}_3 \\ \mathbf{B} & \mathbf{C} \end{bmatrix} \ .$$

Then, the submatrices of $\mathbf{A}$ are

$$\mathbf{0} \equiv 3 \times 3 \quad \text{zero matrix},$$

$$\mathbf{I}_3 \equiv 3 \times 3 \quad \text{identity matrix},$$

$$\mathbf{B} \equiv \begin{bmatrix} U^*_{xx} & U^*_{xy} & U^*_{xz} \\ U^*_{yx} & U^*_{yy} & U^*_{yz} \\ U^*_{zx} & U^*_{zy} & U^*_{zz} \end{bmatrix} \ ,$$

$$\mathbf{C} \equiv \begin{bmatrix} 0 & 2 & 0 \\ -2 & 0 & 0 \\ 0 & 0 & 0 \end{bmatrix} .$$

The solution to the system of linear differential equations represented in equation (2.26) is of the following form,

$$\xi = \sum_{i=1}^{6} A_i e^{s_i t} , \tag{2.27}$$

$$\eta = \sum_{i=1}^{6} B_i e^{s_i t} , \tag{2.28}$$

$$\zeta = \sum_{i=1}^{6} C_i e^{s_i t} , \tag{2.29}$$

where the symbols A_i, B_i, and C_i represent constant coefficients, and the six eigenvalues of the matrix $\mathbf{A}$ appear as s_i. The eigenvalues, or characteristic roots, determine the stability of the linear system for motion relative to the equilibrium point, and, thus, also contain some information about the stability of the nonlinear system and the qualitative nature of the motion.

The systems of variational equations relative to the collinear points each possess two real eigenvalues, one of which is positive [6]. Thus, the motion in the region of the solution space surrounding the collinear points is generally unstable. However, the other four eigenvalues are purely imaginary, indicating the potential for strictly oscillatory motion. It is therefore possible to select initial conditions that excite only the oscillatory modes and generate stable periodic orbits. The eigenvalues corresponding to the linearized system and associated with the triangular points are all pure imaginary for $\mu < \mu_0 \approx 0.0385$; for $\mu > \mu_0$, some of the eigenvalues possess positive real parts. Thus, the nonlinear behavior near L_4 and L_5 is likely to be oscillatory and bounded for some combinations of primaries, and unstable for others.

2.1.5 Approximate Periodic Solutions

For initial conditions that excite only the oscillatory modes, the general form of the solution for motion near the collinear libration points is a Lissajous path described

mathematically as follows,

$$\xi = A_1 \cos \lambda t + A_2 \sin \lambda t \ , \tag{2.30}$$

$$\eta = -kA_1 \sin \lambda t + kA_2 \cos \lambda t \ , \tag{2.31}$$

$$\zeta = C_1 \sin \nu t + C_2 \cos \nu t \ , \tag{2.32}$$

where λ is the in-plane frequency, ν is the out-of-plane frequency, and k is a constant denoting a relationship between the coefficients corresponding to the ξ and η components. This is bounded motion that is not necessarily periodic since the ratios of the frequencies for the in-plane ($x-y$ or $\xi-\eta$) and out-of-plane (z or ζ) motion are generally irrational. By careful selection of the initial conditions associated with the Lissajous motion, a precisely periodic orbit can be constructed. Of course, specification of the initial states effectively imposes certain constraints on the in-plane and out-of-plane amplitudes and phases. The result is a first-order solution of the form

$$\xi = -A_x \cos(\lambda t + \phi) \ , \tag{2.33}$$

$$\eta = kA_x \sin(\lambda t + \phi) \ , \tag{2.34}$$

$$\zeta = A_z \sin(\nu t + \psi) \ , \tag{2.35}$$

where A_x and A_z are the in-plane and out-of-plane amplitudes, while ϕ and ψ are the phase angles.

Using the first-order periodic solution as a basis, Richardson [18] applies the method of successive approximations to develop a third-order solution for periodic motion about the collinear points:

$$\begin{aligned} \xi = {} & a_{21}A_x^2 + a_{22}A_z^2 - A_x \cos(\lambda\tau + \phi) + (a_{23}A_x^2 - a_{24}A_z^2)\cos(2\lambda\tau + 2\phi) \\ & + (a_{31}A_x^3 - a_{32}A_xA_z^2)\cos(3\lambda\tau + 3\phi) \ , \end{aligned} \tag{2.36}$$

$$\begin{aligned} \eta = {} & kA_x \sin(\lambda\tau + \phi) + (b_{21}A_x^2 - b_{22}A_z^2)\sin(2\lambda\tau + 2\phi) \\ & + (b_{31}A_x^3 - b_{32}A_xA_z^2)\sin(3\lambda\tau + 3\phi) \ , \end{aligned} \tag{2.37}$$

$$\begin{aligned} \zeta = {} & \delta_n A_z \cos(\lambda\tau + \phi) + \delta_n d_{21}A_xA_z(cos(2\lambda\tau + 2\phi) - 3) \\ & + \delta_n(d_{32}A_zA_x^2 - d_{31}A_z^3)\cos(3\lambda\tau + 3\phi) \ , \end{aligned} \tag{2.38}$$

where a_{jk}, b_{jk}, and d_{jk} are coefficients derived from the successive approximation procedure (see Appendix B), $\delta_n = \pm 1$ is a switch function specifying the direction of the maximum out-of-plane excursion, and τ is a scaled time variable. Additionally, the amplitudes A_x and A_z must satisfy the constraint relationship [18]

$$l_1 A_x^2 + l_2 A_z^2 + \Delta = 0 \ , \tag{2.39}$$

where l_1, l_2, and Δ are evaluated from the expressions that appear in Appendix B.

The coefficients a_{jk}, b_{jk}, d_{jk}, l_j, and k, and the frequency λ, are ultimately functions of c_n, the coefficients in a Legendre polynomial expansion that represents the Lagrangian for motion in the vicinity of a collinear libration point [40]. The coefficients c_n are evaluated from the following expressions,

$$c_n = \frac{1}{\gamma_L^3}\left[(\pm 1)^n \mu + (-1)^n \frac{(1-\mu)\gamma_L^{n+1}}{(1 \mp \gamma_L)^{n+1}}\right] \quad (L_1 \ \text{or} \ L_2) \ , \tag{2.40}$$

$$c_n = \frac{1}{\gamma_L^3}\left[1 - \mu + \frac{\mu \gamma_L^{n+1}}{(1+\gamma_L)^{n+1}}\right] \quad (L_3) \ , \tag{2.41}$$

where γ_L is the ratio of the distance between the libration point and the nearest primary to the distance between the primaries.

These approximate analytical solutions offer useful insights into the nature of the motion in the vicinity of the collinear libration points. In particular, families of three-dimensional periodic orbits, commonly labelled as "halo" orbits [16], are known to exist and have been numerically computed [20, 21]. These orbits are broadly classified in terms of the sign of the out-of-plane component at the point of maximum excursion as either northern ($\max(z) > 0$), or southern ($\max(z) < 0$). Approximate solutions are also useful in any numerical scheme to determine exact solutions to the nonlinear equations of motion. The numerical techniques that are applied to generate exact numerically integrated solutions to the nonlinear equations are not self-starting, and require an externally generated initial guess that is near a periodic orbit. This initial guess can sometimes be provided by an approximate analytical solution.

2.1.6 The State Transition Matrix

The numerical technique to determine precisely periodic orbits in the nonlinear system is the differential corrections method. The use of differential corrections to compute a periodic orbit requires information concerning the sensitivity of a state along the path to changes in the initial conditions. Such sensitivity information is obtained by linearizing the equations of motion relative to a reference trajectory, and then using the resulting linear variational equations to develop a state transition matrix.

The linear variational equations for motion relative to a reference trajectory, i.e., one that is a solution to the nonlinear differential equations, are similar to those previously developed relative to the constant equilibrium solutions, that is, the libration points. Perturbation variables are again introduced, although, to distinguish them from the variables (ξ, η, ζ) that represent variations relative to the libration points, the variations with respect to the reference trajectory are designated $(\delta x, \delta y, \delta z)$. The six-dimensional state vector is then defined as

$$\delta\overline{x} \equiv [\delta x \;\; \delta y \;\; \delta z \;\; \delta\dot{x} \;\; \delta\dot{y} \;\; \delta\dot{z}]^T \;\; ,$$

and the resulting state space form of the variational equations appears as

$$\delta\dot{\overline{x}}(t) = \mathbf{A}(t)\delta\overline{x}(t) \; . \tag{2.42}$$

The time-dependent matrix $\mathbf{A}(t)$ is represented in terms of four 3×3 submatrices, that is,

$$\mathbf{A}(t) \equiv \begin{bmatrix} \mathbf{0} & \mathbf{I}_3 \\ \mathbf{B}(t) & \mathbf{C} \end{bmatrix} \; .$$

This is similar in form to the $\mathbf{A}$ matrix corresponding to the variational equations derived relative to the libration points. However, in this case, the submatrix $\mathbf{B}(t)$ is not a constant, and therefore $\mathbf{A}(t)$ is time-varying.

The general form of the solution to the system in equation (2.42) is

$$\delta\overline{x}(t) = \mathbf{\Phi}(t, t_0)\delta\overline{x}(t_0) \; , \tag{2.43}$$

where $\mathbf{\Phi}(t, t_0)$ is the state transition matrix (STM). The STM is a linear map from the initial state at the initial time t_0 to a state at some later time t, and thus offers a tool to approximate the impact of variations in the initial state on the evolution of the trajectory. The STM must satisfy the matrix differential equation

$$\dot{\mathbf{\Phi}}(t, t_0) = \mathbf{A}(t)\mathbf{\Phi}(t, t_0) \ , \tag{2.44}$$

given the initial condition,

$$\mathbf{\Phi}(t_0, t_0) = \mathbf{I}_6 \ , \tag{2.45}$$

where $\mathbf{I}_6$ is the 6×6 identity matrix.

It is clear that the STM at time t can be numerically determined by integrating equation (2.44) from the initial value in equation (2.45). Since the STM is a 6×6 matrix, propagation of equations (2.44) requires the integration of 36 first-order scalar differential equations. Since the elements of $\mathbf{B}(t)$, and hence $\mathbf{A}(t)$, depend on the reference trajectory, equation (2.44) must be integrated simultaneously with the nonlinear equations of motion to generate the reference states. This necessitates the integration of an additional 6 first-order equations, for a total of 42 scalar differential equations.

2.1.7 Differential Corrections

The differential corrections technique is essentially an iterative targeting scheme. Given some initial state $\overline{x}(t_0)$, where the six-dimensional state vector is defined as

$$\overline{x} \equiv \begin{bmatrix} x & y & z & \dot{x} & \dot{y} & \dot{z} \end{bmatrix}^T \ ,$$

the objective is the generation of a trajectory that terminates at a desired state $\overline{x}(t_f)_{des}$. In general, the integration of $\overline{x}(t_0)$ will terminate at some state $\overline{x}(t_f)$ that differs from the desired state. The initial state is then modified such that the resultant final state is within some threshold distance of the desired state.

The effect on the final state of a modification in the initial state can be estimated by examining the first variations in the final state, that is,

$$\delta\overline{x}(t_f) = \frac{\partial\overline{x}(t_f)}{\partial\overline{x}(t_0)}\delta\overline{x}(t_0) + \dot{\overline{x}}(t_f)\delta(t_f - t_0) \ . \tag{2.46}$$

The matrix partial derivative $\frac{\partial \overline{x}(t_f)}{\partial \overline{x}(t_0)}$ is equivalent to the state transition matrix, evaluated at time t_f. Thus, equation (2.46) is simply,

$$\delta\overline{x}(t_f) = \mathbf{\Phi}(t_f, t_0)\delta\overline{x}(t_0) + \dot{\overline{x}}(t_f)\delta(t_f - t_0) \ . \tag{2.47}$$

The correction in the final state that is required to match the value corresponding to the desired state can be written as

$$\delta\overline{x}(t_f) = \overline{x}(t_f)_{des} - \overline{x}(t_f) \ . \tag{2.48}$$

By substituting equation (2.48) into equation (2.47), it is possible to solve for an estimate of the change in the initial state, $\delta\overline{x}(t_0)$, that is required to generate the desired final state. In general, this procedure will require several iterations, since it is based on a linear approximation; the system of interest is, of course, nonlinear.

Recall that three-dimensional periodic halo orbits are known to exist in the vicinity of the libration points. Such orbits can be numerically computed by exploiting equation (2.47) [20, 21, 19]. The process is simplified by taking advantage of the symmetry of these familiar orbits about the $\hat{x} - \hat{z}$ plane. This symmetry implies that the periodic orbit must cross the $\hat{x} - \hat{z}$ plane perpendicularly, and, therefore, at the crossings,

$$y = \dot{x} = \dot{z} = 0 \ .$$

From the perspective of the numerical algorithm, the condition corresponding to the perpendicular plane crossings yields several useful features. First, the computational overhead is reduced since the initial state need only be integrated for a half revolution. Second, there is no need to specify a final time, t_f, a priori, since the intersection with the $\hat{x} - \hat{z}$ plane, i.e., $y(t_f) = 0$, can be used as a stopping condition in the algorithm. In fact, since $y(t_f)$ is specified to be equal to zero, $\delta(t_f - t_0)$ emerges as the sixth dependent variable in equation (2.47).

If the initial state is selected such that it corresponds to a plane crossing, then the initial state vector is evaluated in the form

$$\overline{x}(t_0) = [x_0 \ \ 0 \ \ z_0 \ \ 0 \ \ \dot{y}_0 \ \ 0]^T \ .$$

To maintain this perpendicular departure, the only elements of the initial state that can be manipulated are x_0, z_0, and $\dot{y}_0$. For periodicity, the desired final state vector also possesses the form

$$\overline{x}(t_f)_{des} = [x_f \;\; 0 \;\; z_f \;\; 0 \;\; \dot{y}_f \;\; 0]^T \;\; .$$

The values of x_f, z_f, and $\dot{y}_f$ are arbitrary, since the perpendicular crossing condition is established solely by the requirement that $y_f = \dot{x}_f = \dot{z}_f = 0$. Since $y_f = 0$ is used as the stopping condition for the integrator, the corrections process adjusts the initial conditions to shift the final state elements $\dot{x}_f$ and $\dot{z}_f$ closer to zero. Thus, the evaluation of $\delta\overline{x}(t_0)$ from equation (2.47) is reduced to solving a system of two equations (from $\dot{x}_f$ and $\dot{z}_f$) in three unknowns (x_0, z_0, and $\dot{y}_0$). A minimum norm solution is immediately available using standard techniques from linear algebra. However, to allow more control over the specific orbit that is isolated with this procedure, the approach adopted in this investigation is based on fixing one of the initial state elements, and, thus, reducing the system to two equations in two unknowns. This latter approach is useful, for example, to force the generation of halo orbits with some specified amplitude.

An arbitrary L_1 halo orbit in the Sun-Earth system, one that is generated by differentially correcting a third-order approximate solution, is depicted in Figure 2.3. The orbit is plotted in the rotating frame with the origin at the Sun-Earth barycenter. Since the maximum out-of-plane excursion (200,000 km) is in the positive $\hat{z}$ direction, this orbit is a member of the northern halo family. Also consistent with a northern family, note the direction of motion in the $\hat{y} - \hat{z}$ projection.

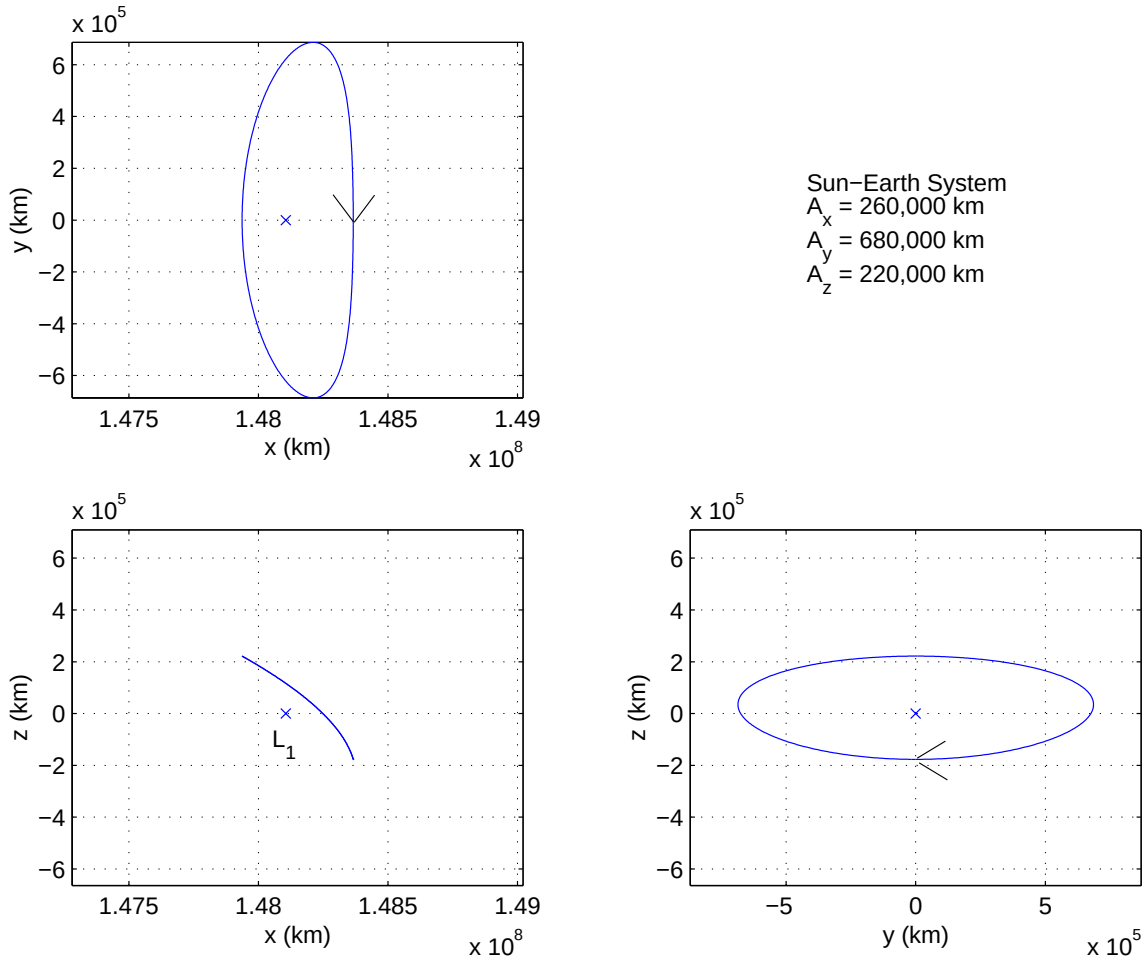

Figure 2.3. Example: Sun-Earth L_1 halo orbit

2.2 Solar Sails

2.2.1 Force Model

The existence of radiation pressure was predicted in 1873 by James Clerk Maxwell [1], as a consequence of the unified theory of electromagnetic radiation. Later representations were derived from quantum mechanical principles. However, in both cases the resulting expression for the radiation pressure is the same, that is,

$$P = \frac{W}{c} \,, \tag{2.49}$$

where the scalar P denotes the magnitude of the radiation pressure force, and c is the speed of light. The symbol W in equation (2.49) represents the energy flux of the electromagnetic radiation that is inducing the pressure. Assuming that the effects of a finite solar disc are negligible (i.e., that the Sun can be modelled as a point source), the energy flux of solar radiation varies in proportion to the inverse square of the distance from the Sun. At the mean distance of the Earth from the Sun, $L^* = 1$ AU, and the solar flux, including all frequencies of solar radiation, is approximately $W^* = 1368$ $\mathrm{Js^{-1}m^{-2}}$. Assuming perfect capture, this results in a value of the solar radiation pressure force per area such that $P^* = 4.56 \times 10^{-6}$ $\mathrm{Nm^{-2}}$.

The mathematical model to be used for the solar radiation pressure force is consistent with other studies, i.e., McInnes [1], Bell [37], and Nuss [38]. For the purposes of this investigation, it is assumed that the solar sails are ideal, flat, perfectly reflecting surfaces. Thus, the solar sails intercept photons of all possible frequencies, and reflect them in perfectly elastic collisions. As a consequence of these assumptions, such solar sails experience both a momentum transfer force from incident photons, and a reaction force — of equal magnitude — from the reflected photons. (See Figure 2.4.) The resultant force is directed normal to the surface of the sail, and the magnitude of the pressure force is exactly twice the value computed in equation (2.49).

The net force generated by a solar sail is clearly dependent on the area of the sail that is exposed to solar radiation. The exposed area varies in response to changes in the sail orientation relative to direction of the solar radiation. The angle between the

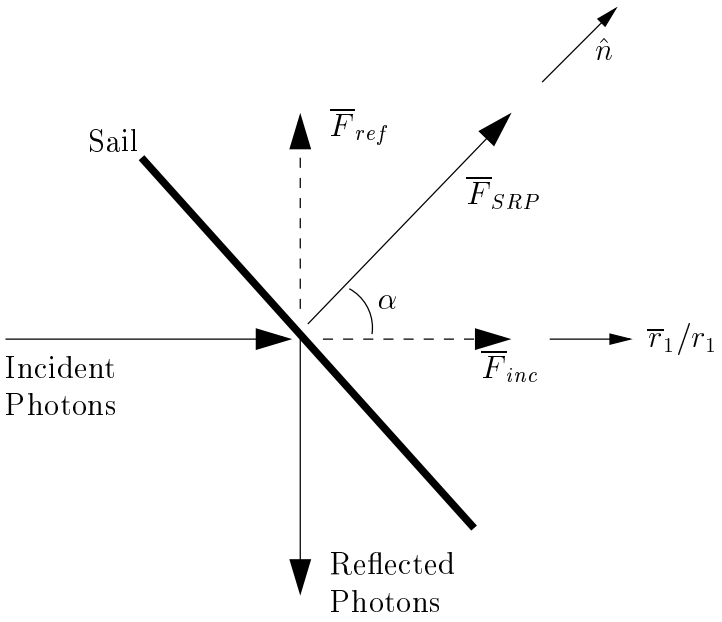

Figure 2.4. Force on a flat, perfectly reflecting solar sail

sail normal and the incident solar radiation is designated α (as it appears in Figure 2.4). At $\alpha = 0°$, the sail is perpendicular to the solar radiation, thus maximizing the projected area of the sail, and the resultant force. As α increases, the projected area of the sail and the magnitude of the resultant force each decreases. The equation that models the force vector on a solar sail of mass M_3, at a distance R_1 from the Sun (P_1), is

$$\overline{F}_{SRP} = \frac{2P^* M_3}{\sigma} \left(\frac{L^*}{R_1}\right)^2 \cos^2 \alpha \; \hat{n} \; , \tag{2.50}$$

where $\hat{n}$ is the sail surface normal vector, and σ is a sail design parameter defined as the ratio of the sail mass to sail area.

The mass/area ratio that is required, such that a sail with $\alpha = 0°$ generates a force equal and opposite to the solar gravitational force is,

$$\sigma^* = \frac{2P^* L^{*2}}{GM_1} \; , \tag{2.51}$$

where G is the universal gravitational constant and M_1 is the mass of the Sun. The corresponding value of σ^* is determined to be approximately equal to 1.53 g m^{-2}.

Then, using the terminology introduced by McInnes [1, 34, 35], the dimensionless sail lightness parameter β can be defined as follows,

$$\beta \equiv \frac{\sigma^*}{\sigma} \ .$$

Effectively, the sail lightness parameter is the ratio of solar radiation pressure acceleration to solar gravitational acceleration. Since both accelerations are assumed to be functions of the inverse square of the distance between the sail and the Sun, β is independent of distance. Typical sail lightness values for current solar sail designs range from a conservative $\beta \approx 0.03$ to optimistic proposals for sails with a lightness parameter of $\beta \approx 0.3$ [1]. The effective sail lightness value for a typical spacecraft without a solar sail is approximately $\beta = 1.5 \times 10^{-5}$ (derived from values given by Bell [37], and converted from Bell's model using the expression $\beta \approx \frac{1.53 \times S}{1000}$.)

The introduction of the sail lightness parameter allows reformulation of equation (2.50) in terms of solar gravitational acceleration, that is,

$$\overline{F}_{SRP} = \beta \frac{G M_1 M_3}{R_1^2} \cos^2 \alpha \ \hat{n} \ . \tag{2.52}$$

The force described by equation (2.52) can be rewritten as an acceleration per unit mass, in terms of the nondimensional units introduced previously, as,

$${}^{I}\ddot{\overline{r}}_{SRP} = \beta \frac{(1-\mu)}{r_1^2} \cos^2 \alpha \ \hat{n} \ . \tag{2.53}$$

Equation (2.53) represents the effects of a solar sail in a form that is readily incorporated into the equations of motion derived in the circular restricted three-body problem.

2.2.2 Solar Sail Orientation

The direction of the solar sail "thrust" vector is determined by the orientation of the sail with respect to the incident solar radiation. It is assumed that gravitational torques on the sail structure are negligible, and that the sail orientation is completely controllable (e.g., with "control vanes" that use solar radiation pressure to generate attitude control torques [41].) The sail orientation can be described using two angles

defined in terms of a sail centered orthogonal reference frame. One of these angles is the cone angle, previously defined as α, that corresponds to nutation. The other angle is the clock angle, labelled γ, that corresponds to a precession angle.

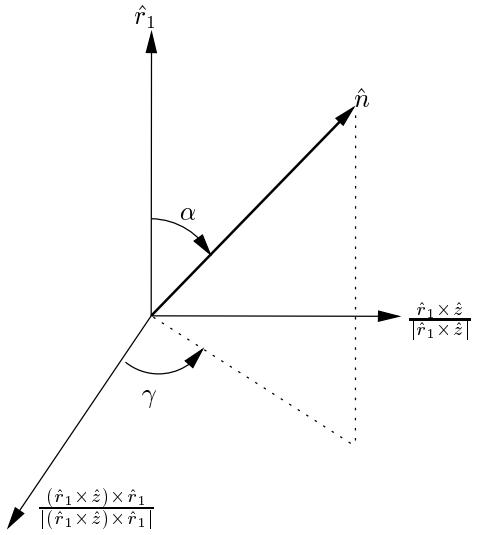

Figure 2.5. Definition of sail angles

The solar radiation is assumed to be directed radially from the Sun towards the solar sail, and, thus, is represented by the unit vector $\hat{r}_1 = \overline{r}_1/r_1$. The other vectors composing the reference orthogonal triad are constructed with the aid of the $\hat{z}$ unit vector, which is common to both the inertial and rotating frames. Illustrated in Figure 2.5 is the relationship between α, γ, the sail normal, and the incident solar radiation. Given the definition of α with respect to the Sun radius line, a constant value of α implies that the sail will complete one revolution in the inertial frame with each orbit.

The sail orientation can also be expressed in terms of the components of the sail normal vector as expressed in the rotating frame. Given the sail angle definitions, the scalar components of $\hat{n}$ corresponding to the directions $\hat{x}$, $\hat{y}$, and $\hat{z}$ are

$$n_x = \frac{\cos\alpha\ (x+\mu)}{|\overline{r}_1|} - \frac{\sin\alpha\ \cos\gamma\ (x+\mu)z}{|(\overline{r}_1 \times \hat{z}) \times \overline{r}_1|} + \frac{\sin\alpha\ \sin\gamma\ y}{|\overline{r}_1 \times \hat{z}|}\ , \qquad (2.54)$$

$$n_y = \frac{\cos\alpha\ y}{|\overline{r}_1|} - \frac{\sin\alpha\ \cos\gamma\ yz}{|(\overline{r}_1 \times \hat{z}) \times \overline{r}_1|} - \frac{\sin\alpha\ \sin\gamma\ (x+\mu)}{|\overline{r}_1 \times \hat{z}|}\ , \tag{2.55}$$

$$n_z = \frac{\cos\alpha\ z}{|\overline{r}_1|} + \frac{\sin\alpha\ \cos\gamma\ (y^2 + (x+\mu)^2)}{|(\overline{r}_1 \times \hat{z}) \times \overline{r}_1|}\ , \tag{2.56}$$

where

$$|\overline{r}_1| = \sqrt{(x+\mu)^2 + y^2 + z^2}\ ,$$
$$|\overline{r}_1 \times \hat{z}| = \sqrt{(x+\mu)^2 + y^2}\ ,$$
$$|(\overline{r}_1 \times \hat{z}) \times \overline{r}_1| = \sqrt{(x+\mu)^2 z^2 + y^2 z^2 + ((x+\mu)^2 + y^2)^2}\ .$$

Representing the sail orientation as defined in equations (2.54), (2.55), and (2.56) allows the effects of a solar sail to be added to the scalar equations of motion as formulated in the circular restricted three-body problem.

2.2.3 Three-Body Equations of Motion

Recall from equation (2.5) that the vector differential equation governing motion of the infinitesimal mass with respect to the two primaries in the circular restricted three body problem is

$$\frac{{}^I d^2\overline{r}}{dt^2} = -\frac{(1-\mu)}{r_1^3}\overline{r}_1 - \frac{\mu}{r_2^3}\overline{r}_2\ ,$$

where the terms on the right hand side of the equation represent the gravitational accelerations due to P_1 and P_2, respectively, expressed in terms of nondimensional quantities. Inclusion of a solar sail adds another force, and therefore another acceleration term, to the model. Incorporating the solar sail acceleration from equation (2.53) into the vector equation of motion, yields a modified form of equation (2.5), i.e.,

$$\frac{{}^I d^2\overline{r}}{dt^2} = -\frac{(1-\mu)}{r_1^3}\overline{r}_1 - \frac{\mu}{r_2^3}\overline{r}_2 + \beta\frac{(1-\mu)}{r_1^2}\cos^2\alpha\ \hat{n}\ . \tag{2.57}$$

Thus, this equation defines the dynamical system that is the focus of this investigation.

To enable a compact expression for the scalar form of the equations of motion, the solar sail acceleration is defined in terms of three auxiliary variables representing

the scalar components corresponding to rotating coordinates:

$$a_x = \beta \frac{(1-\mu)}{r_1^2} \cos^2 \alpha \; n_x \; , \tag{2.58}$$

$$a_y = \beta \frac{(1-\mu)}{r_1^2} \cos^2 \alpha \; n_y \; , \tag{2.59}$$

$$a_z = \beta \frac{(1-\mu)}{r_1^2} \cos^2 \alpha \; n_z \; , \tag{2.60}$$

where $\hat{n}_x$, $\hat{n}_y$, and $\hat{n}_z$ are the components of the sail normal vector from equations (2.54), (2.55), and (2.56). With the inclusion of the solar sail accelerations, the scalar equations for the motion of P_3 are augmented and appear in the form

$$\ddot{x} - 2\dot{y} = U_x + a_x \; , \tag{2.61}$$

$$\ddot{y} + 2\dot{x} = U_y + a_y \; , \tag{2.62}$$

$$\ddot{z} = U_z + a_z \; , \tag{2.63}$$

where the U_j terms are the partial derivatives of the three-body scalar potential defined in equations (2.20)-(2.22).

2.2.4 Solar Sail Libration Points

The equations of motion that result from the addition of a solar sail force to the circular restricted three-body problem possess new equilibrium solutions. McInnes, McDonald, Simmons, and MacDonald [34] determined that the modified equations of motion result in surfaces of "artificial" libration points. These surfaces can be parameterized by sail orientation. As usual, the equilibrium solutions in the restricted problem correspond to positions at which all components of velocity and acceleration relative to the rotating coordinates are zero. Thus, from equations (2.61), (2.62), and (2.63) the equilibrium solutions are computed from the relationship,

$$-\overline{\nabla} U = \beta \frac{(1-\mu)}{r_1^2} \cos^2 \alpha \; \hat{n} \; , \tag{2.64}$$

where $\overline{\nabla} U = U_x \hat{x} + U_y \hat{y} + U_z \hat{z}$. The vector product of $\overline{\nabla} U$, as determined in equation (2.64), and $\hat{n}$ produces zero, i.e.,

$$-\overline{\nabla} U \times \hat{n} = \overline{0} \; , \tag{2.65}$$

that implies that an artificial libration point exists only if the sail orientation, represented by $\hat{n}$, is parallel to $\overline{\nabla}U$. Since the $\hat{n}$ is a unit vector, the expression

$$\hat{n} = \frac{-\overline{\nabla}U}{|-\overline{\nabla}U|} , \tag{2.66}$$

yields a sail normal in the appropriate direction.

From the definition of α, the cosine of the sail cone angle is

$$\cos\alpha = \hat{r}_1 \cdot \hat{n} = \hat{r}_1 \cdot \frac{-\overline{\nabla}U}{|-\overline{\nabla}U|} . \tag{2.67}$$

Thus, equation (2.64) can be solved explicitly for the sail lightness parameter that is required to produce an artificial libration point, and the result appears as follows,

$$\beta = \frac{r_1^2}{(1-\mu)} \frac{|-\overline{\nabla}U|^3}{(\hat{r}_1 \cdot -\overline{\nabla}U)^2} , \qquad \beta \geq 0 . \tag{2.68}$$

The required sail orientation can be deduced using the vector and scalar products of equation (2.66) with $\hat{r}_1$. The resulting expressions are

$$\tan\alpha = \frac{|\hat{r}_1 \times -\overline{\nabla}U|}{\hat{r}_1 \cdot -\overline{\nabla}U} , \tag{2.69}$$

$$\tan\gamma = \frac{|(\hat{r}_1 \times \hat{z}) \times (\hat{r}_1 \times -\overline{\nabla}U)|}{(\hat{r}_1 \times \hat{z}) \cdot (\hat{r}_1 \times -\overline{\nabla}U)} . \tag{2.70}$$

Note that α is constrained to lie in the range $-90^\circ \leq \alpha \leq 90^\circ$, since it is physically impossible to direct the solar radiation pressure acceleration vector sunward, and, as a consequence, the sail normal vector will never be directed towards the Sun.

Using the expressions for β, α, and γ from equations (2.68)-(2.70), a set of potential artificial libration points can be parameterized by sail lightness β. This parameterization generates level surfaces as demonstrated, for the Sun-Earth system, in Figures 2.6-2.10. These figures are plotted in the barycentric rotating frame. Note that Figures 2.8 and 2.9 depict a more detailed view of the level surfaces in the vicinity of the Earth. Topologically, these surfaces are nested toroids, although, for $\beta > 1.0$ the interior radii of the toroids vanish. Each point on a given surface corresponds to a particular sail orientation. Of course, the conditions corresponding to the classical three-body problem exist as a special case of the general solar sail equations of motion, when $\beta = 0$ or $\alpha = 0^\circ$, and the level surfaces collapse to the libration points.

The level surfaces asymptotically approach a boundary, defined by a constraint on α, as $\beta \to \infty$. The boundary can be determined by expressing the constraint in the form

$$\overline{r}_1 \cdot -\overline{\overline{\nabla}} U \geq 0 \; . \tag{2.71}$$

The bounding surface is then defined by the equality condition in equation (2.71), that, when evaluated, yields the relationship,

$$x(x+\mu) + y^2 - \frac{(1-\mu)}{r_1} - \frac{(\overline{r}_1 \cdot \overline{r}_2)\mu}{r_2^3} = 0 \; . \tag{2.72}$$

This equation defines two topologically disconnected surfaces, designated S_1 and S_2, that bound the region of existence for the artificial libration points (Figures 2.6-2.9). Surface S_1 has a cylindrical topology and, in the $\hat{x} - \hat{y}$ plane, excludes solutions that lie outside the classical L_2 and L_3 points. Surface S_2 excludes solutions between L_1 and P_2 along the $\hat{x}$-axis, as well as some off-axis locations apparent in Figures 2.8 and 2.9. All five classical libration points are located on one of the bounding surfaces.

The huge range of potential artificial libration points, as depicted in Figures 2.6-2.10, offers the possibility of many new mission scenarios. However, to utilize these new points in the conceptual development of a mission, a better understanding of the dynamical properties of the artificial libration points is necessary. The exploration and exploitation of the dynamics in the vicinity of the artificial libration points that are generated by a solar sail is the primary focus of the following sections.

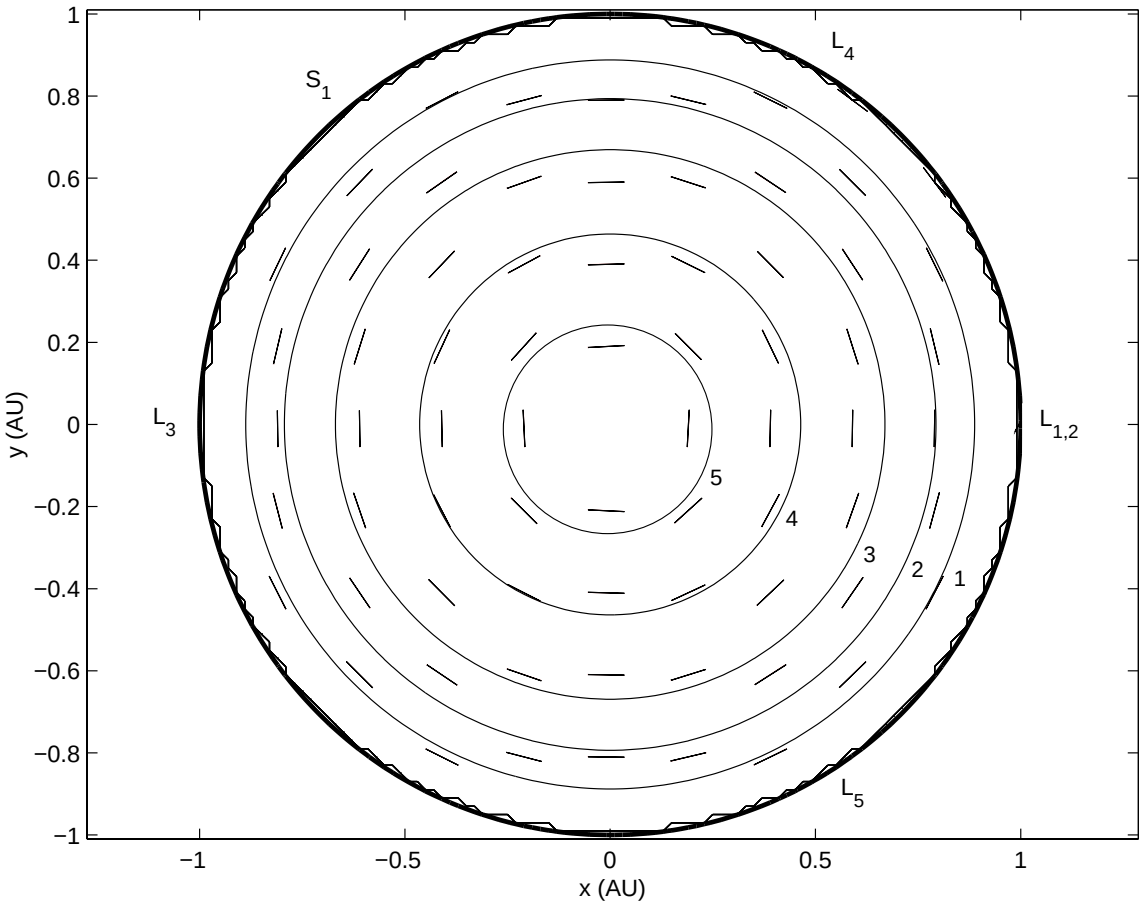

Figure 2.6. Section: libration point level surfaces; $\hat{x} - \hat{y}$ plane

Representative sail lightness values:

$1 : \beta = 0.3 \qquad 5 : \beta = 0.99$

$2 : \beta = 0.5$

$3 : \beta = 0.7$

$4 : \beta = 0.9$

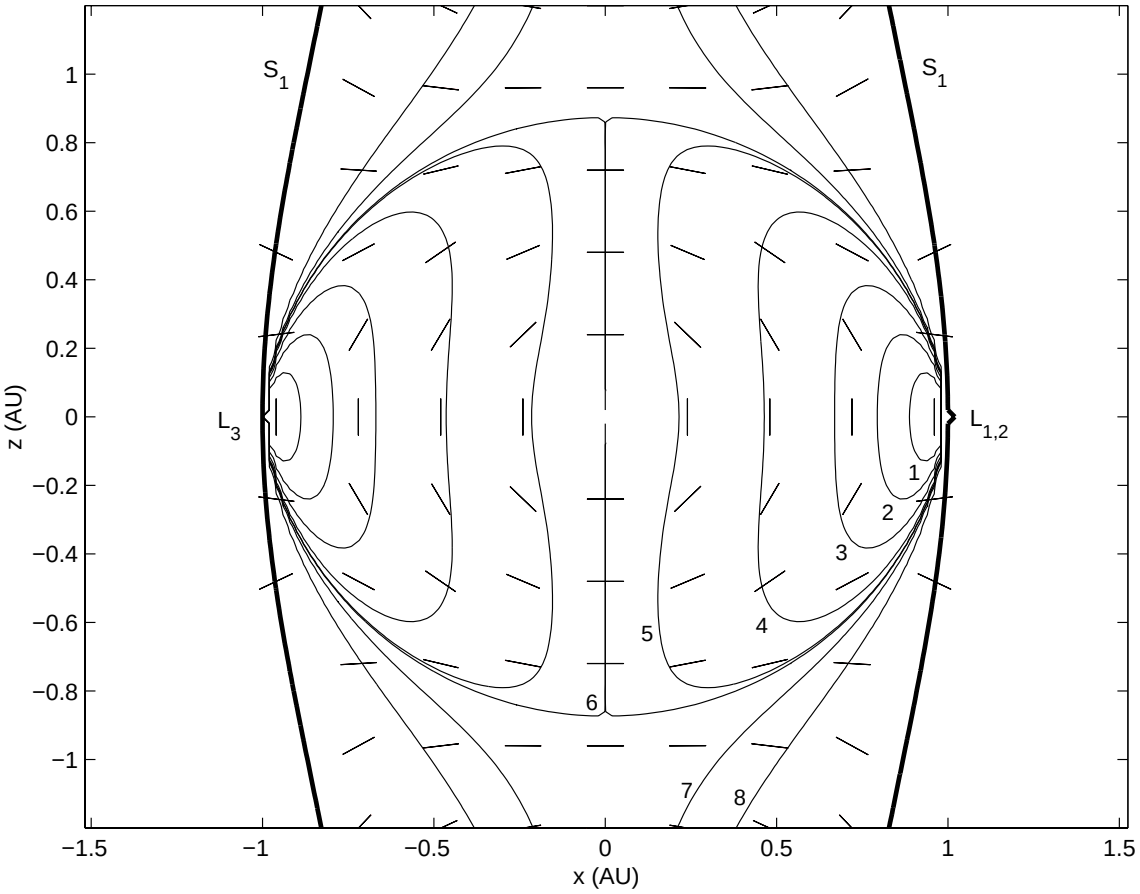

Figure 2.7. Section: libration point level surfaces; $\hat{x} - \hat{z}$ plane

Representative sail lightness values:

$1 : \beta = 0.3$ $\quad$ $5 : \beta = 0.99$

$2 : \beta = 0.5$ $\quad$ $6 : \beta = 1.0$

$3 : \beta = 0.7$ $\quad$ $7 : \beta = 1.1$

$4 : \beta = 0.9$ $\quad$ $8 : \beta = 1.5$

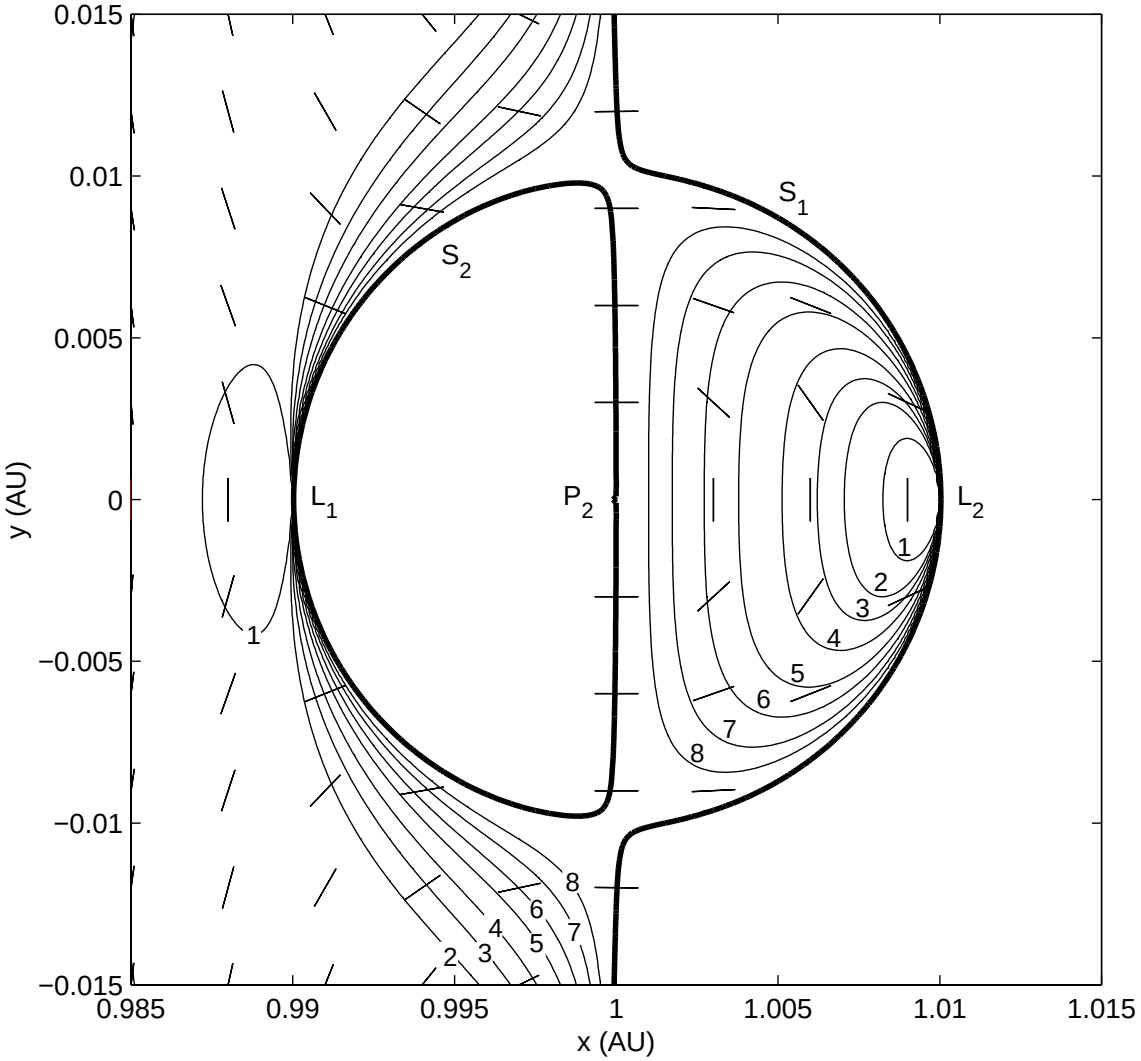

Figure 2.8. Libration point level surfaces in the vicinity of P_2; $\hat{x} - \hat{y}$ plane

Representative sail lightness values:

$1 : \beta = 0.02$ $\quad$ $5 : \beta = 0.2$

$2 : \beta = 0.04$ $\quad$ $6 : \beta = 0.4$

$3 : \beta = 0.06$ $\quad$ $7 : \beta = 1.0$

$4 : \beta = 0.1$ $\quad$ $8 : \beta = 3.0$

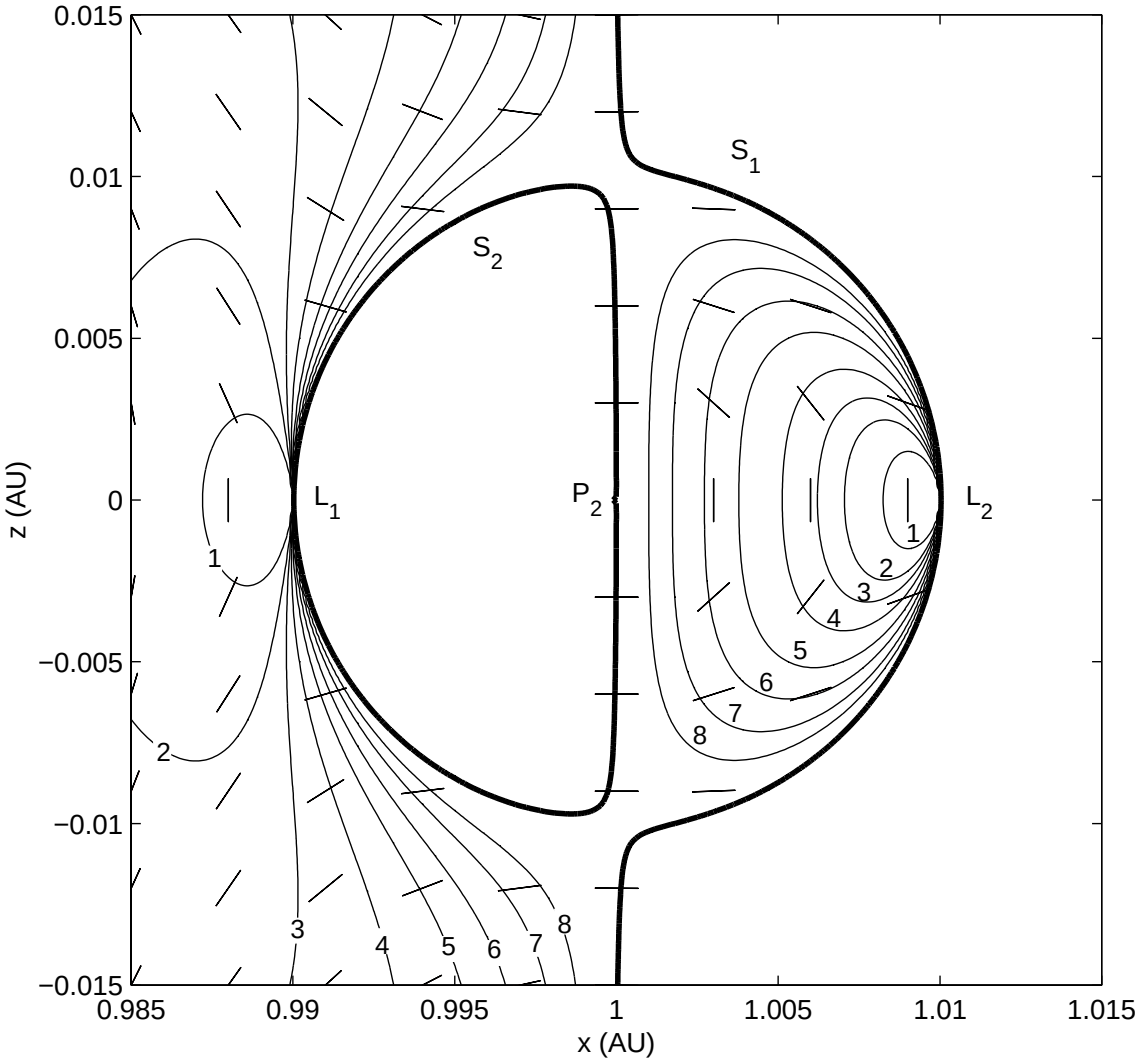

Figure 2.9. Libration point level surfaces in the vicinity of P_2; $\hat{x} - \hat{z}$ plane

Representative sail lightness values:

$1 : \beta = 0.02$ $\quad$ $5 : \beta = 0.2$

$2 : \beta = 0.04$ $\quad$ $6 : \beta = 0.4$

$3 : \beta = 0.06$ $\quad$ $7 : \beta = 1.0$

$4 : \beta = 0.1$ $\quad$ $8 : \beta = 3.0$

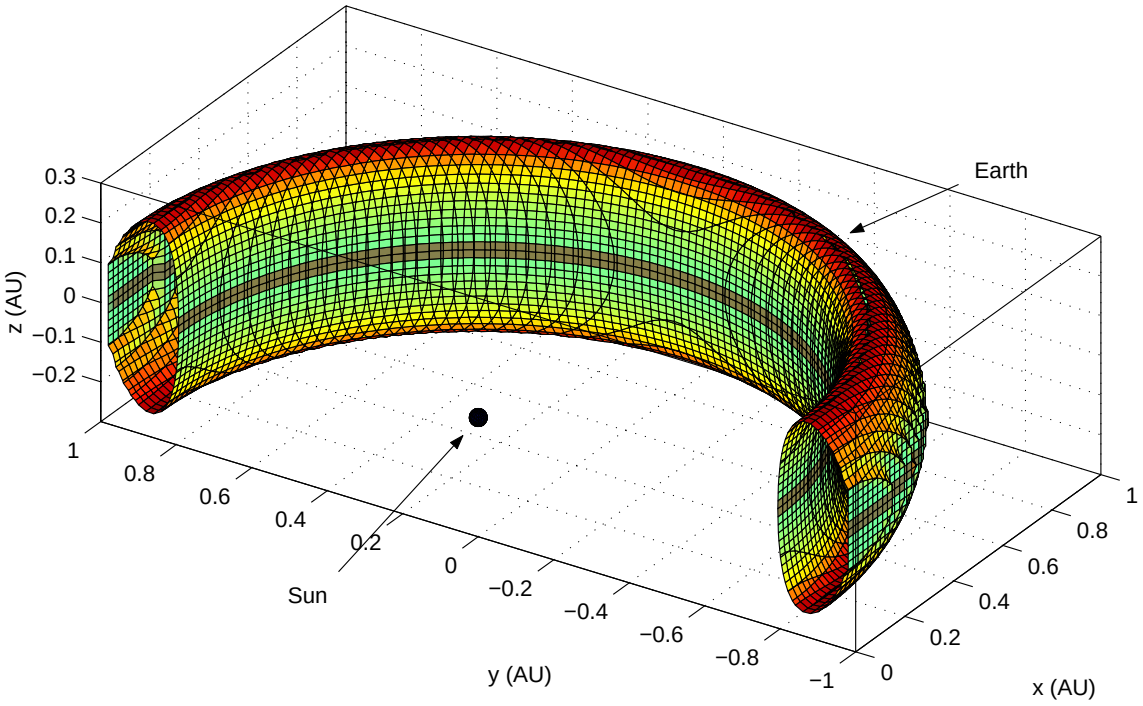

Figure 2.10. Artificial libration surface for $\beta = 0.5$; only half of the torus ($x > 0$) appears

3. On-Axis Solutions

The introduction of forces associated with a solar sail into the circular restricted three-body problem alters the properties of the dynamical system. A consequence of such a modification that is of particular interest to mission designers is the creation of a set of artificial libration points. The artificial libration points that lie along the $\hat{x}$-axis form a subset of the the complete new set of equilibrium points. The "on-axis" solutions originate with the classical collinear libration points and serve as a natural starting point in the study of the artificial libration points.

This chapter examines the effects of the introduction of solar sail forces on the position and stability of the on-axis libration points. An analytical approximation for periodic solutions about these new libration points is then developed. This approximation is used as an aid in initiating a numerical investigation of the new periodic solutions. The focus of the investigation is a study of the evolution of the shape of halo-type families of periodic orbits, and the stability of the orbits within the family, under the increasing influence of solar radiation pressure. Finally, a halo orbit stationkeeping algorithm, based on controlled variations in solar sail orientation, is formulated.

3.1 Effects of Solar Radiation Pressure on the Collinear Libration Points

3.1.1 Location of the Libration Points

For points along the $\hat{x}$-axis, $\overline{r}_1$, and, thus, $\hat{r}_1$, is parallel to the $\hat{x}$-axis. So, as is appropriate, the only non-zero component of $\overline{\nabla}U$ is U_x, the $\hat{x}$ component. Equation (2.66) then correctly yields

$$\hat{n}_{on-axis} = \pm\hat{x} \ . \tag{3.1}$$

To generate on-axis libration points, the sail cone angle $\alpha = 0°$, i.e., the sail is perpendicular to the Sun-spacecraft line (and, thus, γ is arbitrary). The scalar equations of motion then reduce, that is,

$$\ddot{x} - 2\dot{y} - x = -\frac{(1-\mu)(1-\beta)(x+\mu)}{r_1^3} - \frac{\mu(x-(1-\mu))}{r_2^3} , \tag{3.2}$$

$$\ddot{y} + 2\dot{x} - y = -\frac{(1-\mu)(1-\beta)y}{r_1^3} - \frac{\mu y}{r_2^3} , \tag{3.3}$$

$$\ddot{z} = -\frac{(1-\mu)(1-\beta)z}{r_1^3} - \frac{\mu z}{r_2^3} . \tag{3.4}$$

To examine the collinear points, note that the values $y = z = 0$ by definition. The location of the libration points on the $\hat{x}$-axis can then be determined from the solution of a single scalar equation,

$$x - \frac{(1-\mu)(1-\beta)(x+\mu)}{(x+\mu)^3} - \frac{\mu(x-(1-\mu))}{(x-(1-\mu))^3} = 0 . \tag{3.5}$$

Of course, this expression is very similar in form to the equivalent equation from the classical restricted three-body problem, differing only by the $(1-\beta)$ factor in the second term. Note that collinear solutions exist only for $\beta < 1$.

The solution of equation (3.5) requires determination of the roots of a fifth order polynomial in x. Typically, the equivalent expression in the classical restricted three-body problem is solved iteratively (e.g., using Newton's method) [6], and this technique is equally successful when the libration point locations are influenced by a solar sail force. The effect of solar radiation pressure can be quantified by solving equation (3.5) for various values of sail lightness. (See Figure 3.1.) As the sail lightness increases, the libration points move closer to the Sun, although this effect is much smaller in magnitude in the case of the L_2 libration point. These effects were previously noted in 1991 by Bell, for spacecraft influenced by solar radiation pressure [37].

3.1.2 Libration Point Stability

The similarity in form between equations (3.2), (3.3), and (3.4), and the classical differential equations corresponding to the restricted problem suggests that a quantity

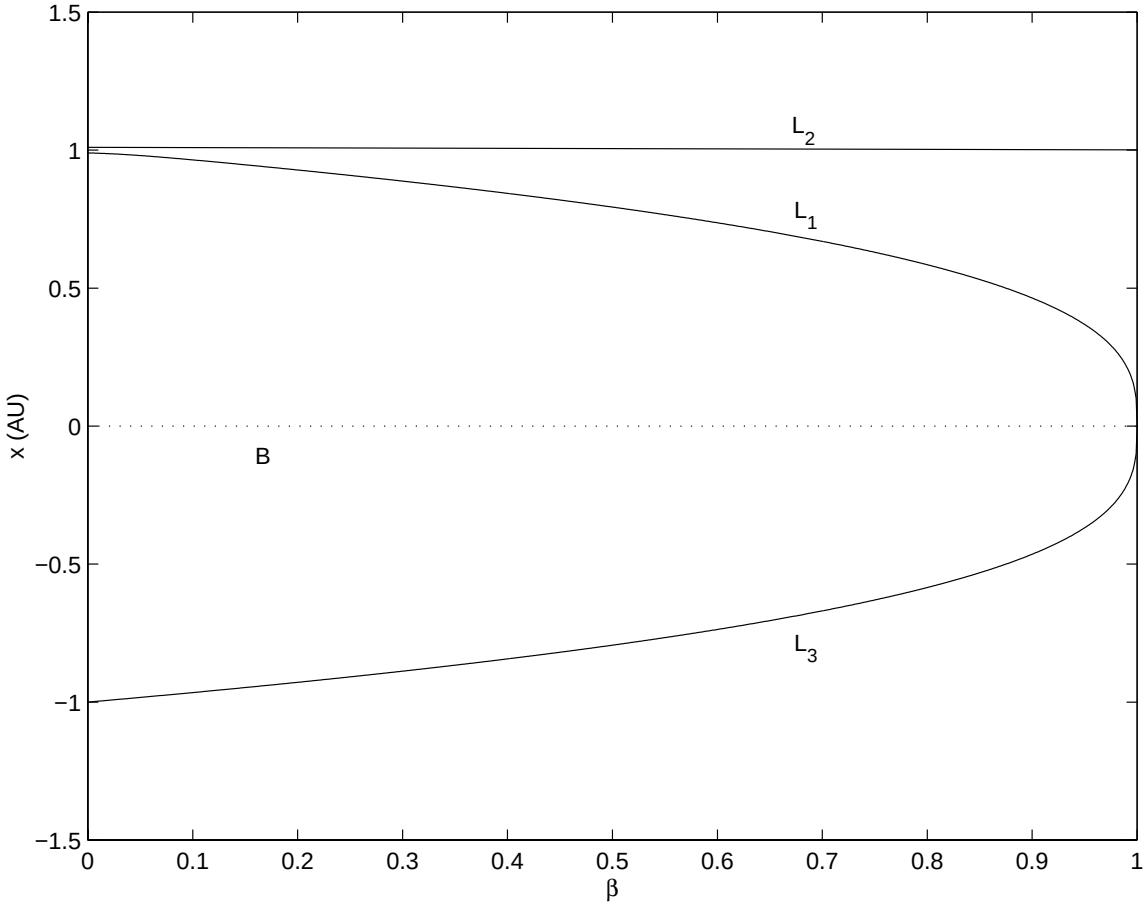

Figure 3.1. Evolution of the Sun-Earth collinear libration point locations with β

analogous to the pseudo-potential exists. The "modified pseudo-potential", Ω, is defined as,

$$\Omega = \frac{(1-\mu)(1-\beta)}{r_1} + \frac{\mu}{r_2} + \frac{1}{2}(x^2+y^2) \; . \tag{3.6}$$

The linear variational equations for motion relative to a libration point L_i are then, written in standard form,

$$\ddot{\xi} - 2\dot{\eta} = \Omega^*_{xx}\xi + \Omega^*_{xy}\eta + \Omega_{xz^*}\zeta \; , \tag{3.7}$$

$$\ddot{\eta} + 2\dot{\xi} = \Omega^*_{yx}\xi + \Omega^*_{yy}\eta + \Omega^*_{yz}\zeta \; , \tag{3.8}$$

$$\ddot{\zeta} = \Omega^*_{zx}\xi + \Omega^*_{zy}\eta + \Omega^*_{zz}\zeta \; , \tag{3.9}$$

where $\Omega_{jk} = \frac{\partial \Omega}{\partial j \partial k}$ and $\Omega^*_{jk} = \Omega_{jk}|_{L_i}$. The expressions for these partial derivatives appear in Appendix C.

By definition, the collinear points lie on the $\hat{x}$-axis, and, thus,

$$\Omega^*_{xy} = \Omega^*_{yx} = \Omega^*_{xz} = \Omega^*_{zx} = \Omega^*_{yz} = \Omega^*_{zy} = 0 \; . \tag{3.10}$$

This results in a differential equation for the out-of-plane motion, ζ, that is decoupled from the in-plane motion represented by ξ and η. First, consider the out-of-plane behavior. Since $M_1 > M_2$, the mass ratio $\mu < \frac{1}{2}$. Also, as stated previously, $\beta < 1$ for the collinear points. Therefore,

$$\Omega^*_{zz} = -\frac{(1-\mu)(1-\beta)}{r_1^3} - \frac{\mu}{r_2^3} < 0 \; , \tag{3.11}$$

and the characteristic equation resulting from equation (3.9),

$$s^2 = \Omega^*_{zz} \; , \tag{3.12}$$

and, thus, the characteristic roots associated with ζ are purely imaginary.

The analysis of the in-plane motion is similar to that presented in [6] for the classical three-body problem. The non-zero terms that remain in the system of equations for in-plane $(\xi - \eta)$ motion simplify to,

$$\Omega^*_{xx} = 1 + \frac{2(1-\mu)(1-\beta)}{r_1^3} + \frac{2\mu}{r_2^3} > 0 \; , \tag{3.13}$$

$$\Omega^*_{yy} = 1 - \frac{(1-\mu)(1-\beta)}{r_1^3} - \frac{\mu}{r_2^3} < 0 \; . \tag{3.14}$$

The corresponding characteristic equation for this system appears as follows,

$$s^4 + (4 - \Omega^*_{xx} - \Omega^*_{yy})s^2 + \Omega^*_{xx}\Omega^*_{yy} = 0 \ . \tag{3.15}$$

Making the substitution $S = s^2$, equation (3.15) can be rewritten in the form

$$S^2 + 2\Lambda_1 S - \Lambda_2^2 = 0 \ , \tag{3.16}$$

where,

$$\Lambda_1 = 2 - \frac{\Omega^*_{xx} + \Omega^*_{yy}}{2} \ , \tag{3.17}$$

$$\Lambda_2^2 = -\Omega^*_{xx}\Omega^*_{yy} > 0 \ . \tag{3.18}$$

The roots of equation (3.16) are real and of opposite sign:

$$S_1 = -\Lambda_1 + (\Lambda_1^2 + \Lambda_1^2)^{1/2} > 0 \ , \tag{3.19}$$

$$S_2 = -\Lambda_1 - (\Lambda_1^2 + \Lambda_1^2)^{1/2} < 0 \ . \tag{3.20}$$

and, thus, the four characteristic roots for the $\xi - \eta$ system, $s = (\pm {S_1}^{1/2}, \ \pm {S_2}^{1/2})$, include two real and two pure imaginary roots.

The characteristic roots determined in equations (3.12), (3.19), and (3.20) are associated with the variational equations that incorporate the solar sail force, and, thus, correspond to the artificial on-axis libration points. Note that these "new" roots are actually of the same form as those determined for the classical collinear points [6]. Therefore, the qualitative stability of the on-axis libration points, influenced by the force representing a solar sail, is similar to stability information derived in the classical system. Of particular interest is the survival of the pure imaginary roots, with the obvious implication that the periodic halo orbits that exist in the vicinity of the classical collinear points may be preserved in some modified form.

3.2 A Modified Analytical Halo Approximation

Recall Richardson's third-order halo orbit approximation [18],

$$\xi = a_{21}A_x^2 + a_{22}A_z^2 - A_x \cos(\lambda\tau + \phi) + (a_{23}A_x^2 - a_{24}A_z^2)\cos(2\lambda\tau + 2\phi)$$

$$+(a_{31}A_x^3 - a_{32}A_xA_z^2)\cos(3\lambda\tau + 3\phi) \ , \tag{3.21}$$

$$\eta = kA_x\sin(\lambda\tau+\phi) + (b_{21}A_x^2 - b_{22}A_z^2)\sin(2\lambda\tau+2\phi)$$
$$+(b_{31}A_x^3 - b_{32}A_xA_z^2)\sin(3\lambda\tau+3\phi) \ , \tag{3.22}$$

$$\zeta = \delta_n A_z\cos(\lambda\tau+\phi) + \delta_n d_{21}A_xA_z(cos(2\lambda\tau+2\phi) - 3)$$
$$+\delta_n(d_{32}A_zA_x^2 - d_{31}A_z^3)\cos(3\lambda\tau+3\phi) \ . \tag{3.23}$$

This approximate solution is based on a Legendre polynomial expansion of the Lagrangian for the motion of P_3 relative to the libration point. Since the coefficients in this approximation are functions of c_n, that is, the coefficients of the expansion of the Lagrangian (see Appendix B), the approximation is actually a general third-order algebraic solution for systems possessing a Lagrangian that can be expressed in the form

$$\mathcal{L} = \frac{1}{2}(\dot{\overline{\rho}}\cdot\dot{\overline{\rho}}) + \sum_{n=2}^{\infty} c_n\rho^n P_n(\xi/\rho) \ , \tag{3.24}$$

where the position vector $\overline{\rho} = \xi\hat{x} + \eta\hat{y} + \zeta\hat{z}$, $\rho = |\overline{\rho}|$, and $P_n(\xi/\rho)$ is the nth Legendre polynomial of the first kind with argument ξ/ρ. Additionally, the nonlinear system for which an approximation is sought must have a first-order periodic solution, since the approximation scheme relies on the use of a first-order "guess" as a generating solution.

As has been demonstrated previously, the equations of motion for a solar sail in the vicinity of the on-axis libration points can be reduced to a form very similar to that of the classical circular restricted three-body problem. Also, as noted in the previous section, the stability properties of the variational equations that result from the linearization process are such that a first-order periodic solution is available. Proceeding with an analysis similar to that in [40], the Lagrangian for motion in the vicinity of an on-axis libration point, incorporating the effects of a solar sail force, can be developed in terms of the perturbing potentials due to the gravitational fields of P_1 and P_2.

Given that for on-axis libration points $\alpha = 0°$, equations (2.3) and (2.52) can be

combined to yield a vector equation for the motion of P_3 in the inertial frame,

$$M_3 \frac{{}^I d^2\overline{R}}{dt^2} = -\frac{GM_1M_3}{R_1^3}\overline{R}_1 - \frac{GM_2M_3}{R_2^3}\overline{R}_2 + \beta\frac{GM_1M_3}{R_1^3}\overline{R}_1 \ . \tag{3.25}$$

Applying Newton's Law of Gravity, the expression for the motion of P_1 is

$$M_1 \frac{{}^I d^2\overline{d}_1}{dt^2} = \frac{GM_1M_3}{R_1^3}\overline{R}_1 + \frac{GM_1M_2}{R_{12}^3}\overline{R}_{12} \ , \tag{3.26}$$

where $\overline{d}_1$ is the position vector of P_1 as defined in Figure 2.1, and $R_{12} = \overline{d}_2 - \overline{d}_1$. Utilizing the assumption that $M_3 \ll M_2 < M_1$, and equations (3.25) and (3.26), the motion of P_3 relative to P_1 is described by the expression,

$$\frac{{}^I d^2\overline{R}_1}{dt^2} = \frac{{}^I d^2\overline{R}}{dt^2} - \frac{{}^I d^2\overline{d}_1}{dt^2} = -GM_1\frac{(1-\beta)}{R_1^3}\overline{R}_1 + GM_2\left[\frac{\overline{R}_{12} - \overline{R}_1}{|\overline{R}_{12} - \overline{R}_1|^3} - \frac{\overline{R}_{12}}{R_{12}^3}\right] \ . \tag{3.27}$$

Note that the substitution $-\overline{R}_2 = \overline{R}_{12} - \overline{R}_1$ has been employed to reduce the number of different vectors in the expression.

Using the characteristic quantities and nondimensional variables previously defined for the classical restricted three-body problem, equation (3.27) can be rewritten in nondimensional form as

$$\frac{{}^I d^2\overline{r}_1}{dt^2} = -(1-\mu)\frac{(1-\beta)}{r_1^3}\overline{r}_1 + \mu\left[\frac{\overline{r}_{12} - \overline{r}_1}{|\overline{r}_{12} - \overline{r}_1|^3} - \frac{\overline{r}_{12}}{r_{12}^3}\right] \ , \tag{3.28}$$

where $\overline{r}_{12} = \frac{\overline{R}_{12}}{L^*}$. The Lagrangian associated with the motion of P_3 relative to P_1 can then be written as follows,

$$\mathcal{L}_{P_1} = \frac{1}{2}(\dot{\overline{r}}_1 \cdot \dot{\overline{r}}_1) + (1-\mu)\frac{(1-\beta)}{r_1} + \mu\left[\frac{1}{|\overline{r}_{12} - \overline{r}_1|^3} - \frac{\overline{r}_{12}\cdot\overline{r}_1}{r_{12}^3}\right] \ , \tag{3.29}$$

where the over-dot (e.g., $\dot{\overline{r}}_1$) indicates differentiation with respect to time, and in the inertial frame.

As stated previously, the nondimensional angular velocity of the synodic frame relative to the inertial frame is ${}^I\overline{\omega}^S = \hat{z}$. Thus, expanding the kinematic expression on the left hand side of equation (3.28) results in the following,

$$\frac{{}^I d^2\overline{r}_1}{dt^2} = \frac{{}^S d^2\overline{r}_1}{dt^2} + 2\hat{z} \times \frac{{}^S d\overline{r}_1}{dt} - \overline{r}_1 \ . \tag{3.30}$$

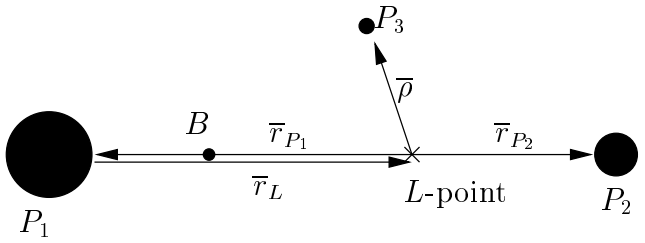

Figure 3.2. Geometric relationships between the three bodies and a libration point

Let a libration point L_i be located relative to P_1 by the vector $\overline{r}_L$, as it appears in Figure 3.2. At the libration point, $\frac{{}^S d^2\overline{r}_1}{dt^2} = \frac{{}^S d\overline{r}_1}{dt} = 0$, and, therefore, from equations (3.28) and (3.30),

$$\overline{r}_L - (1-\mu)\frac{(1-\beta)}{r_L^3}\overline{r}_L + \mu\left[\frac{\overline{r}_{12} - \overline{r}_L}{|\overline{r}_{12} - \overline{r}_L|^3} - \frac{\overline{r}_{12}}{r_{12}^3}\right] = 0 \ . \tag{3.31}$$

Solving equation (3.31) for $\frac{\overline{r}_{12}}{r_{12}^3}$ yields,

$$\frac{\overline{r}_{12}}{r_{12}^3} = \mu^{-1}\overline{r}_L - \mu^{-1}(1-\mu)\frac{(1-\beta)}{r_L^3}\overline{r}_L + \frac{\overline{r}_{12} - \overline{r}_L}{|\overline{r}_{12} - \overline{r}_L|^3} \ . \tag{3.32}$$

Substituting this expression into equation (3.29), and defining the vectors (as seen in Figure 3.2),

$$\begin{aligned} \overline{r}_{P_1} &= -\overline{r}_L \ , \\ \overline{r}_{P_2} &= \overline{r}_{12} - \overline{r}_L \ , \\ \overline{\rho} &= \overline{r}_1 - \overline{r}_L \ , \end{aligned}$$

allows the Lagrangian to be rewritten as

$$\begin{aligned} \mathcal{L}_{P_1} &= \frac{1}{2}(\dot{\overline{\rho}}\cdot\dot{\overline{\rho}}) - \dot{\overline{r}}_{P_1}\cdot\dot{\overline{\rho}} + \overline{r}_{P_1}\cdot\overline{\rho} + (1-\mu)(1-\beta)\left[\frac{1}{|\overline{r}_{P_1} - \overline{\rho}|} - \frac{\overline{r}_{P_1}\cdot\overline{\rho}}{|\overline{r}_{P_1}|^3}\right] \\ &\quad + \mu\left[\frac{1}{|\overline{r}_{P_2} - \overline{\rho}|} - \frac{\overline{r}_{P_2}\cdot\overline{\rho}}{|\overline{r}_{P_2}|^3}\right] + \text{ constant terms} \ . \end{aligned} \tag{3.33}$$

From equation (3.30), at a libration point ($\overline{r}_1 \equiv \overline{r}_{P_1}$),

$$\frac{{}^I d^2\overline{r}_1}{dt^2} = -\overline{r}_1 \ , \tag{3.34}$$

and, thus, the second and third terms of equation (3.33) can be combined to form the identity,

$$-\dot{\overline{r}}_{P_1}\cdot\dot{\overline{\rho}} + \overline{r}_{P_1}\cdot\overline{\rho} \equiv -\frac{{}^I d}{dt}(\overline{\rho}\cdot\dot{\overline{r}}_{P_1}) \ . \tag{3.35}$$

Then, from equation (3.33), it is possible to write,

$$\mathcal{L} \equiv \mathcal{L}_{P_1} + \frac{d}{dt}(\overline{\rho} \cdot \dot{\overline{r}}_{P_1}) \; . \tag{3.36}$$

This expression possesses a form corresponding to a canonical transformation. Selecting the identity transformation as the most straightforward coordinate change, the new Lagrangian is,

$$\begin{aligned} \mathcal{L} &= \frac{1}{2}(\dot{\overline{\rho}} \cdot \dot{\overline{\rho}}) + (1-\mu)(1-\beta)\left[\frac{1}{|\overline{r}_{P_1} - \overline{\rho}|} - \frac{\overline{r}_{P_1} \cdot \overline{\rho}}{|\overline{r}_{P_1}|^3}\right] \\ &\quad + \mu\left[\frac{1}{|\overline{r}_{P_2} - \overline{\rho}|} - \frac{\overline{r}_{P_2} \cdot \overline{\rho}}{|\overline{r}_{P_2}|^3}\right] \; . \end{aligned} \tag{3.37}$$

This closely resembles the Lagrangian developed by Richardson for the classical system.

Given the Lagrangian of of the form in equation (3.37), the expansion of the Lagrangian into a Legendre polynomial power series is accomplished for the interior and exterior libration points. In the case of an interior (L_1) libration point, define the dimensionless ratio γ_L as follows, i.e.,

$$\gamma_L \equiv \frac{r_{P_2}}{(d_1 + d_2)} \; ,$$

where $(d_1 + d_2)$ is the distance between the primaries. Using this definition, the vectors from the libration point to each primary become,

$$\overline{r}_{P_1} = -(1-\gamma_L)\hat{x} \; , \tag{3.38}$$

$$\overline{r}_{P_2} = \gamma_L \hat{x} \; . \tag{3.39}$$

The Lagrangian can then be rewritten as,

$$\begin{aligned} \mathcal{L} &= \frac{1}{2}(\dot{\overline{\rho}} \cdot \dot{\overline{\rho}}) + (1-\mu)(1-\beta)\left[\frac{1}{\sqrt{(-(1-\gamma_L) - \xi)^2 + \eta^2 + \zeta^2}} + \frac{(1-\gamma_L)\xi}{(1-\gamma_L)^3}\right] \\ &\quad + \mu\left[\frac{1}{\sqrt{(\gamma_L - \xi)^2 + \eta^2 + \zeta^2}} - \frac{\gamma_L \xi}{\gamma_L^3}\right] \; . \end{aligned} \tag{3.40}$$

It is known [42] that a function having the form,

$$\frac{1}{\sqrt{1 - 2qu + u^2}} \; ,$$

can be expressed as a Legendre polynomial series such that,

$$\frac{1}{\sqrt{1-2qu+u^2}} = \sum_{n=0}^{\infty} P_n(q)u^n \ , \tag{3.41}$$

where $P_n(q)$ denotes a Legendre polynomial of the first kind, with argument q. Note also that $P_0(q) = 1$, and $P_1(q) = q$. Thus, define $q = \xi/\rho$, and $u = -\rho/(1-\gamma_L)$; the the first bracketed term in equation (3.40) becomes

$$\begin{aligned}
\left[\frac{1}{\sqrt{(-(1-\gamma_L)-\xi)^2+\eta^2+\zeta^2}} \ + \ \frac{(1-\gamma_L)\xi}{(1-\gamma_L)^3}\right] & \\
= \ & \left[\frac{1}{(1-\gamma_L)\sqrt{1+2\frac{\xi}{(1-\gamma_L)}+\frac{\rho^2}{(1-\gamma_L)^2}}}\right. \\
& \left. + \ \frac{\xi}{(1-\gamma_L)^2}\right] \ , \qquad (3.42) \\
= \ & \frac{1}{(1-\gamma_L)}\left[\frac{1}{\sqrt{1-2qu+u^2}} - qu\right] \ , \qquad (3.43) \\
= \ & \frac{1}{(1-\gamma_L)}\left[\sum_{n=2}^{\infty} P_n(q)u^n - 1\right] \ , \qquad (3.44) \\
= \ & \left[\sum_{n=2}^{\infty} \frac{(-1)^n\rho^n}{(1-\gamma_L)^{n+1}} P_n(\xi/\rho) - \frac{1}{(1-\gamma_L)}\right] . \qquad (3.45)
\end{aligned}$$

Similarly, again let $q = \xi/\rho$, and $u = \rho/\gamma_L$, and the second bracket in equation (3.40) yields

$$\begin{aligned}
\left[\frac{1}{\sqrt{(\gamma_L-\xi)^2+\eta^2+\zeta^2}} - \frac{\gamma_L\xi}{\gamma_L^3}\right] \ = \ & \left[\frac{1}{\gamma_L\sqrt{1-2\frac{\xi}{\gamma_L}+\frac{\rho^2}{\gamma_L^2}}} + \frac{\xi}{\gamma_L^2}\right] \ , \qquad (3.46) \\
= \ & \frac{1}{\gamma_L}\left[\frac{1}{\sqrt{1-2qu+u^2}} - qu\right] \ , \qquad (3.47) \\
= \ & \frac{1}{\gamma_L}\left[\sum_{n=2}^{\infty} P_n(q)u^n - 1\right] \ , \qquad (3.48) \\
= \ & \left[\sum_{n=2}^{\infty} \frac{\rho^n}{\gamma_L^{n+1}} P_n(\xi/\rho) - \frac{1}{\gamma_L}\right] . \qquad (3.49)
\end{aligned}$$

The Lagrangian in equation (3.40) can then be rewritten as follows,

$$\begin{aligned}\mathcal{L} &= \frac{1}{2}(\dot{\overline{\rho}}\cdot\dot{\overline{\rho}}) + (1-\mu)(1-\beta)\left[\sum_{n=2}^{\infty}\frac{(-1)^n\rho^n}{(1-\gamma_L)^{n+1}}P_n(\xi/\rho)\right] \\ &\quad + \mu\left[\sum_{n=2}^{\infty}\frac{\rho^n}{\gamma_L^{n+1}}P_n(\xi/\rho)\right] + \text{constant terms} . \qquad (3.50)\end{aligned}$$

Thus, the modified expression for the expansion coefficient, c_n, is

$$c_n = \left[\frac{(-1)^n(1-\mu)(1-\beta)}{(1-\gamma_L)^{n+1}} + \frac{\mu}{\gamma_L^{n+1}}\right] . \qquad (3.51)$$

The coefficients for the L_2 and L_3 libration points can be derived in a similar fashion. Thus, for an L_2 libration point (i.e., exterior to P_2), γ_L is defined as

$$\gamma_L \equiv \frac{r_{P_2}}{(d_1+d_2)} ,$$

and, thus, $\overline{r}_{P_1}$ and $\overline{r}_{P_2}$ are redefined as

$$\overline{r}_{P_1} = -(1+\gamma_L)\hat{x} , \qquad (3.52)$$

$$\overline{r}_{P_2} = -\gamma_L\hat{x} . \qquad (3.53)$$

The expansion coefficient for this case is then,

$$c_n = \left[\frac{(-1)^n(1-\mu)(1-\beta)}{(1+\gamma_L)^{n+1}} + \frac{(-1)^n\mu}{\gamma_L^{n+1}}\right] . \qquad (3.54)$$

In the case of an L_3 libration point (i.e., exterior to P_1),

$$\gamma_L \equiv \frac{r_{P_1}}{(d_1+d_2)} ,$$

and,

$$\overline{r}_{P_1} = \gamma_L\hat{x} , \qquad (3.55)$$

$$\overline{r}_{P_2} = (1+\gamma_L)\hat{x} . \qquad (3.56)$$

The resulting expansion coefficient is then,

$$c_n = \left[\frac{(1-\mu)(1-\beta)}{\gamma_L^{n+1}} + \frac{\mu}{(1+\gamma_L)^{n+1}}\right] . \qquad (3.57)$$

Note that these expressions are derived in terms of the nondimensional units introduced previously, rather than Richardson's normalized units, and, thus, the approximate solutions resulting from the use of these modified coefficients will also be in the same nondimensional units.

The new coefficients obtained from equations (3.51), (3.54), and (3.57) can be substituted into the expressions in Appendix B to generate approximate solutions for periodic orbits near the artificial on-axis libration points that result from the introduction of a solar sail force. These periodic solutions retain the sail orientation assumption upon which the approximation is constructed, that is, $\alpha = 0^\circ$ along the entire solution. Examples of third-order approximations are presented in Figures 3.3 and 3.4; these plots represent periodic solar sail orbits in the vicinity of the modified L_1 and L_2 libration points. Approximate solutions generated as a result of this scheme have been successfully used as initial guesses for the numerical generation of precisely periodic orbits.

3.3 Families of Periodic Orbits

3.3.1 Generation of Families

Using the the modified third-order approximation to generate initial guesses for periodic halo orbits, a differential corrections scheme (as outlined in section 2.1.7) is applied to obtain numerically integrated periodic solutions to the three-body equations of motion that include a solar sail force. Recall that the differential corrections procedure relies on the state transition matrix, $\mathbf{\Phi}(t_f, t_0)$, which is obtained by numerically integrating the system of 36 differential equations represented by

$$\dot{\mathbf{\Phi}}(t, t_0) = \mathbf{A}(t)\mathbf{\Phi}(t, t_0) \ , \quad \mathbf{\Phi}(t_0, t_0) = \mathbf{I}_6 \ . \tag{3.58}$$

Consistent with the previous discussion, the matrix $\mathbf{A}(t)$ appears in the general form

$$\mathbf{A}(t) \equiv \begin{bmatrix} \mathbf{0} & \mathbf{I}_3 \\ \mathbf{B}(t) & \mathbf{C} \end{bmatrix} \ ,$$

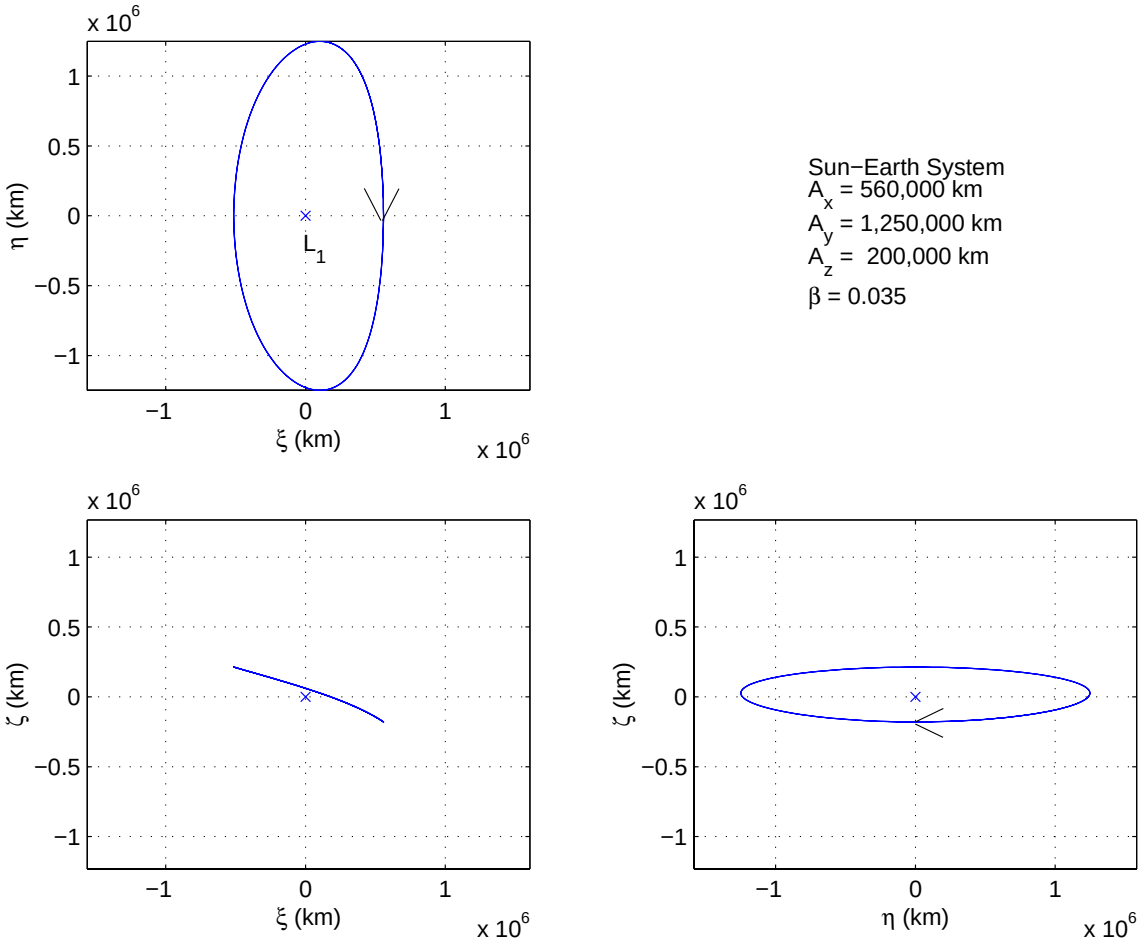

Figure 3.3. Example: Third-order Sun-Earth L_1 solar sail halo orbit approximation

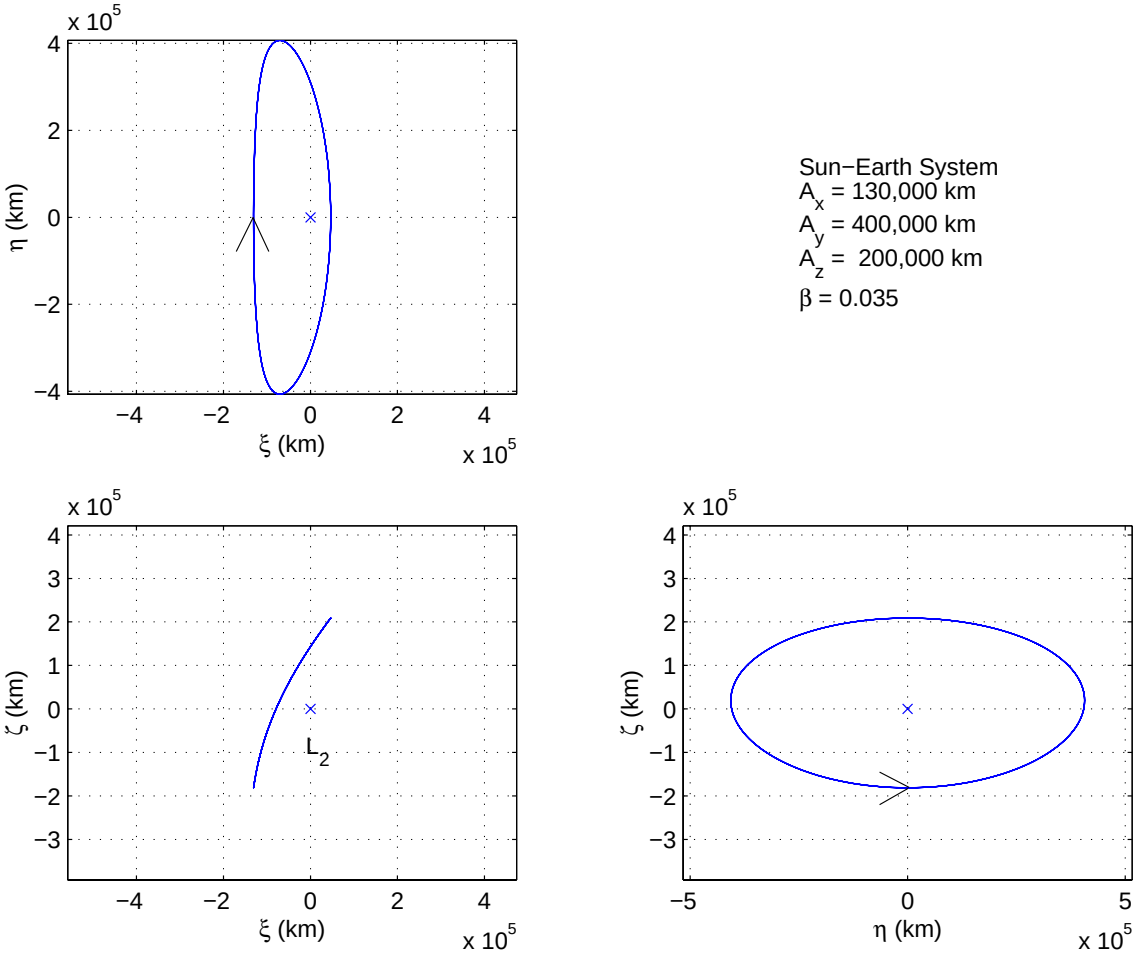

Figure 3.4. Example: Third-order Sun-Earth L_2 solar sail halo orbit approximation

where $\mathbf{A}(t)$ is expressed in terms of four 3×3 submatrices. However, the addition of a solar sail force alters the elements in the submatrix $\mathbf{B}(t)$ such that

$$\mathbf{B}(t) \equiv \begin{bmatrix} U_{xx} + a_{xx} & U_{xy} + a_{xy} & U_{xz} + a_{xz} \\ U_{yx} + a_{yx} & U_{yy} + a_{yy} & U_{yz} + a_{yz} \\ U_{zx} + a_{zx} & U_{zy} + a_{zy} & U_{zz} + a_{zz} \end{bmatrix},$$

where $a_{jk} = \frac{\partial a_j}{\partial k}$. The expressions for the partial derivatives of a_x, a_y, and a_z are straightforward, and appear in Appendix D. Given the modified elements of matrix $\mathbf{B}(t)$, the state transition matrix is now computed for a trajectory that includes the effects of a solar sail force. Numerically generated halo orbits appear in Figure 3.5 for several values of β. Note that the differential corrections process is structured in this example to maintain a fixed maximum z-value (A_z) in all orbits. As with the approximate solutions, $\alpha = 0^\circ$ along the entire orbit, and, thus, the value of γ is irrelevant. For the trajectories presented in Figure 3.5, γ is arbitrarily set to zero.

From the example orbits in Figure 3.5, it is apparent that the addition of a solar sail shifts the libration point, but it can also alter the characteristics of the periodic orbits. As noted by Nuss [38], for an L_1 halo of a given maximum out-of-plane excursion (A_z), an increase in the lightness parameter β results in a corresponding increase in the in-plane amplitude as well as the period. In the case of L_2 halo orbits, increasing the sail lightness parameter causes a decrease in the in-plane amplitude and the period. Figure 3.6 illustrates these effects for a Sun-Earth L_1 halo with an A_z amplitude of 450,000 km.

The result of an increase in the value of the sail lightness parameter for a given periodic trajectory is a significant change in the size and character of the orbit. This implies that the characteristics of the entire family of periodic halo orbits will change as a solar sail force is introduced. For the purposes of this investigation, families of periodic orbits are computed by first generating a near-planar orbit for various values of β, using the modified third-order approximation to obtain an initial guess, and then utilizing numerical continuation to produce additional members of the family from the initial orbit. Recall that the periodic orbits are computed with the assumption

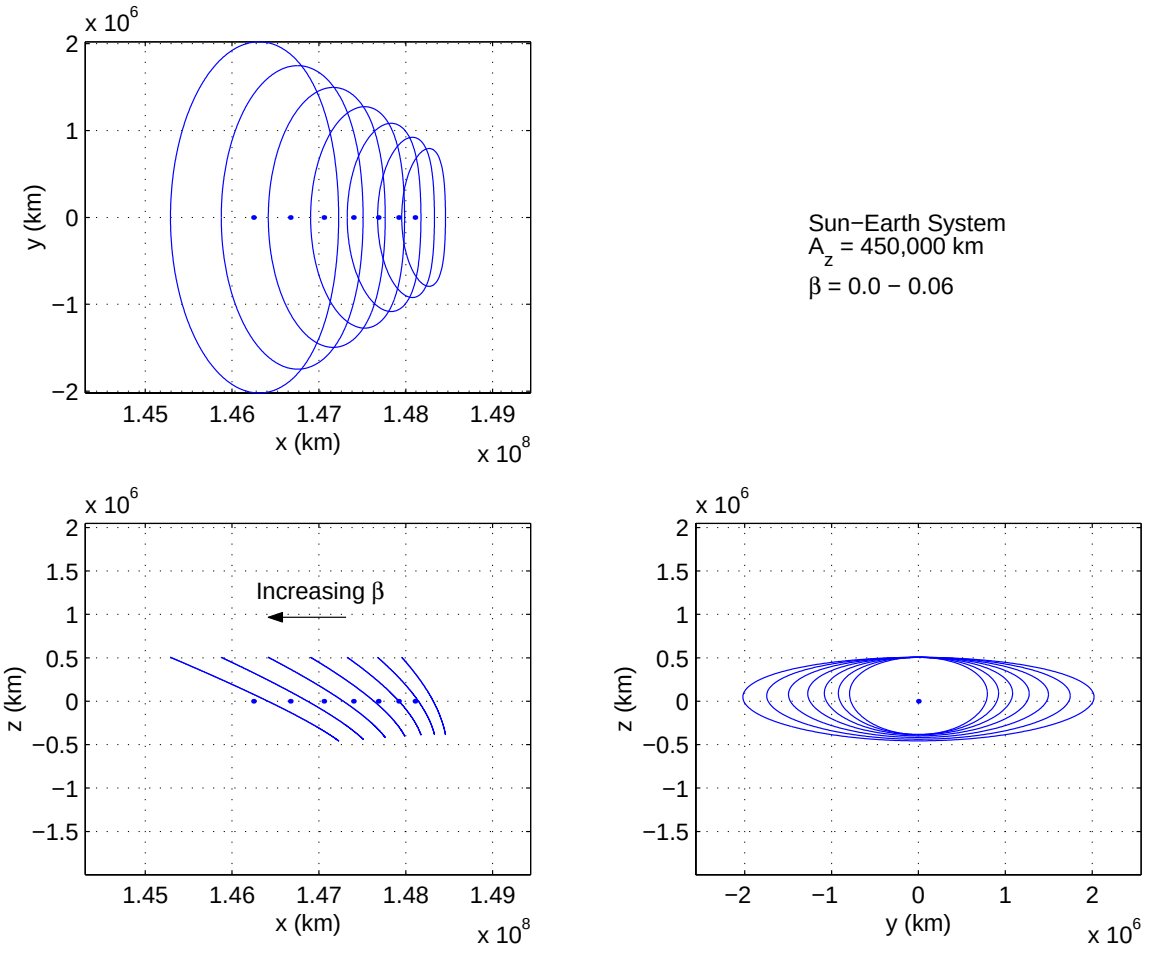

Figure 3.5. Evolution of Sun-Earth L_1 halo orbits with sail lightness β

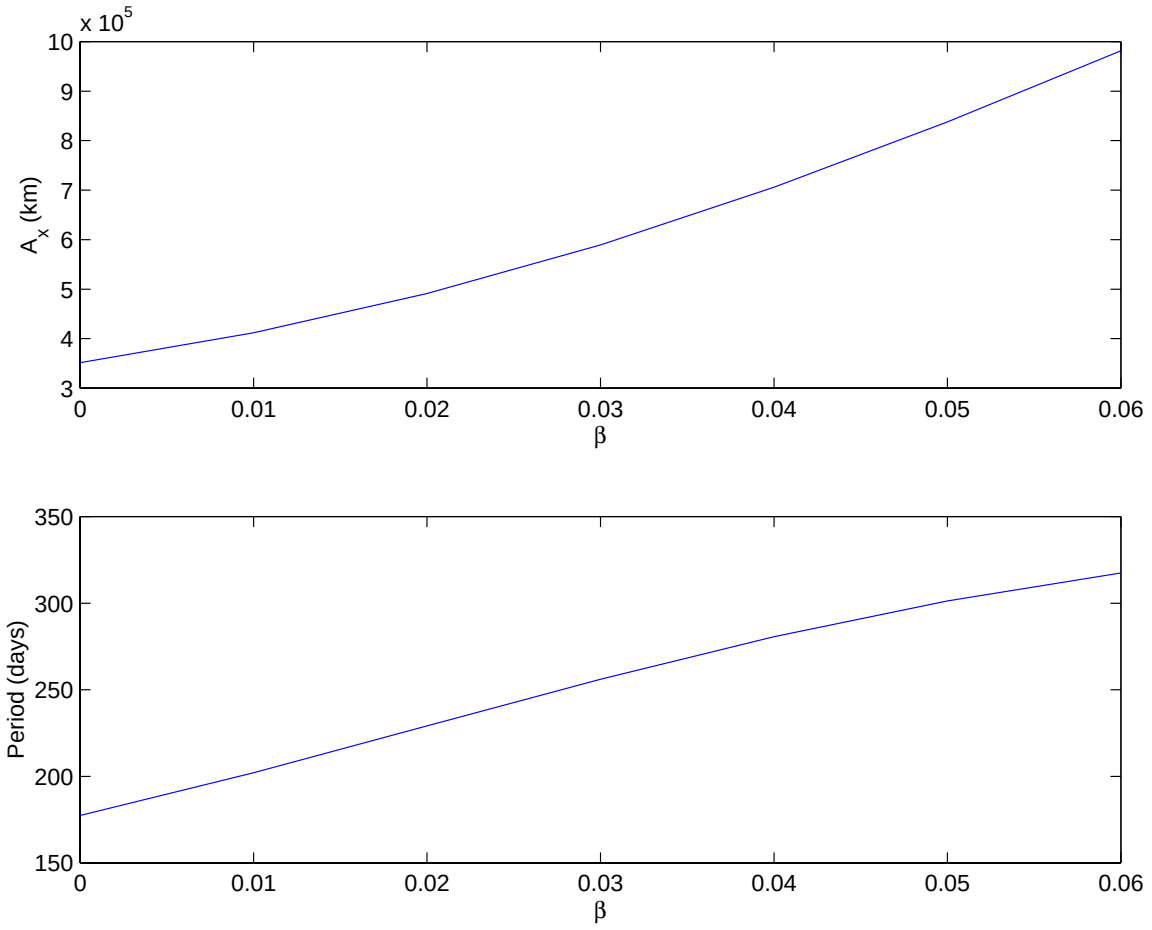

Figure 3.6. Effects of β on L_1 halo orbit amplitude and period

that the sail orientation is such that $\alpha = 0°$, that is, $\hat{n}$ remains parallel to $\overline{r}_1$.

Members of the classical L_1 halo family are plotted in Figure 3.7. The plot is produced using the technique outlined above. The next two figures, Figure 3.8 and Figure 3.9, demonstrate how the introduction of a solar sail can alter the shape of the halo family. Note that the numerical continuation process involves making a small change in some element of the initial state, and computing a new periodic orbit from the modified initial state. Thus, to prevent the computation of the new orbit from converging to the previous orbit, the differential corrector is now structured

such that the element of the initial state that is modified as part of the continuation process is held fixed during the corrections process. An interesting development is the appearance of "L_1" halo orbits that pass beyond Earth's orbit. (See Figure 3.9.) Periodic orbits from L_2 families appear in Figures 3.10 and 3.11. The classical family in Figure 3.10 evolves into a family that incorporates a solar sail force in Figure 3.11. It is apparent that the qualitative "shape" of the L_2 family is not as dramatically affected as the shape characteristics of the L_1 family by the introduction of a solar sail.

The periodic orbits in the vicinity of the on-axis libration points are symmetric about the $\hat{x} - \hat{z}$ plane. Thus, one method to characterize the shape of a halo family is to examine the intersection of the family with the plane of symmetry. This reduces the representation of the family of periodic orbits to a pair of curves (the maximum $\hat{z}$ and $-\hat{z}$ excursions), with each point on the curves corresponding to an individual orbit. From these simplified representations, the shapes of several families can easily be compared. Such a comparison appears in Figure 3.12. A set of L_1 halo families is represented for a range of sail lightness parameter values. The orbits are plotted relative to a libration point-centered coordinate frame such that all of the libration points coincide, thus, emphasizing the change in family shape rather than family location. Each family appears as two curves, one positive (intersections with the $\hat{x}-\hat{z}$ plane at maximum z), and one negative (the minimum z intersection point along the orbit). Of particular interest is the evolution of the family such that it appears to "fold through" itself at maximum z, as β increases; the family transitions from the "bowl" shape of the classical halo family to a form that originates and terminates at the $\hat{x} - \hat{y}$ plane. A similar representation of the evolution of the L_2 family appears in Figure 3.13. Again, the shape of the L_2 family is essentially preserved as the sail lightness is increased.

3.3.2 Stability

Given the changes in the properties of the halo families under the influence of a solar sail force, it is also possible that the stability of the orbits has been altered.

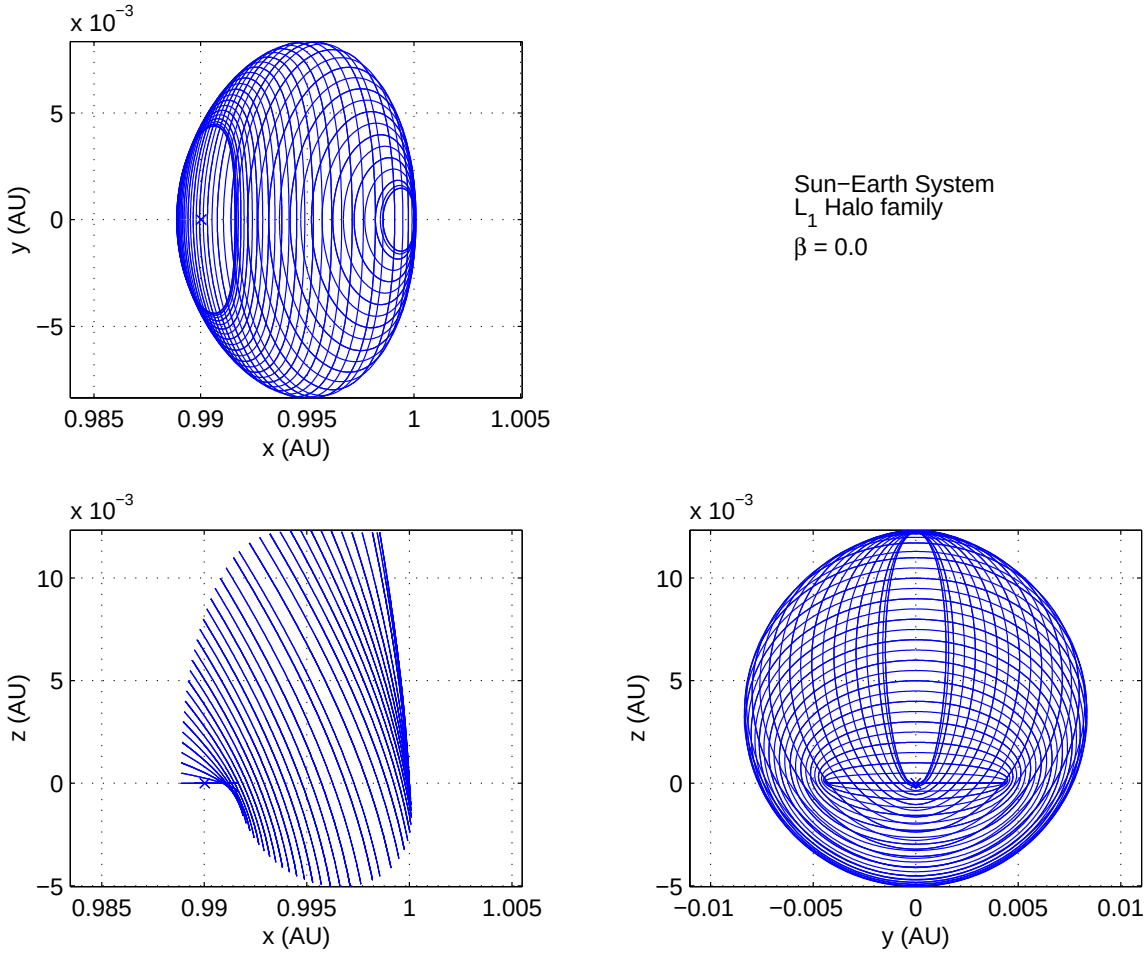

Figure 3.7. Classical Sun-Earth L_1 halo family

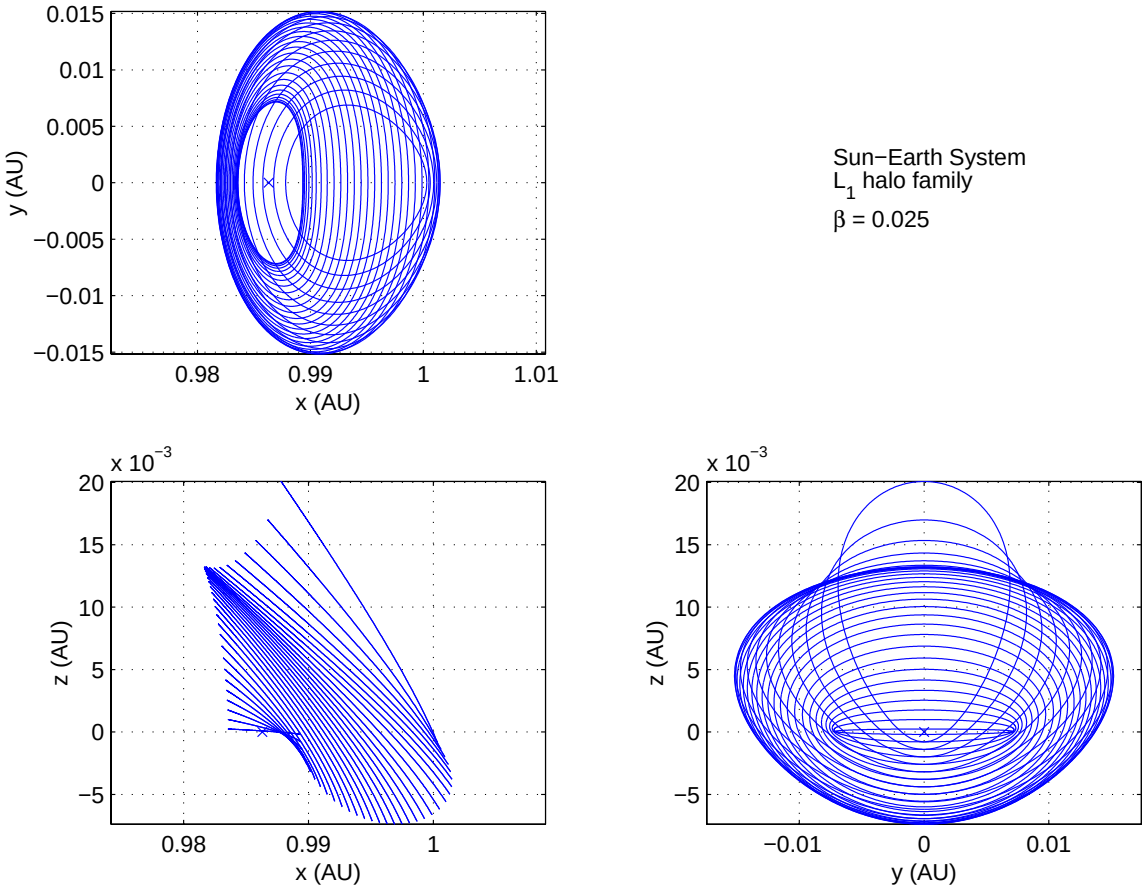

Figure 3.8. Sun-Earth L_1 halo family for β=0.025

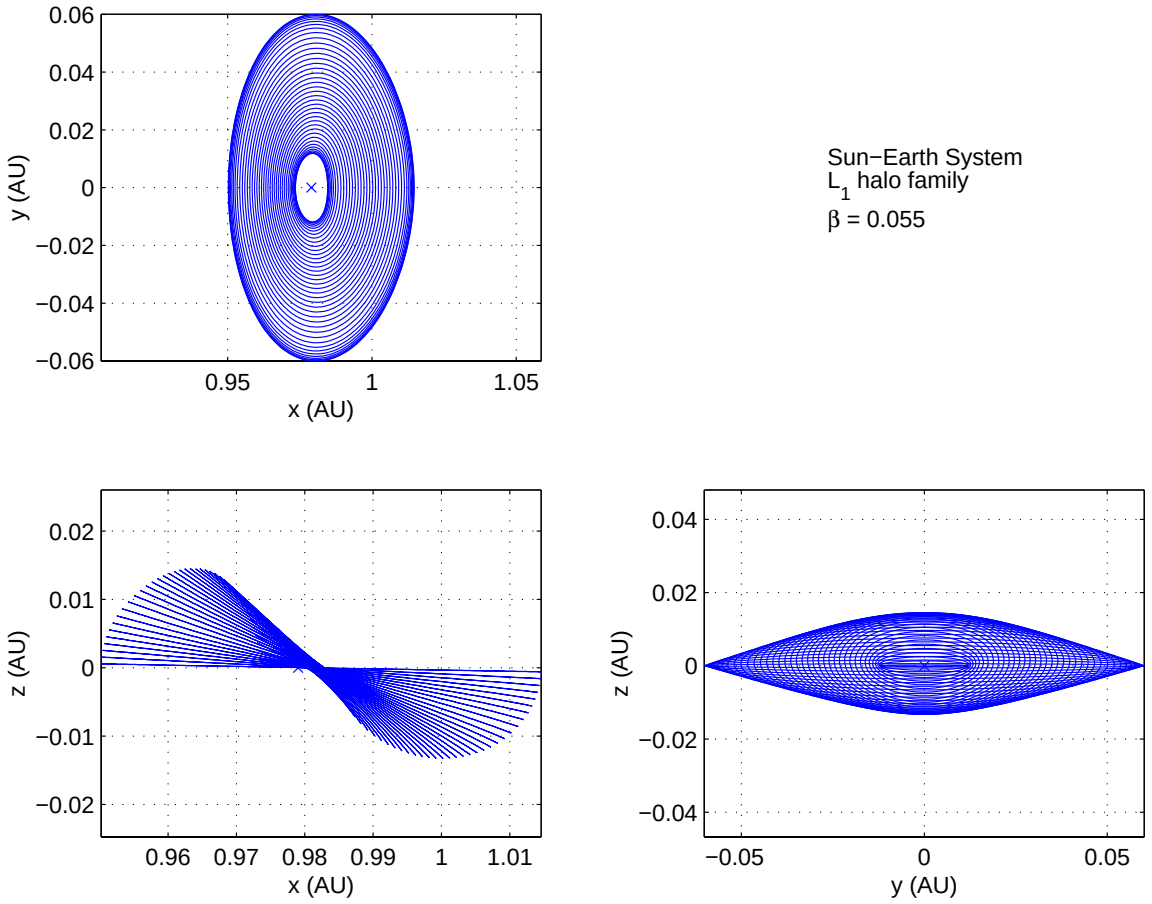

Figure 3.9. Sun-Earth L_1 halo family for β=0.055

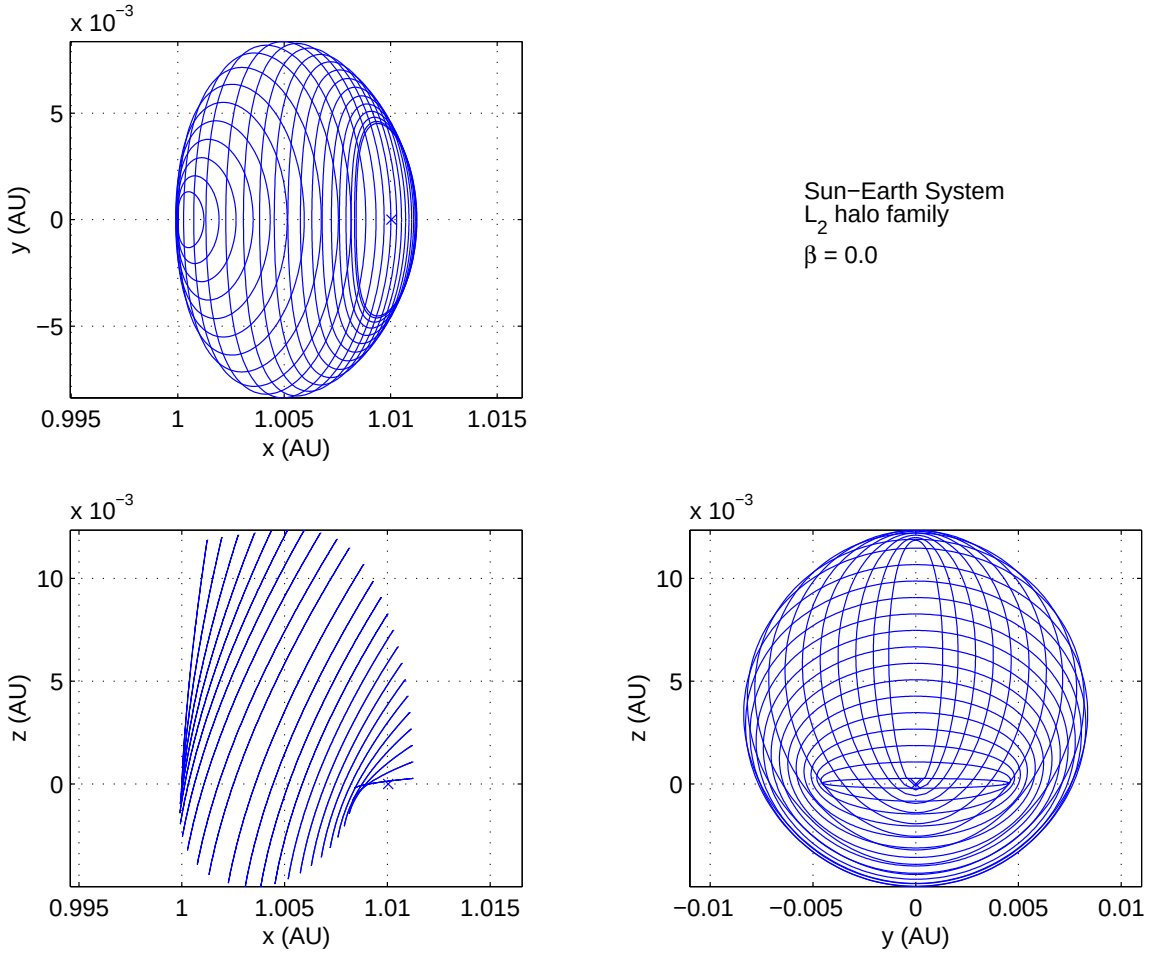

Figure 3.10. Classical Sun-Earth L_2 halo family

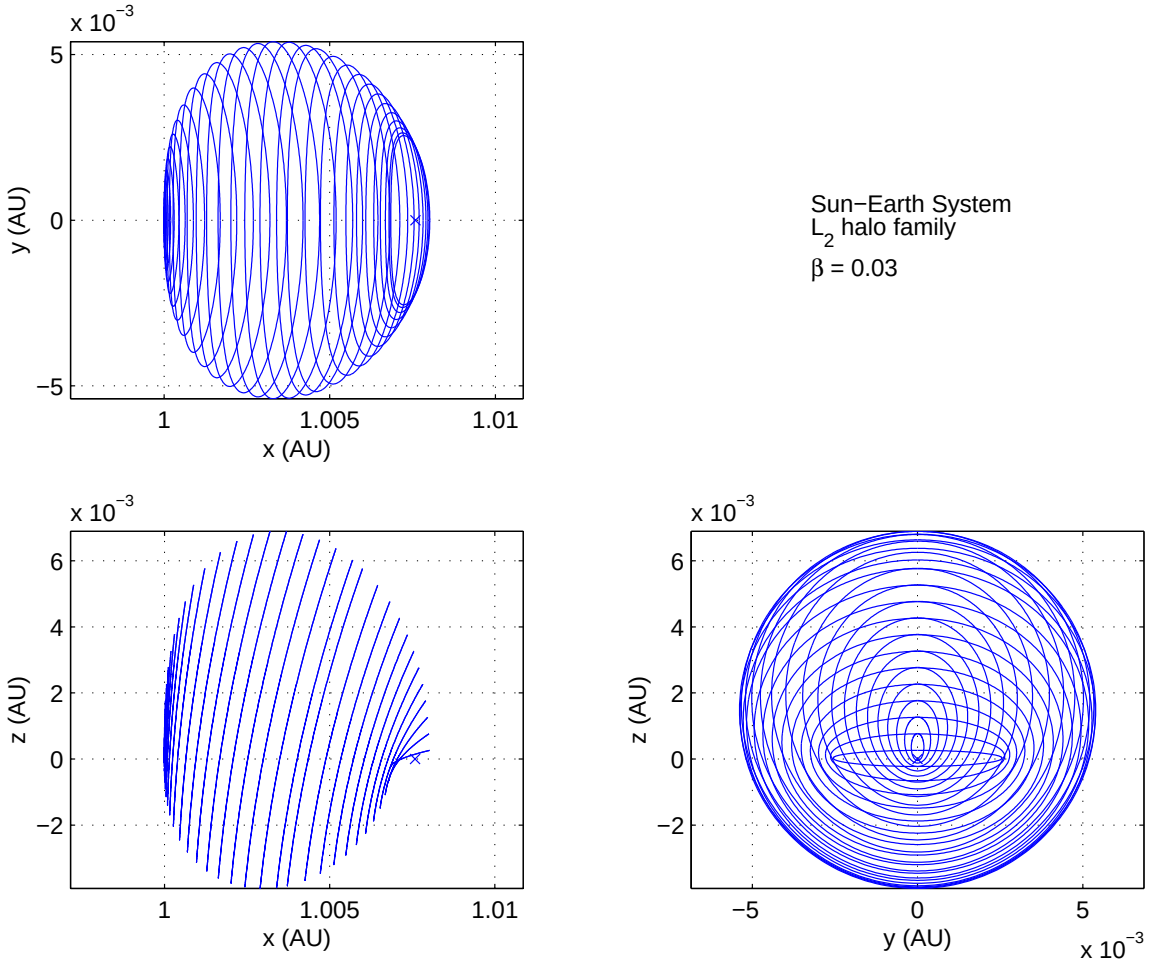

Figure 3.11. Sun-Earth L_2 halo family for β=0.03

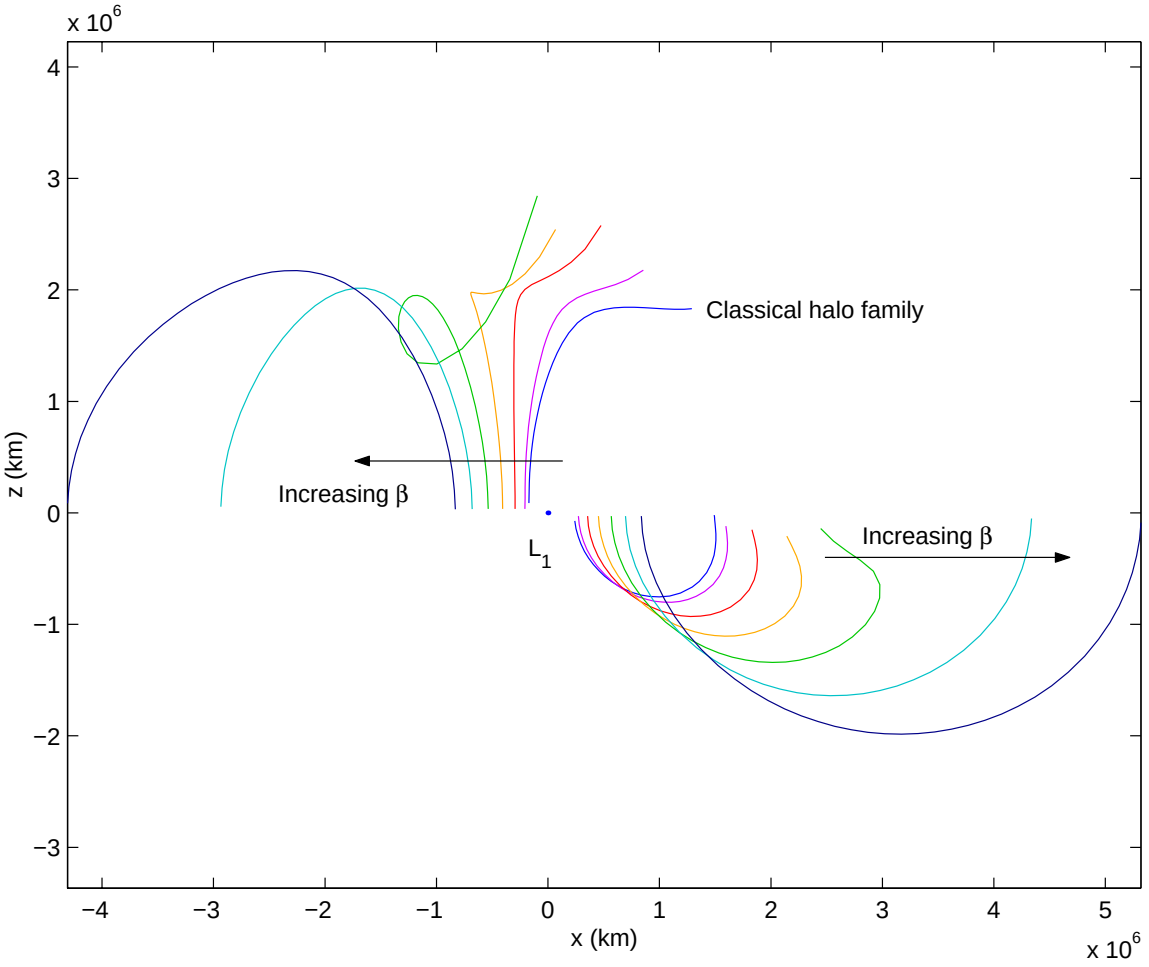

Figure 3.12. Evolution of the Sun-Earth L_1 halo family: $\beta = 0.0$-0.055

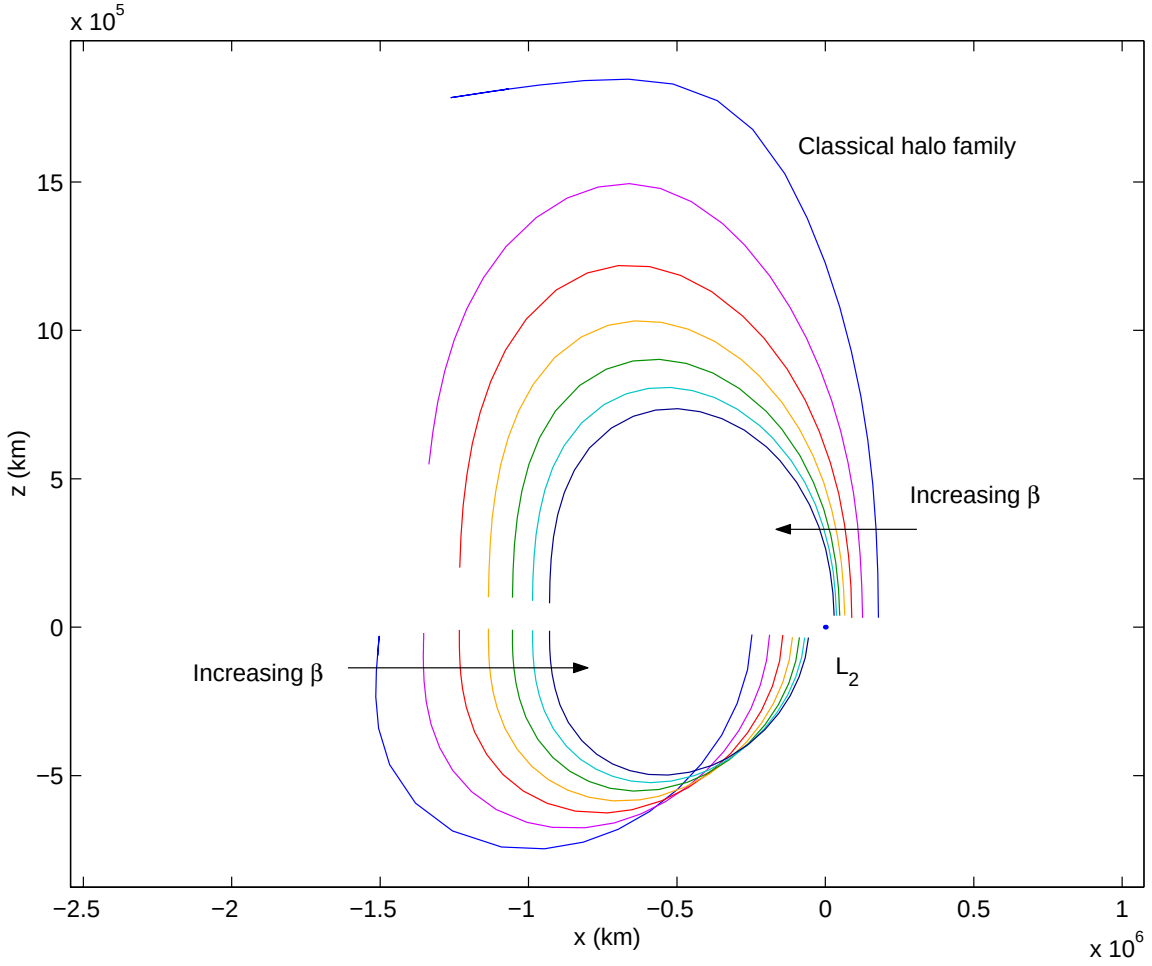

Figure 3.13. Evolution of the Sun-Earth L_2 halo family: $\beta = 0.0$-0.06

Orbital stability is of interest for several reasons. The stability characteristics of a given orbit may influence the use of such an orbit for mission applications, and will impact the cost of stationkeeping maneuvers. Changes in the stability from one section of a family to another also indicate bifurcation points, or intersections with other families of periodic orbits [43]; these other families expand knowledge of the solution space.

From Floquet theory [39], it is well known that the stability of a periodic orbit can be determined by examining the eigenvalues, λ_i, of the monodromy matrix, defined as the state transition matrix after one period of the motion. The stability criteria are:

1. $|\lambda_i| < 1$ indicates stability.

2. $|\lambda_i| > 1$ indicates instability.

3. $|\lambda_i| = 1$ provides no stability information concerning the nonlinear system.

A general periodic orbit must possess at least one eigenvalue such that $\lambda \equiv 1$ [39]. The six eigenvalues associated with a classical periodic halo orbit also appear in reciprocal, complex conjugate pairs [21]. As a result of the reciprocal pair condition, the monodromy matrix corresponding to a periodic halo orbit possesses two eigenvalues equal to 1. Thus, the remaining four eigenvalues characterize the stability of the orbit. Of course, if one of the four eigenvalues is inside the unit circle, its reciprocal lies outside the circle. Thus, the most stable configuration occurs with all six eigenvalues on the unit circle. The "order of instability" is defined as the number of eigenvalues that are evaluated with magnitude $|\lambda| > 1$.

The evolution of the stability along the L_1 and L_2 families appears in Figures 3.14 and 3.15. Comparing Figure 3.14 with Figure 3.12, it is apparent that along some regions of the L_1 families the stability information has not been recorded. These regions indicate orbits for which the monodromy matrix was found to have *no* eigenvalues equal to one, at least to the numerical accuracy available. If the numerical result is indeed correct, this implies that the orbits in question are not periodic. Nevertheless,

these orbits fit appropriately within the family, meet the periodicity conditions for perpendicular plane crossings to within the same tolerance as all other orbits in the family, and can be integrated for multiple revolutions without significant divergence. Therefore, the monodromy matrix, and any stability information derived from it, is considered suspect for these orbits, and is not recorded.

To further examine the problem, monodromy matrices for the suspect orbits are also computed using an alternative method. For this second approach, recall that the state transition matrix satisfies the equation,

$$\delta\overline{x}(t) = \mathbf{\Phi}(t, t_0)\delta\overline{x}(t_0) \ . \tag{3.59}$$

Thus, if $\mathbf{\Phi}(t, t_0)$ is partitioned into six-dimensional columns such that

$$\mathbf{\Phi}(t, t_0) \ = \ [\overline{\phi}_0 \vdots \overline{\phi}_1 \vdots \overline{\phi}_2 \vdots \overline{\phi}_3 \vdots \overline{\phi}_4 \vdots \overline{\phi}_5] \ ,$$

and $\delta\overline{x}(t_0)$ is assumed to be defined in the following form

$$\delta\overline{x}_\epsilon(t_0) = [\epsilon \quad 0 \quad 0 \quad 0 \quad 0 \quad 0]^T \ ,$$

then

$$\delta\overline{x}_0(t) = \mathbf{\Phi}(t, t_0)\delta\overline{x}_\epsilon(t_0) = \epsilon\overline{\phi}_0 \ . \tag{3.60}$$

Of course, equation (3.60) can be rearranged to solve for a column of the state transition matrix as,

$$\overline{\phi}_0 = \frac{1}{\epsilon}\delta\overline{x}_0(t) \ . \tag{3.61}$$

Similarly, a modification of the initial condition,

$$\delta\overline{x}_\epsilon(t_0) = [0 \quad \epsilon \quad 0 \quad 0 \quad 0 \quad 0]^T \ ,$$

yields

$$\overline{\phi}_1 = \frac{1}{\epsilon}\delta\overline{x}_1(t) \ , \tag{3.62}$$

and so on. Therefore, a state transition matrix can be numerically computed one column at a time by adding a perturbation ϵ to a single component of the initial state

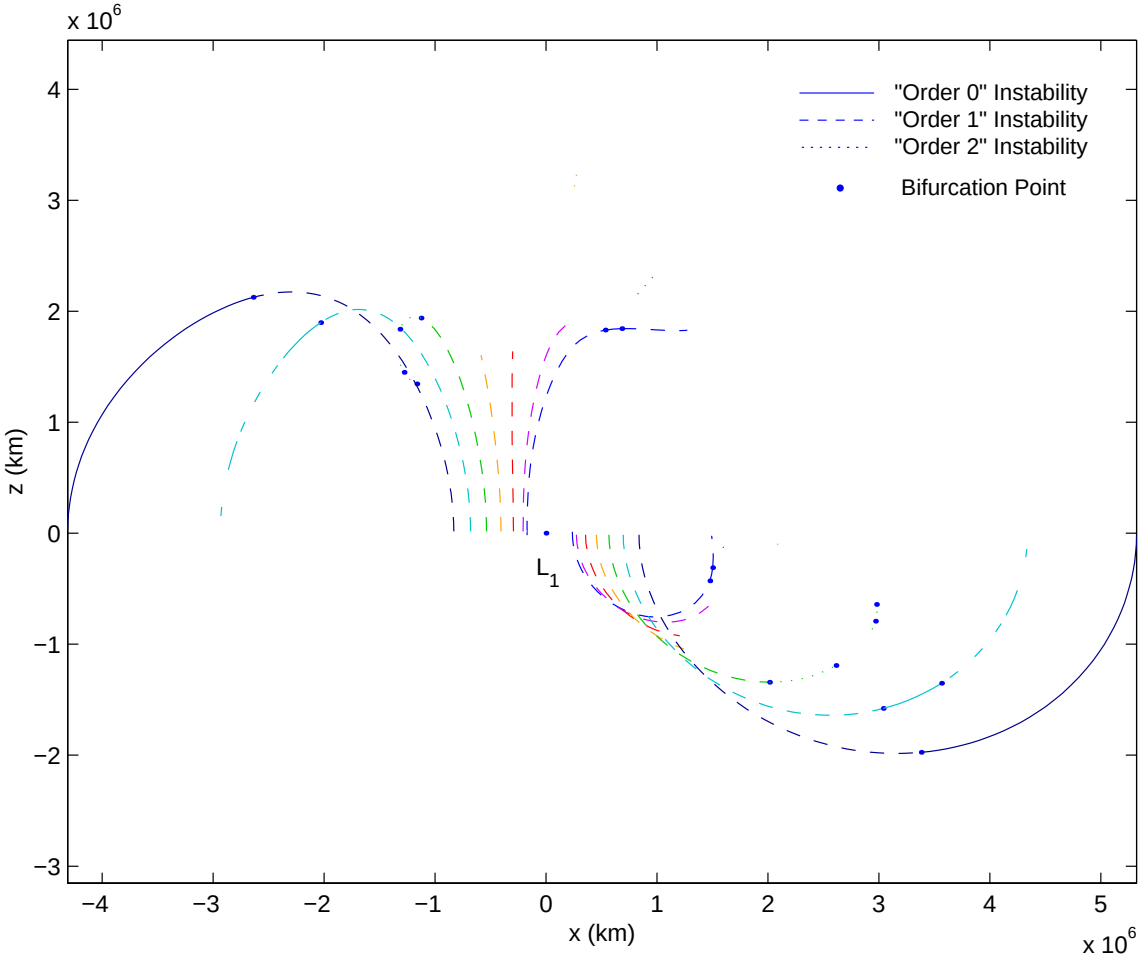

Figure 3.14. Evolution of the stability characteristic of the Sun-Earth L_1 halo family: $\beta = 0.0$-0.055

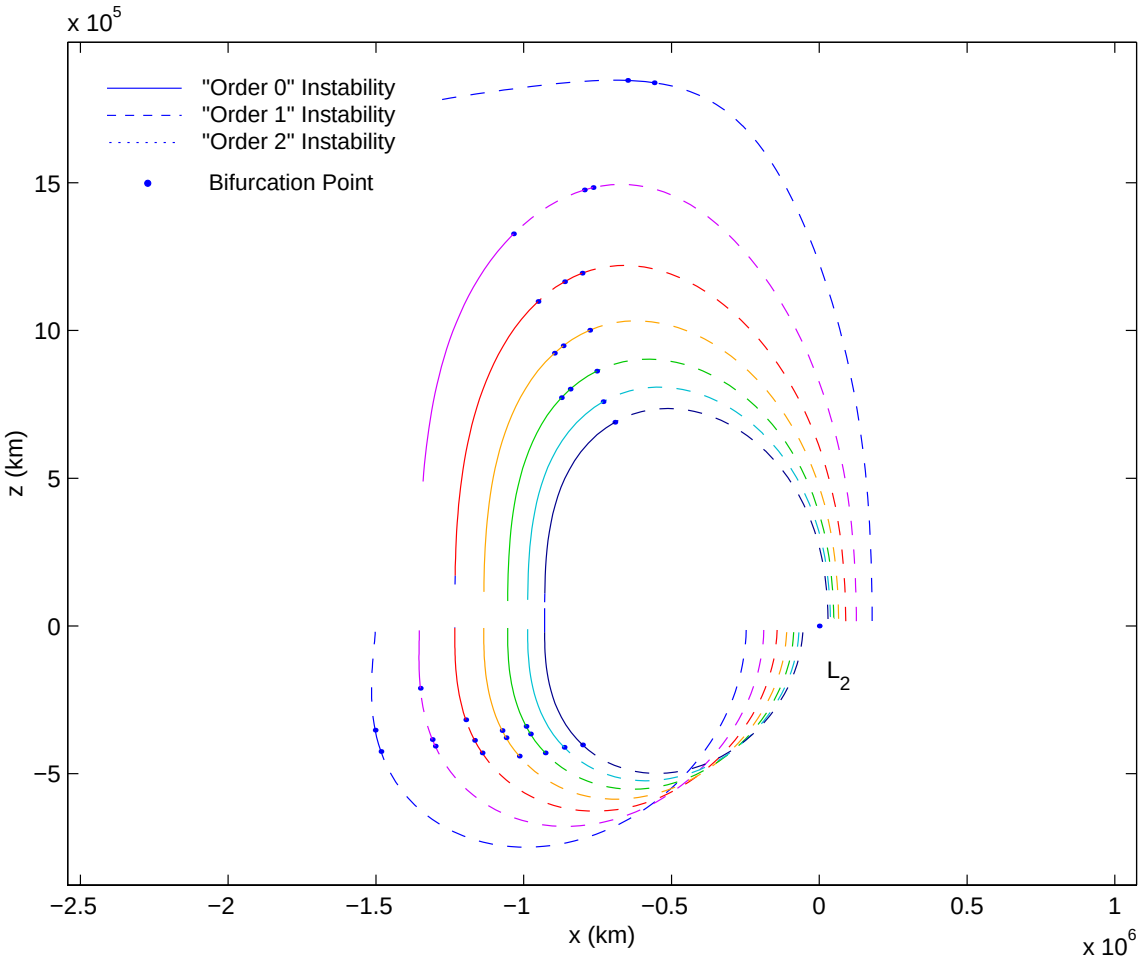

Figure 3.15. Evolution of the stability characteristic of the Sun-Earth L_2 halo family: $\beta = 0.0$-0.06

corresponding to the reference trajectory, then numerically integrating the modified initial state, subtracting the reference final state from the integrated result, and finally dividing by ϵ. The resulting state transition matrix that is somewhat dependent on the values selected for the perturbation (ϵ). It is possible to determine values for the perturbations ϵ such that the monodromy matrices computed using this second method approximately match the suspect monodromy matrices. Further, through trial and error, it is possible to determine values of ϵ that generate monodromy matrices with the required eigenvalue equal to one, for some orbits.

The source of the difficulties with the computation of the monodromy matrix is still unresolved. These problems are not encountered in the computation of the orbits in the L_2 families. A future investigation into the numerical issues associated with computing the monodromy matrix in this regime is clearly warranted.

3.4 Stationkeeping about Nominal Family Members

3.4.1 Proposed Strategy

In practice, unmodelled perturbations and orbit injection errors will result in drift of a spacecraft from a nominal trajectory. This effect is further amplified by the unstable nature of libration point orbits. Thus, a stationkeeping algorithm is required to compute corrective maneuvers such that the actual spacecraft trajectory remains acceptably close to the nominal path. Stationkeeping strategies for libration point orbits have typically involved computing discrete, impulsive velocity corrections to be applied with thrusters [23, 25, 44]. However, the introduction of a solar sail introduces the possibility of using changes in the sail orientation (and potentially the sail area) to generate various "thrust" magnitudes and directions, and, thus, to provide stationkeeping capabilities.

The stationkeeping strategy developed here is an adaptation of the libration point trajectory stationkeeping method originally introduced by Howell and Pernicka [23], modified such that the stationkeeping maneuvers are computed in terms of sail orientation angles rather than velocity changes. Hence, the resulting stationkeeping maneuvers are discrete changes in the sail orientation angles, which might occur as

infrequently as twice per revolution. Between maneuvers, the sail angles remain constant, and, thus, the sail orientation is fixed relative to the direction of solar radiation (although it is changing relative to an inertial frame). To adapt the libration point stationkeeping model, the linear variational equations for motion near a reference trajectory are extended to include terms for the variations in sail orientation. The variables that represent changes in the sail orientation are defined such that

$$\delta\alpha = \alpha - \alpha_0 \ , \quad \text{and} \quad \delta\gamma = \gamma - \gamma_0 \ ,$$

where α_0 and γ_0 are the nominal sail angles along the reference trajectory. For this investigation α_0 and γ_0 are constants. This suggests that the halo orbits from families such as those in Figures 3.5, 3.8, 3.9, and 3.11 might well serve as reference trajectories. The variational equations can then be written as

$$\begin{aligned} \delta\ddot{x} - 2\delta\dot{y} &= U_{xx}\delta x + U_{xy}\delta y + U_{xz}\delta z + a_{x\alpha}\delta\alpha + a_{x\gamma}\delta\gamma \ , & (3.63) \\ \delta\ddot{y} + 2\delta\dot{x} &= U_{yx}\delta x + U_{yy}\delta y + U_{yz}\delta z + a_{y\alpha}\delta\alpha + a_{y\gamma}\delta\gamma \ , & (3.64) \\ \delta\ddot{z} &= U_{zx}\delta x + U_{zy}\delta y + U_{zz}\delta z + a_{z\alpha}\delta\alpha + a_{z\gamma}\delta\gamma \ , & (3.65) \end{aligned}$$

where $a_{jk} = \frac{\partial a_j}{\partial k}$, that is, the partial derivatives of the sail acceleration along the reference trajectory, relative to the sail orientation angles (see Appendix E).

To facilitate expression of the linearized system in state space form, the variations in the orientation variables are incorporated into an augmented variational state vector, defined as follows,

$$\delta\overline{x} \equiv [\delta x \ \ \delta y \ \ \delta z \ \ \delta\dot{x} \ \ \delta\dot{y} \ \ \delta\dot{z} \ \ \delta\alpha \ \ \delta\gamma]^T \ .$$

It is assumed that the sail orientation angles remain constant along the trajectory arc of interest. Such an arc may be anywhere from 1 day to 1 revolution in length. Thus, the state space form of the modified variational equations can be written as

$$\delta\dot{\overline{x}}(t) = \mathbf{A}(t)\delta\overline{x}(t) \ , \qquad (3.66)$$

where the 8×8 matrix $\mathbf{A}(t)$ has the general form

$$\mathbf{A}(t) \equiv \begin{bmatrix} \mathbf{0} & \mathbf{I}_3 & \mathbf{0} \\ \mathbf{B}(t) & \mathbf{C} & \mathbf{D}(t) \\ \mathbf{0} & \mathbf{0} & \mathbf{0} \end{bmatrix} ,$$

and the time-varying submatrix $\mathbf{D}(t)$ is 3×2 with the form

$$\mathbf{D}(t) \equiv \begin{bmatrix} a_{x\alpha} & a_{x\gamma} \\ a_{y\alpha} & a_{y\gamma} \\ a_{z\alpha} & a_{z\gamma} \end{bmatrix} .$$

The solution to the system in equation (3.66) has the form

$$\delta\overline{x}(t_p) = \mathbf{\Phi}(t_p, t_q)\delta\overline{x}(t_q) , \tag{3.67}$$

where $\mathbf{\Phi}(t_p, t_q)$ is the state transition matrix.

With the addition of the variations in the orientation angles, the state transition matrix, $\mathbf{\Phi}(t_p, t_q)$, enlarges to become an 8×8 matrix. This matrix is partitioned such that

$$\mathbf{\Phi}(t_p, t_q) = \begin{bmatrix} \mathbf{K}_{pq} & \mathbf{L}_{pq} & \mathbf{E}_{pq} \\ \mathbf{M}_{pq} & \mathbf{N}_{pq} & \mathbf{F}_{pq} \\ \mathbf{0} & \mathbf{0} & \mathbf{I}_2 \end{bmatrix} , \tag{3.68}$$

where the partitions represent the following vector partial derivatives,

$$\begin{aligned} \mathbf{K}_{pq} &= \tfrac{\partial \overline{r}_{t_p}}{\partial \overline{r}_{t_q}} , \\ \mathbf{L}_{pq} &= \tfrac{\partial \overline{r}_{t_p}}{\partial \overline{v}_{t_q}} , \\ \mathbf{M}_{pq} &= \tfrac{\partial \overline{v}_{t_p}}{\partial \overline{r}_{t_q}} , \\ \mathbf{N}_{pq} &= \tfrac{\partial \overline{v}_{t_p}}{\partial \overline{v}_{t_q}} , \\ \mathbf{E}_{pq} &= \tfrac{\partial \overline{r}_{t_p}}{\partial \overline{\theta}} , \\ \mathbf{F}_{pq} &= \tfrac{\partial \overline{v}_{t_p}}{\partial \overline{\theta}} . \end{aligned}$$

The vectors in these expressions are defined as follows,

$$\begin{aligned} \overline{r} &= [x \quad y \quad z]^T , \\ \overline{v} &= [\dot{x} \quad \dot{y} \quad \dot{z}]^T , \\ \overline{\theta} &= [\alpha \quad \gamma]^T . \end{aligned}$$

The partitions $\mathbf{K}_{pq}$, $\mathbf{L}_{pq}$, $\mathbf{M}_{pq}$, and $\mathbf{N}_{pq}$ are 3×3 matrices that together comprise the equivalent of the standard state transition matrix. The partitions $\mathbf{E}_{pq}$ and $\mathbf{F}_{pq}$ are 3×2 matrices associated with the effect of the sail orientation on the position and velocity of the spacecraft.

Development of the stationkeeping algorithm originates with a cost function. Let $\overline{m}_i$ be a 3-element vector representing the deviation of the actual trajectory from the nominal at some time t_i, that is, $\overline{m}_i = [\delta x(t_i) \quad \delta y(t_i) \quad \delta z(t_i)]^T$. This deviation is caused by a velocity perturbation, represented by a 3-dimensional velocity error vector $\overline{e}_0 = [\delta \dot{x}(t_0) \quad \delta \dot{y}(t_0) \quad \delta \dot{z}(t_0)]^T$, and a position perturbation written in terms of a 3-element vector $\overline{p}_0 = [\delta x(t_0) \quad \delta y(t_0) \quad \delta z(t_0)]^T$, both evaluated at time t_0. The deviation is also influenced by a corrective sail orientation $\delta\overline{\theta}_c = [\delta\alpha_c \quad \delta\gamma_c]^T$ applied at some time t. For the purposes of this investigation, assume that the correction is applied at $t = t_0$. The index i denotes a target point, that is, some point downstream at a future time $t_i = t_0 + \Delta t_i$ when the predicted actual trajectory will be compared to the nominal. (See Figure 3.16.) The methodology can employ any number of target points, but for this study, as in [23], two target points are arbitrarily selected. Given the submatrices that comprise the state transition matrix associated with the nominal trajectory, the linear approximation for the position deviation at target point i can be expressed as,

$$\overline{m}_i \;\cong\; \mathbf{K}_{i0}\overline{p}_0 \;+\; \mathbf{L}_{i0}\overline{e}_0 \;+\; \mathbf{E}_{i0}\delta\overline{\theta}_c \;. \tag{3.69}$$

The cost function is then defined such that

$$J[\overline{p}_0, \overline{e}_0, \delta\overline{\theta}_c] \;=\; \delta\overline{\theta}_c^T\mathbf{Q}\delta\overline{\theta}_c \;+\; \overline{m}_1^T\mathbf{R}\overline{m}_1 \;+\; \overline{m}_2^T\mathbf{S}\overline{m}_2 \;, \tag{3.70}$$

where the superscript T signifies a transpose. The weighting matrix $\mathbf{Q}$ is symmetric and positive definite, while $\mathbf{R}$ and $\mathbf{S}$ are positive semidefinite. Note that the weighting matrices can be time-varying, but are assumed constant in this initial investigation.

Given the cost function, J, the optimal corrective sail orientation is obtained by minimizing equation (3.70), that is, determination of the optimal sail variations,

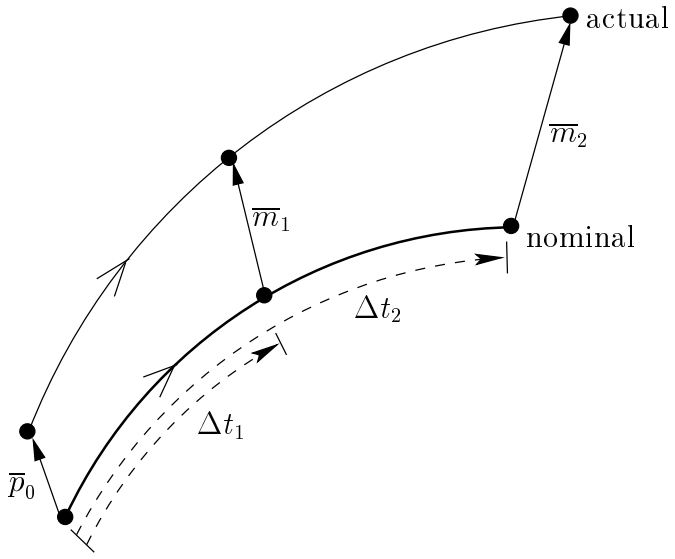

Figure 3.16. Relationship of the target points to the nominal and actual trajectories

$\delta\overline{\theta}_c = \delta\overline{\theta}_c^*$, such that

$$\frac{\partial J}{\partial \delta\overline{\theta}_c} = 0 \ .$$

Using the expression in equation (3.69), the terms in equation (3.70) can be expanded. Then, the partial derivative of J with respect to $\delta\overline{\theta}_c$, yields

$$\begin{aligned} \frac{\partial J}{\partial \delta\overline{\theta}_c} \ &= \ 2\mathbf{Q}\delta\overline{\theta}_c \ + \ 2\mathbf{E}_{10}^T\mathbf{R}\mathbf{L}_{10}\overline{e}_0 \ + \ 2\mathbf{E}_{10}^T\mathbf{R}\mathbf{K}_{10}\overline{p}_0 \ + \ 2\mathbf{E}_{10}^T\mathbf{R}\mathbf{E}_{10}\delta\overline{\theta}_c \\ &\quad + 2\mathbf{E}_{20}^T\mathbf{S}\mathbf{L}_{20}\overline{e}_0 \ + \ 2\mathbf{E}_{20}^T\mathbf{S}\mathbf{K}_{20}\overline{p}_0 \ + \ 2\mathbf{E}_{20}^T\mathbf{S}\mathbf{E}_{20}\delta\overline{\theta}_c \ , \end{aligned} \tag{3.71}$$

and, thus, the optimal corrective sail orientation is evaluated as follows,

$$\begin{aligned} \delta\overline{\theta}_c^* \ &= \ -\left[\mathbf{Q} \ + \ \mathbf{E}_{10}^T\mathbf{R}\mathbf{E}_{10} \ + \ \mathbf{E}_{20}^T\mathbf{S}\mathbf{E}_{20}\right]^{-1} \\ &\quad \times \left[(\mathbf{E}_{10}^T\mathbf{R}\mathbf{L}_{10} + \mathbf{E}_{20}^T\mathbf{S}\mathbf{L}_{20})\overline{e}_0 \ + \ (\mathbf{E}_{10}^T\mathbf{R}\mathbf{K}_{10} + \mathbf{E}_{20}^T\mathbf{S}\mathbf{K}_{20})\overline{p}_0\right] \ . \end{aligned} \tag{3.72}$$

The solution of this equation requires the inversion of just a 2×2 matrix. Note that the sail is assumed to reorient instantaneously.

3.4.2 Preliminary Results

The evaluation of a stationkeeping strategy is accomplished by introducing various errors into a nominal trajectory, and examining the actual trajectory that results

when stationkeeping maneuvers are applied. For this investigation, the focus is restricted to consideration of the impact of injection, tracking, and orientation control errors. Note that modeling inaccuracies are not considered. For the simulations, a zero-mean, Gaussian random number generator is used to compute values representing the error in each component. Injection errors are modelled as deviations from the nominal initial conditions, and tracking errors as a random alteration of the integrated "actual" trajectory data passed to the stationkeeping algorithm. The orientation control errors represent a lack of precision in the attitude control systems, i.e., execution errors modelled as random deviations from the desired sail orientation. These random deviations are added to the desired sail orientation at each time step, to generate the sail orientation actually used for that step of the numerical integration.

Given a nominal solution, the initial conditions are randomly modified to simulate the injection error, and then both the nominal and "actual" trajectories are integrated simultaneously. At various times along the trajectory, the stationkeeping algorithm will determine that a maneuver, or sail reorientation, is required. Three criteria determine the timing of the maneuver/reorientation:

1. Input parameter t_{min}, which defines the minimum time between maneuvers. (Although t_{min} values up to half a revolution are tested here, this variable can be used to mimic a sail that nearly continuously changes orientation.)

2. Input parameter d_{min}, which specifies the allowable deviation from the nominal before a maneuver is implemented. (This allows some evaluation of a "tight" versus a "loose" control approach.)

3. The deviation must be increasing, i.e., the spacecraft is drifting further from the nominal. (Corrections are only necessary if the unstable mode has been excited.)

If all three of the conditions are met, the optimal maneuver is computed, and, subject to random error, implemented.

For all of the samples, the simulation interval is the equivalent of four revolutions along the nominal, terminating early if the deviation from the nominal exceeds an arbitrary limit (in this case 50,000 km). Since the nominal trajectories examined here are on-axis halo orbits, the baseline cone angle is, of course, $\alpha = 0^\circ$ throughout the orbit. Although the clock angle is nominally completely free, experience demonstrates that better results are achieved with γ near either 90° or 270°. For this study, the clock angle is arbitrarily fixed such that $\gamma = 85^\circ$.

The standard deviations for the orbit injection and tracking errors are relatively large, but consistent with the stationkeeping investigation by Howell and Pernicka [23]:

$$\begin{aligned} \sigma_x &= 1.5\text{km}\,, \quad & \sigma_y &= 2.5\text{km}\,, \quad & \sigma_z &= 15.0\text{km}\,, \\ \sigma_{\dot{x}} &= 1.0\text{mm/s}\,, & \sigma_{\dot{y}} &= 1.0\text{mm/s}\,, & \sigma_{\dot{z}} &= 3.0\text{mm/s}\,. \end{aligned}$$

Various estimates for the standard deviation of the orientation control errors are obtained from the spacecraft pointing accuracies discussed in [45] and [46]. Since no data on orientation control accuracy for an actual solar sail mission exists, these estimates are based on the performance of the attitude determination and control systems used in current spacecraft. The two values used in this study are

$$\sigma_\theta = 0.01^\circ, \text{ and } \sigma_\theta = 0.001^\circ\,,$$

that represent errors in the actual orientation relative to the desired nominal orientation. Simulations using both estimates are structured to investigate the sensitivity of the stationkeeping strategy to errors in the sail orientation control systems.

A baseline L_1 halo orbit with out-of-plane amplitude $A_z = 200,000$km is used for evaluation of the stationkeeping strategy. Two different values of sail lightness are incorporated, one in the feasible range of current solar sail designs ($\beta = 0.055$), and the other representing an extremely low performance sail ($\beta = 0.005$). This results in two different nominal periodic orbits, one for each value of the sail lightness parameter. (See Figures 3.17 and 3.18.) For each nominal, several different values of t_{min}, Δt_1, and Δt_2 are examined, although d_{min} is fixed to zero throughout the investigation.

Elements of the weighting matrices (based on trial and error) are defined with the values

$$\begin{aligned} Q &= \text{diag}[1 \times 10^{-5},\ \ 1 \times 10^{-5},\ \ 1 \times 10^{-5}]\,, \\ R &= \text{diag}[1,\ \ 1,\ \ 1]\,, \\ S &= \text{diag}[5,\ \ 5,\ \ 5]\,. \end{aligned}$$

The values of these weighting matrices correspond to sail orientation angles expressed in radians, and position deviations expressed in the nondimensional distance units defined previously (equivalent to astronomical units in the Sun-Earth system). In each case, consistent with Howell and Pernicka's study [23], 100 separate trials are simulated, each corresponding to a different randomly generated orbit injection error. (A simple analysis indicates that 100 trials is a sufficient number to provide at least "order of magnitude" performance estimates.) The statistics compiled for each case are presented in Tables 3.1 and 3.2. The stationkeeping algorithm is capable of maintaining a vehicle reasonably close to the nominal path for both values of the sail lightness parameter. It is notable that the clock angle, γ, does not appear to play a role in the stationkeeping process, although this is not surprising for the on-axis orbits. Not unexpectedly, increasing the minimum time between maneuvers reduces the performance. An increase in the magnitude of the orientation control errors also has a negative effect, although controlling the vehicle to remain quite near the reference orbit is still possible for smaller values of t_{min}. The overall performance of the two sails is not directly comparable. The solar sail with a higher sail lightness ($\beta = 0.055$) results in a reference orbit with a period that is significantly longer than the reference periodic orbit corresponding to the sail defined with $\beta = 0.005$. Thus, four revolutions along the first nominal halo results in a total flight time that is almost twice the length of that for the low performance sail.

A similar analysis is also available for L_2 orbits. A baseline L_2 halo orbit generates a reference orbit for a sail lightness value of $\beta = 0.01$. (See Figure 3.19.) Out-of-plane amplitude is again $A_z = 200,000$ km. The elements of the weighting matrices $\mathbf{Q}$, $\mathbf{R}$, and $\mathbf{S}$ are the same as those previously specified for the L_1 cases, and the

orientation control error $\sigma_\theta = 0.01^\circ$ is again used. A sample set of 100 trials produced results similar to L_1 applications, as demonstrated in Table 3.3. The stationkeeping strategy is reasonably successful for L_2 orbits, even without "fine-tuning" of the various parameters. A more in-depth study of stationkeeping in the vicinity of L_1 and L_2 is indicated.

These preliminary results appear quite promising. More work on developing and tuning the strategy outlined here is clearly desirable. The effect of additional target points is not known, and this should be investigated with the objective of further reducing the magnitude of the deviations from the nominal trajectory. The weighting matrices can be further investigated for specific trajectories, and perhaps using time varying weights, if necessary. In addition to minimizing the position deviation, the strategies that seek to minimize the velocity deviations at the target points, such as the Δv strategies introduced in [25], may also prove advantageous. Another possibility is to exploit the solar sail strategy developed here for minor deviations, in combination with the original impulsive maneuver strategy from [23] to provide larger corrections if the deviation becomes excessive. In terms of applications, it is likely that an easily-manufactured low performance solar sail, perhaps corresponding to $\beta = 0.005$, could be used to generate and maintain halo orbits very near the classical L_1 family, providing a no-propellant, long-term stationkeeping technique for traditional libration point missions.

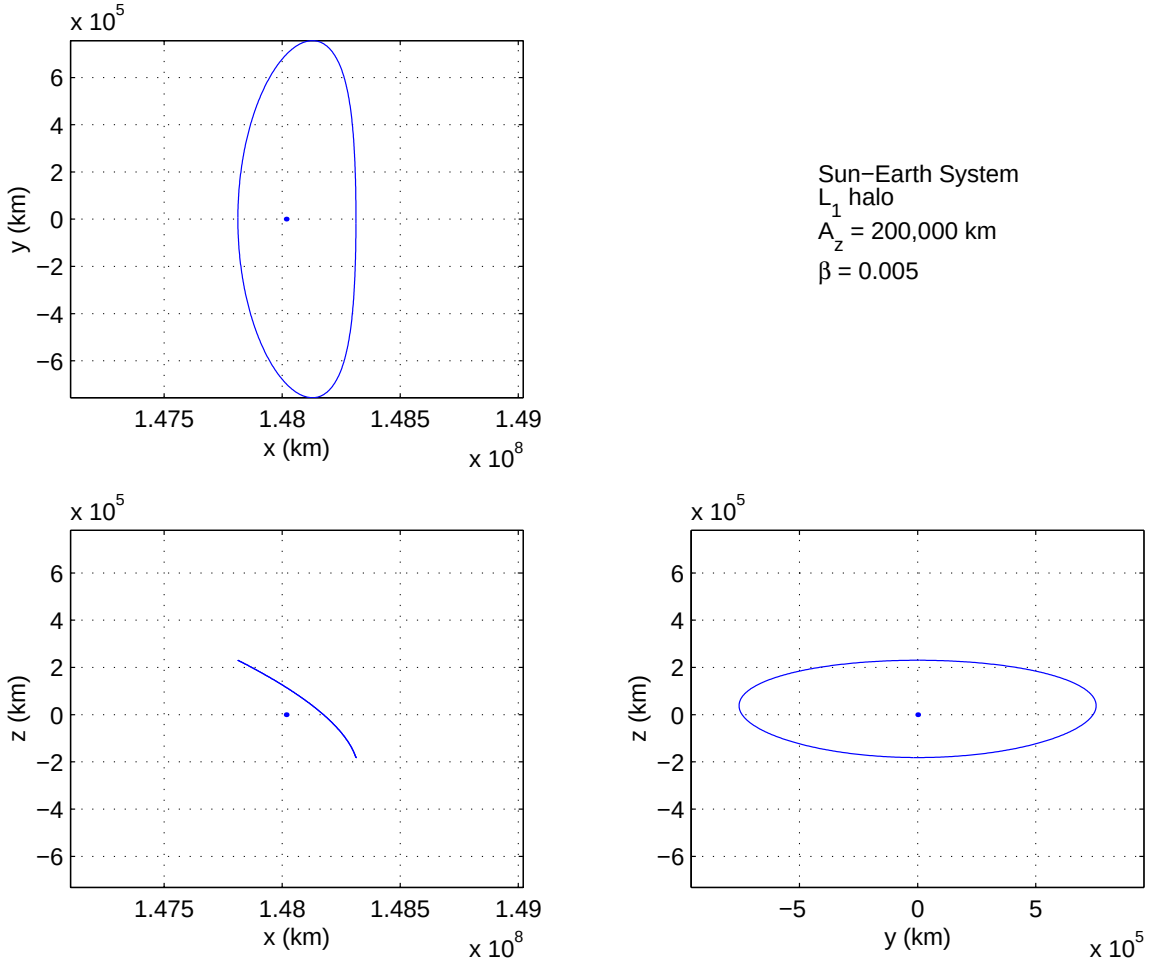

Figure 3.17. Nominal Sun-Earth L_1 halo orbit for $\beta = 0.005$

Table 3.1. Stationkeeping results for reference periodic L_1 halo orbit incorporating $\beta = 0.005$ (nominal period: 190 days)

$\sigma_\theta = 0.001°$			
	t_{min} = 30 days	t_{min} = 60 days	t_{min} = 80 days
Δt_1 (days)	70	90	130
Δt_2 (days)	110	130	180
Avg. completed revs	4.0	3.99	3.98
Avg. max. deviation (km)	1,390	2,960	8,370
Avg. $\delta\alpha$ (degrees)	0.0083	0.0075	0.0108
Avg. $\delta\gamma$ (degrees)	0.0	0.0	0.0

$\sigma_\theta = 0.01°$			
	t_{min} = 30 days	t_{min} = 60 days	t_{min} = 80 days
Δt_1 (days)	70	90	130
Δt_2 (days)	110	130	180
Avg. completed revs	4.0	3.95	3.61
Avg. max. deviation (km)	1,860	9,740	23,660
Avg. $\delta\alpha$ (degrees)	0.0125	0.0226	0.0507
Avg. $\delta\gamma$ (degrees)	0.0	0.0	0.0

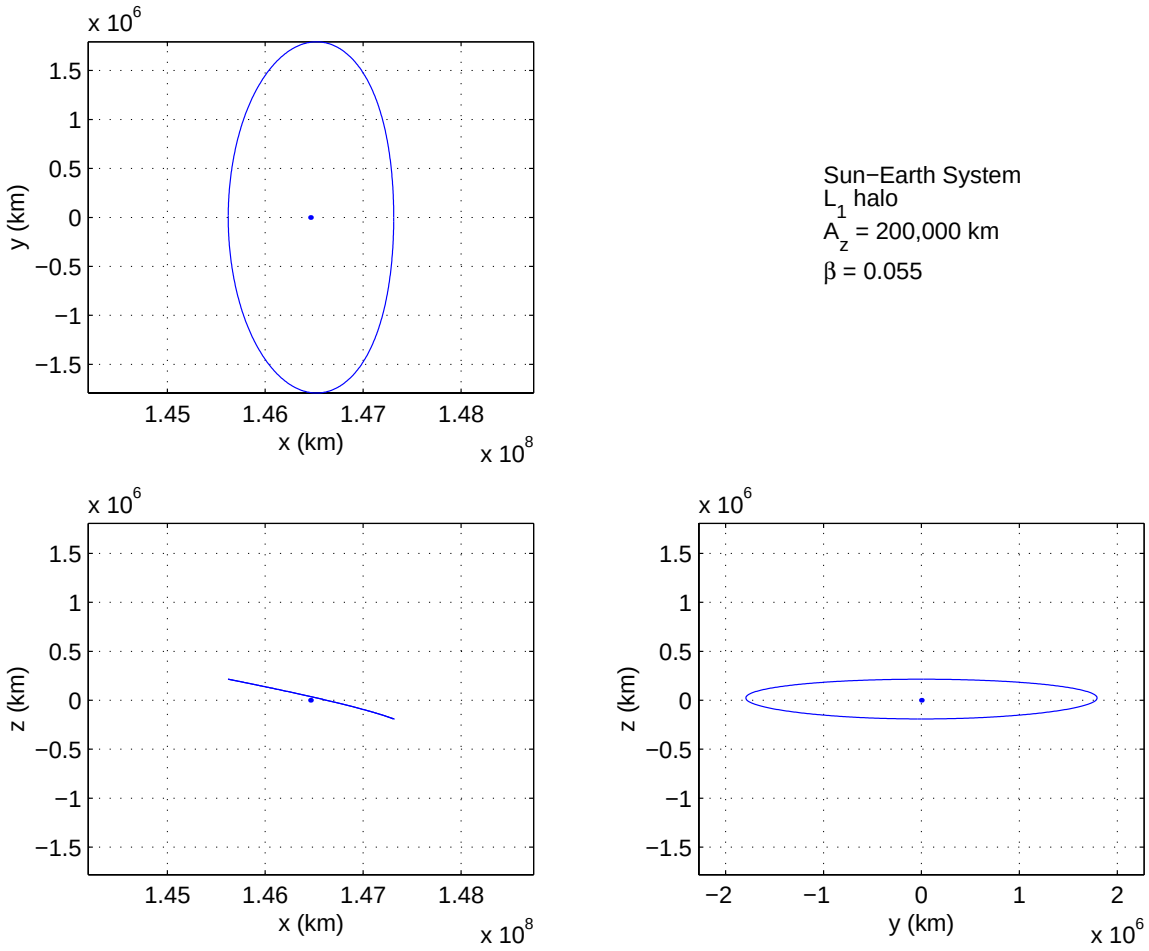

Figure 3.18. Nominal Sun-Earth L_1 halo orbit for $\beta = 0.055$

Table 3.2. Stationkeeping results for reference periodic L_1 halo orbit incorporating $\beta = 0.055$ (nominal period: 310 days)

$\sigma_\theta = 0.001°$			
	t_{min} = 30 days	t_{min} = 60 days	t_{min} = 80 days
Δt_1 (days)	70	90	130
Δt_2 (days)	110	130	180
Avg. completed revs	4.0	3.85	3.87
Avg. max. deviation (km)	7,350	35,840	27,500
Avg. $\delta\alpha$ (degrees)	0.0011	0.0040	0.0016
Avg. $\delta\gamma$ (degrees)	0.0	0.0	0.0

$\sigma_\theta = 0.01°$			
	t_{min} = 30 days	t_{min} = 60 days	t_{min} = 80 days
Δt_1 (days)	70	90	130
Δt_2 (days)	110	130	180
Avg. completed revs	3.59	2.71	2.75
Avg. max. deviation (km)	40,730	49,180	44,880
Avg. $\delta\alpha$ (degrees)	0.0087	0.0089	0.0050
Avg. $\delta\gamma$ (degrees)	0.0	0.0	0.0

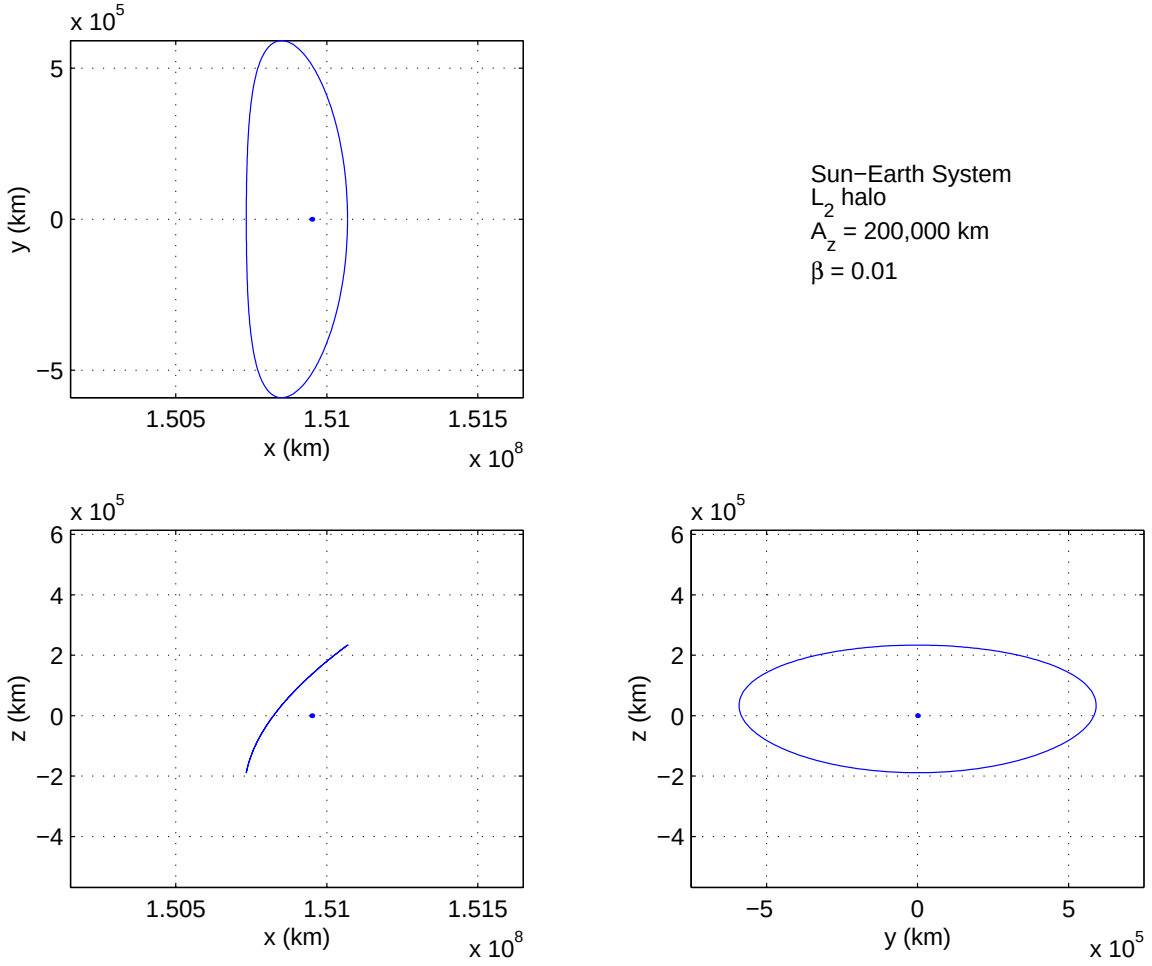

Figure 3.19. Nominal Sun-Earth L_2 halo orbit for $\beta = 0.01$

Table 3.3. Stationkeeping results for reference periodic L_2 halo orbit incorporating $\beta = 0.01$ (nominal period: 160 days)

$\sigma_\theta = 0.01^\circ$	
	t_{min} = 30 days
Δt_1 (days)	70
Δt_2 (days)	110
Avg. completed revs	3.97
Avg. max. deviation (km)	13,400
Avg. $\delta\alpha$ (degrees)	0.0273
Avg. $\delta\gamma$ (degrees)	0.0

4. Off-Axis Solutions

The equilibrium solutions associated with the differential equations that incorporate a solar sail force are presented and discussed in Chapters 2 and 3. It is apparent from Figures 2.6 and 2.7 that the on-axis libration points that exist along the $\hat{x}$-axis form an extremely small subset of the artificial libration points that are available with a solar sail. The "off-axis" libration points form a complementary set to the on-axis subset, and is, by far, the larger of the two sets. The off-axis libration points offer the ability to fix the location of a spacecraft at positions either above or below the plane of primary motion; new locations within the plane of motion can also be explored as potential hover points, or as a basis from which new periodic or bounded solutions might be generated.

It was established in Chapter 2 that the location of an artificial libration point is a function of sail lightness and orientation. Thus, a libration point can be generated anywhere within the interior of the bounding surface S_1, subject to the constraints of sail lightness values that are currently technologically feasible. The nominal values of β, α, and γ that correspond to the desired libration point can then be determined by evaluating equations (2.68), (2.69), and (2.70). Given an artificial libration point, an understanding of the motion in the vicinity of the point can be gained by examining the stability characteristics of the libration point. If the libration point is not asymptotically stable, motion that remains bounded in the vicinity of the libration point, if available, offers an alternative for mission scenarios that require the spacecraft to remain stationary relative to the rotating frame. Bounded orbits in the vicinity of a libration point may actually be preferred over asymptotic stability for some mission applications. This chapter reviews the stability and controllability characteristics of the off-axis libration points, as presented in McInnes, McDonald, Simmons, and

MacDonald [34]. In general, the libration points not asymptotically stable, but are controllable. Thus, a linear state feedback controller is developed, and the performance tested in the nonlinear system. Several different trajectories resulting from the state feedback control are discussed.

4.1 Libration Point Stability

The stability of the libration points can be determined by examining the eigenvalues of the system that results from linearization relative to the equilibrium point. Recall that, in the classical restricted three-body problem, the state space form of the variational equations relative to a libration point, from equation (2.26), is written

$$\dot{\overline{\xi}} = \mathbf{A}\overline{\xi} \ , \tag{4.1}$$

where the constant 6×6 matrix $\mathbf{A}$ is of the form

$$\mathbf{A} \equiv \begin{bmatrix} \mathbf{0} & \mathbf{I}_3 \\ \mathbf{B} & \mathbf{C} \end{bmatrix} \ .$$

Once the solar sail force is incorporated into the model, the matrix $\mathbf{A}$ retains this same general form. However, the 3×3 submatrix $\mathbf{B}$ is augmented such that,

$$\mathbf{B} \equiv \begin{bmatrix} U^*_{xx} + a^*_{xx} & U^*_{xy} + a^*_{xy} & U^*_{xz} + a^*_{xz} \\ U^*_{yx} + a^*_{yx} & U^*_{yy} + a^*_{yy} & U^*_{yz} + a^*_{yz} \\ U^*_{zx} + a^*_{zx} & U^*_{zy} + a^*_{zy} & U^*_{zz} + a^*_{zz} \end{bmatrix} \ ,$$

where $a_{jk} = \frac{\partial a_j}{\partial k}$ and $a^*_{jk} = a_{jk}|_{L_i}$. Recall that the expressions for the partial derivatives of a_x, a_y, and a_z with respect to the position coordinates appear in Appendix D. Note that this form of the linearized system relative to the libration point differs from that presented in Chapter 3. For values of α other than $\alpha = 0°$, the solar sail acceleration is not conservative, and, thus, the impact of the sail force must be accommodated as an additional term, rather than incorporated into a modified pseudo-potential.

The eigenvalues of $\mathbf{A}$ are solutions to the characteristic polynomial,

$$P(s) = \det(\mathbf{A} - s\mathbf{I}) = \sum_{i=0}^{6} c_i s^i = 0 \ , \tag{4.2}$$

where the coefficients, c_i, are

$$
\begin{aligned}
c_6 &= 1 \,, \\
c_5 &= 0 \,, \\
c_4 &= 4 - (U^*_{xx} + U^*_{yy} + U^*_{zz} + a^*_{xx} + a^*_{yy} + a^*_{zz}) \,, \\
c_3 &= 2(U^*_{xy} + a^*_{xy} - U^*_{yx} - a^*_{yx}) \,, \\
c_2 &= (U^*_{zz} + a^*_{zz})(U^*_{xx} + a^*_{xx}) + (U^*_{zz} + a^*_{zz})(U^*_{yy} + a^*_{yy}) - (U^*_{yx} + a^*_{yx})(U^*_{xy} + a^*_{xy}) \\
&\quad + (U^*_{xx} + a^*_{xx})(U^*_{yy} + a^*_{yy}) - (U^*_{yz} + a^*_{yz})(U^*_{zy} + a^*_{zy}) \\
&\quad - (U^*_{xz} + a^*_{xz})(U^*_{zx} + a^*_{zx}) - 4(U^*_{zz} + a^*_{zz}) \,, \\
c_1 &= 2(U^*_{zz} + a^*_{zz})(U^*_{yx} + a^*_{yx}) - 2(U^*_{zz} + a^*_{zz})(U^*_{xy} + a^*_{xy}) \\
&\quad - 2(U^*_{yz} + a^*_{yz})(U^*_{zx} + a^*_{zx}) + 2(U^*_{xz} + a^*_{xz})(U^*_{zy} + a^*_{zy}) \,, \\
c_0 &= (U^*_{zz} + a^*_{zz})(U^*_{yx} + a^*_{yx})(U^*_{xy} + a^*_{xy}) - (U^*_{zx} + a^*_{zx})(U^*_{yz} + a^*_{yz})(U^*_{xy} + a^*_{xy}) \\
&\quad + (U^*_{zx} + a^*_{zx})(U^*_{xz} + a^*_{xz})(U^*_{yy} + a^*_{yy}) - (U^*_{zz} + a^*_{zz})(U^*_{xx} + a^*_{xx})(U^*_{yy} + a^*_{yy}) \\
&\quad - (U^*_{xz} + a^*_{xz})(U^*_{zy} + a^*_{zy})(U^*_{yx} + a^*_{yx}) + (U^*_{yz} + a^*_{yz})(U^*_{zy} + a^*_{zy})(U^*_{xx} + a^*_{xx}) \,.
\end{aligned}
$$

The potential for asymptotic stability of an artificial libration point can be evaluated by application of the Routh-Hurwitz stability criterion [47]. Since $c_5 = 0$, there is always at least one eigenvalue with a real part greater than or equal to zero. Therefore, the artificial libration points are *not* asymptotically stable. The values of the remaining eigenvalues are not clear from this analysis, and, likely to depend on the particular off-axis point that is examined.

4.2 Bounded Motion

Since asymptotically stable trajectories are not available, alternative solutions (such as bounded, periodic, and quasi-periodic motion) to achieve the same mission objectives are required. Unlike the classical restricted three-body problem, which has only five libration points, the addition of a solar sail creates an infinite number of potential artificial libration points, that cannot be examined individually to determine their stability properties. Fortunately, a general understanding of the conditions required for the existence of bounded motion is available. An initial step in obtaining solutions exhibiting bounded behavior is the construction of an oscillatory first-order approximate solution; such an approach requires the existence of purely imaginary

eigenvalues. As presented in [34], conditions for the existence of purely imaginary eigenvalues can be established with the substitution $s = i\omega$. Thus, the form of the characteristic polynomial becomes

$$P(i\omega) = -\omega^6 + c_4\omega^4 - ic_3\omega^3 - c_2\omega^2 + ic_1\omega + c_0 = 0 \ . \tag{4.3}$$

Purely imaginary eigenvalues will exist if there is a consistent solution to equation (4.3), with $\omega \in \Re$. This requires the following relationships to be true, i.e.,

$$-\omega^6 + c_4\omega^4 - c_2\omega^2 + c_0 = 0 \ , \tag{4.4}$$

$$i\omega(c_1 - c_3\omega^2) = 0 \ . \tag{4.5}$$

The three solutions to equation (4.5), $\omega = 0, +\sqrt{c_1/c_3}, -\sqrt{c_1/c_3}$, are not generally consistent with equation (4.4). Therefore, in general, the linearized system does not possess purely imaginary eigenvalues. However, consistent solutions can be obtained by introducing the condition $c_1 = c_3 = 0$, that is, effectively isolating a subset of libration points that have the potential for producing bounded motion. This condition satisfies equation (4.5), and allows consistent solutions to be obtained from equation (4.4). These solutions are not guaranteed to be real, and, thus, the condition is a necessary, but not sufficient, condition for the existence of imaginary eigenvalues.

The requirement that the coefficients c_1 and c_3 be identically zero requires that

$$\begin{aligned} &(U^*_{zz} + a^*_{zz})(U^*_{yx} + a^*_{yx}) - (U^*_{zz} + a^*_{zz})(U^*_{xy} + a^*_{xy}) \\ &-(U^*_{yz} + a^*_{yz})(U^*_{zx} + a^*_{zx}) + (U^*_{xz} + a^*_{xz})(U^*_{zy} + a^*_{zy}) = 0 \ , \end{aligned} \tag{4.6}$$

$$U^*_{xy} + a^*_{xy} - U^*_{yx} - a^*_{yx} = 0 \ . \tag{4.7}$$

Since the pseudo-potential is conservative, it is always true that $U_{xy} - U_{yx} = U_{xz} - U_{zx} = U_{yz} - U_{zy} = 0$. Thus, equations (4.6) and (4.7) reduce to the set

$$\begin{aligned} &U^*_{zz}(a^*_{yx} - a^*_{xy}) + a^*_{zz}a^*_{yx} - a^*_{zz}a^*_{xy} + U^*_{yz}(a^*_{xz} - a^*_{zx}) \\ &+U^*_{xz}(a^*_{zy} - a^*_{yz}) + a^*_{xz}a^*_{zy} - a^*_{yz}a^*_{zx} = 0 \ , \end{aligned} \tag{4.8}$$

$$a^*_{xy} - a^*_{yx} = 0 \ . \tag{4.9}$$

These equations are satisfied if $a_{xy} - a_{yx} = a_{xz} - a_{zx} = a_{yz} - a_{zy} = 0$, a result that implies either $\beta = 0$, or

$$\overline{\nabla} \times \overline{a} = 0 \ . \tag{4.10}$$

Thus, pure imaginary eigenvalues exist only if the solar radiation pressure force is zero (the classical restricted three-body problem), or it is conservative (i.e., $\alpha = 0^\circ$) [34].

4.3 Libration Point Control

Recall that each artificial libration point corresponds to a specific combination of sail orientation angles. The condition $\alpha = 0^\circ$ specifies an extremely small subset of the wider range of libration points that are available. Thus, the stability results derived previously imply that, in general, to remain in the vicinity of an arbitrary artificial libration point requires some kind of stabilizing control. Fortunately, the solar sail itself can provide that control, by varying the sail orientation angles relative to the incident solar radiation [30, 34, 35]. This approach is not as flexible as it might be, since it provides just two control variables, while the thrust vector actually has the three components that can be varied to produce control actions. An additional control element could be provided by varying the sail lightness parameter, thus, effectively varying the magnitude of the thrust generated by the solar sail. However, this would require alternately furling and unfurling the sail, which is considered less practical than simply implementing changes in the orientation, under the conditions that two control variables are sufficient. Nevertheless, adjustment of β during flight is not examined in this study. A continuous-time linear state feedback controller is selected as a simple "proof-of-concept" for control using only sail orientation variations.

The sail orientation control variables are defined such that

$$\delta\alpha = \alpha - \alpha_{L_i} \ , \quad \text{and} \quad \delta\gamma = \gamma - \gamma_{L_i} \ ,$$

where α_{L_i} and γ_{L_i} are the nominal sail angles corresponding to the libration point of interest. Incorporating the control variables, the linear variational system from

equation (4.1) becomes

$$\dot{\overline{\xi}} = \mathbf{A}\overline{\xi} + \mathbf{P}\delta\overline{\theta} \; , \tag{4.11}$$

where $\delta\overline{\theta} = [\delta\alpha \;\; \delta\gamma]^T$, and the 6×2 matrix $\mathbf{P}$ has the form

$$\mathbf{P} \equiv \begin{bmatrix} \mathbf{0} \\ \mathbf{D} \end{bmatrix} \; .$$

As in Chapter 3, the submatrix $\mathbf{D}$ corresponds to the partial derivatives of the sail acceleration with respect to the sail orientation angles. However the elements of the matrix are evaluated at the libration point, and thus the matrix is constant, and appears as

$$\mathbf{D} \equiv \begin{bmatrix} a^*_{x\alpha} & a^*_{x\gamma} \\ a^*_{y\alpha} & a^*_{y\gamma} \\ a^*_{z\alpha} & a^*_{z\gamma} \end{bmatrix} \; ,$$

where $a_{jk} = \frac{\partial a_j}{\partial k}$ (see Appendix E), and $a^*_{jk} = a_{jk}|_{L_i}$, that is, the partial derivatives evaluated at the libration point. The controllability of this system can be determined by from the 6×12 controllability matrix $\mathbf{V}_c = [\mathbf{P} \;\; \mathbf{AP} \;\; \mathbf{A}^2\mathbf{P} \;\; \mathbf{A}^3\mathbf{P} \;\; \mathbf{A}^4\mathbf{P} \;\; \mathbf{A}^5\mathbf{P}]$; evaluated at the libration point of interest, the matrix should be of rank 6. In general, if the sail is not oriented parallel to the solar radiation (i.e., if $\hat{r}_1 \cdot \hat{n} \neq 0$ or equivalently, $\alpha \neq \pm 90^\circ$), the system will be controllable. It should therefore be possible to construct a controller to stabilize an arbitrary libration point.

The feedback control is defined such that the sail orientation angles, α and γ, are functions of the spacecraft position and velocity relative to the libration point. That is,

$$\delta\overline{\theta} = \mathbf{G}\overline{\xi} \; , \tag{4.12}$$

where $\mathbf{G}$ is the 2×6 gain matrix. The closed-loop linearized system from equation (4.11) is rewritten in the form

$$\dot{\overline{\xi}} = (\mathbf{A} + \mathbf{PG})\overline{\xi} \; . \tag{4.13}$$

The elements of the gain matrix are then selected such that the eigenvalues of the composite matrix $(\mathbf{A} + \mathbf{PG})$ all possess real parts < 0, implying that the system is

stable. Once a gain matrix has been determined for a given libration point, it can be used to compute the sail orientation angles at each time step in the numerical integration of the nonlinear equations of motion. Using the numerically integrated state, the sail angles are evaluated from the following expressions,

$$\begin{aligned} \alpha &= \alpha_{L_i} + G_{11}(x - x_{L_i}) + G_{12}(y - y_{L_i}) + G_{13}(z - z_{L_i}) \\ &\quad + G_{14}\dot{x} + G_{15}\dot{y} + G_{16}\dot{z} \ , \end{aligned} \tag{4.14}$$

$$\begin{aligned} \gamma &= \gamma_{L_i} + G_{21}(x - x_{L_i}) + G_{22}(y - y_{L_i}) + G_{23}(z - z_{L_i}) \\ &\quad + G_{24}\dot{x} + G_{25}\dot{y} + G_{26}\dot{z} \ , \end{aligned} \tag{4.15}$$

where G_{jk} are the elements of the gain matrix, and $(x_{L_i},\ y_{L_i},\ z_{L_i})$ represents the location of the corresponding nominal libration point relative to the barycenter. This technique has been successfully used to asymptotically stabilize various artificial libration points. An example appear in Figure 4.2. The libration point in this example, denoted L_A, is arbitrarily selected at (0.8 AU, 0.2 AU, -0.3 AU) relative to the barycenter. (See Figure 4.1.) The corresponding sail lightness is $\beta = 0.59$, and the nominal sail orientation angles are $\alpha = 28.29°$ and $\gamma = 179.99°$. From an arbitrary set of initial conditions in the vicinity of L_A, the asymptotically stable trajectory is propagated in the nonlinear system, arrives at L_A after approximately 200 days, and remains fixed for the remainder of the integration. The corresponding time history for the sail orientation angles appears in Figure 4.3. Since the gain matrix is derived from a linear approximation, this form of the control does not stabilize the entire nonlinear system. The distance from the libration points within which the linear approximation remains valid has been determined experimentally to vary for different libration points, but in some cases extends to approximately 150,000 km.

For some mission objectives, it may be desirable to orbit in the vicinity of a libration point, instead of remaining fixed at the point. However, the linear state feedback controller can be adapted to this scenario as well. By selecting the gain matrix, $\mathbf{G}$, such that the eigenvalues of the composite matrix $(\mathbf{A} + \mathbf{PG})$ are all purely imaginary, an oscillatory linear system is created. The gain matrix can again

be incorporated into the nonlinear system as specified in equations (4.14) and (4.15). An arbitrarily selected initial perturbation will then result in a bounded, Lissajous-type trajectory. By selecting an initial perturbation that is a scalar multiple of one of the eigenvectors of $(\mathbf{A}+\mathbf{PG})$, a single oscillatory mode can be excited, resulting in a periodic or quasi-periodic orbit depending on the validity of the linear approximation at the selected distance from the nominal libration point. An example of a quasi-periodic orbit appears in Figure 4.4. The libration point in this example, denoted L_B, is selected at (0.5 AU, 0.5 AU, 0.5 AU) relative to the barycenter. (See Figure 4.1.) The corresponding sail lightness is $\beta = 0.83$, and the nominal sail orientation angles are $\alpha = 28.37°$ and $\gamma = 0.00016°$. From an initial state generated by a perturbation relative to the nominal libration point in the direction of one of the eigenvectors of $(\mathbf{A}+\mathbf{PG})$, the quasi-periodic trajectory in the figure was integrated for 1.5 years in the nonlinear system. The time history for the sail orientation angles corresponding to this trajectory appears in Figure 4.5.

A controller to maintain periodic or quasi-periodic trajectories using maneuvers performed at discrete time intervals was also attempted. The approach used is based on the "target-point" method of computing Lissajous trajectories developed by Howell and Pernicka [22]. The target-point algorithm is modified to incorporate sail orientation information, and periodic orbits generated using continuous control are used to provide initial guesses. However, the resulting controller is unsuccessful in maintaining a bounded trajectory. Attempts to force a closed orbit resulted in the controlled trajectory collapsing to the libration point. It is not clear whether this lack of success is due to an insufficiently accurate initial guess, or simply lack of sufficient control capability. A more complete analysis is necessary.

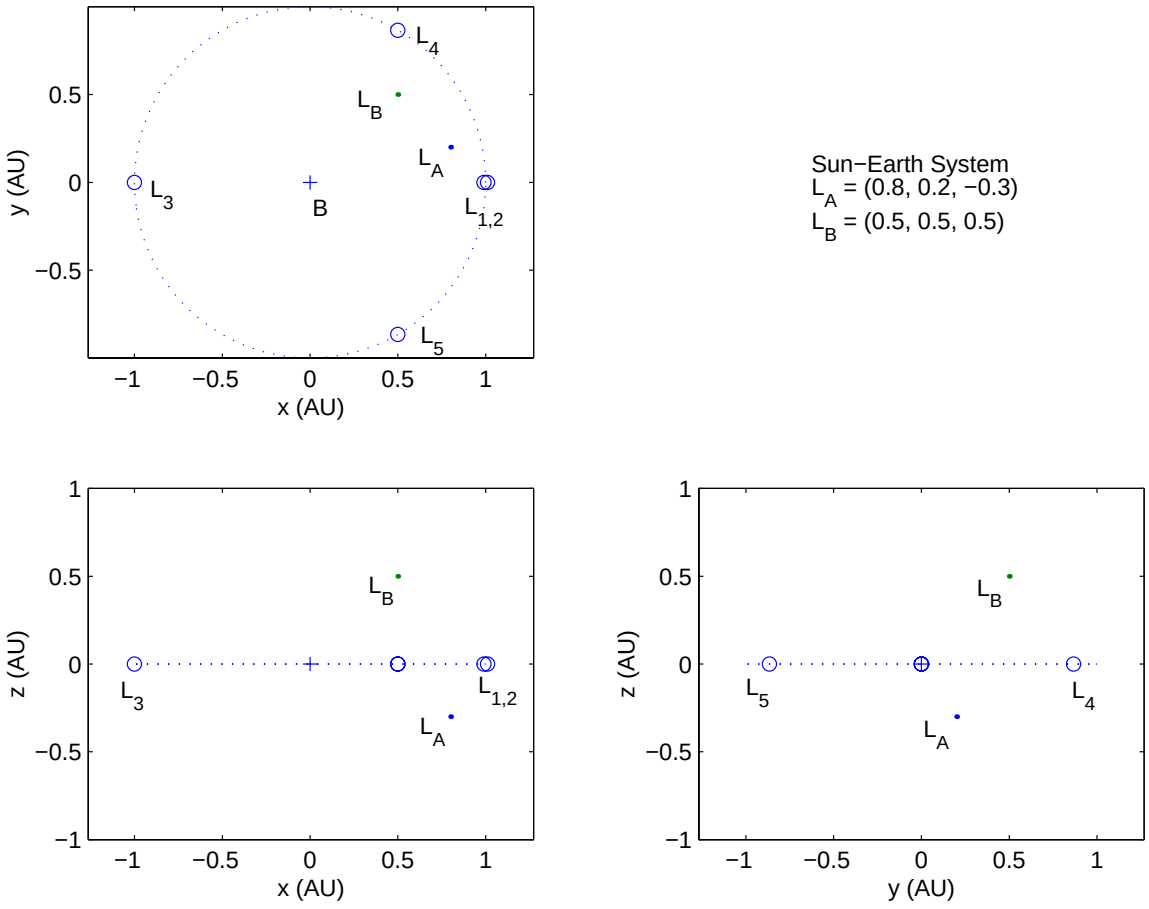

Figure 4.1. Locations of the example off-axis libration points

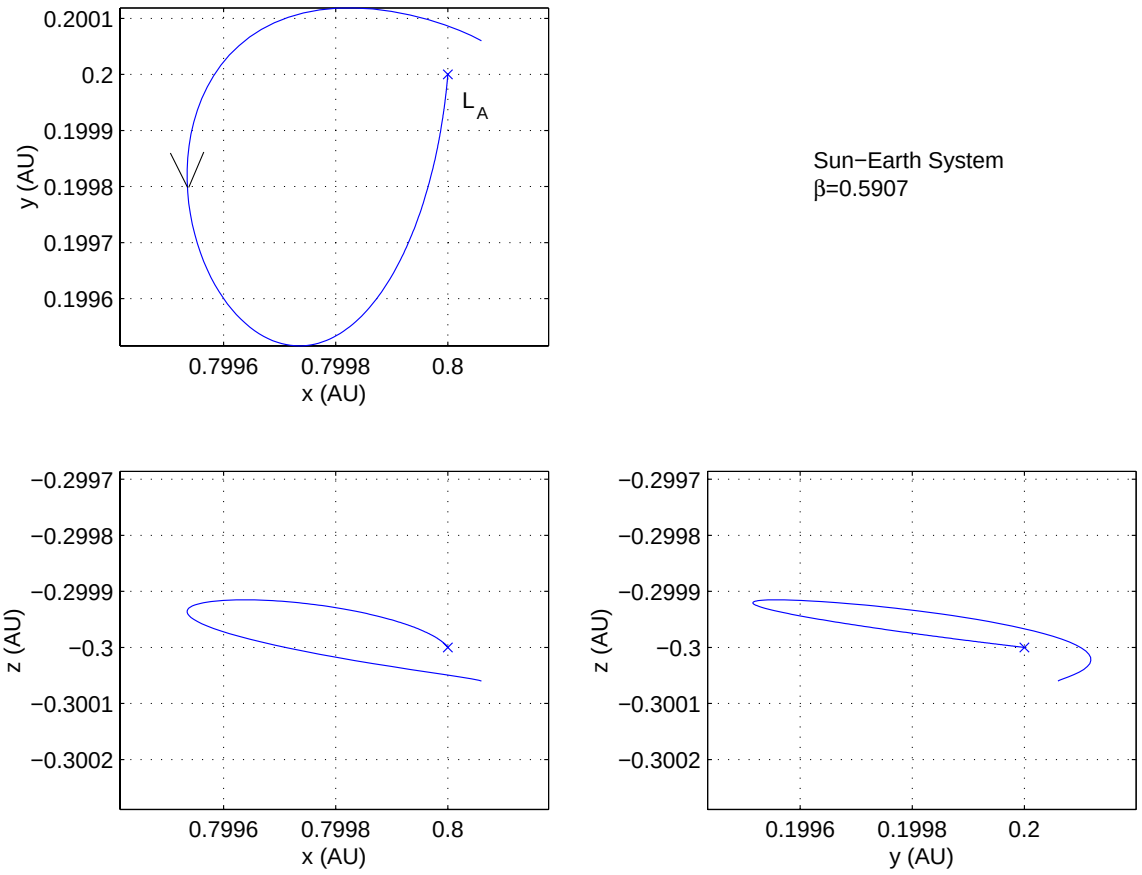

Figure 4.2. Example: asymptotically stable trajectory

Initial state relative to L_A:

$$\begin{aligned}
\xi &= +100,000 \text{ km} , \\
\eta &= +100,000 \text{ km} , \\
\zeta &= +100,000 \text{ km} , \\
\dot{\xi} &= +1 \text{ m/s} , \\
\dot{\eta} &= -1 \text{ m/s} , \\
\dot{\zeta} &= +1 \text{ m/s} .
\end{aligned}$$

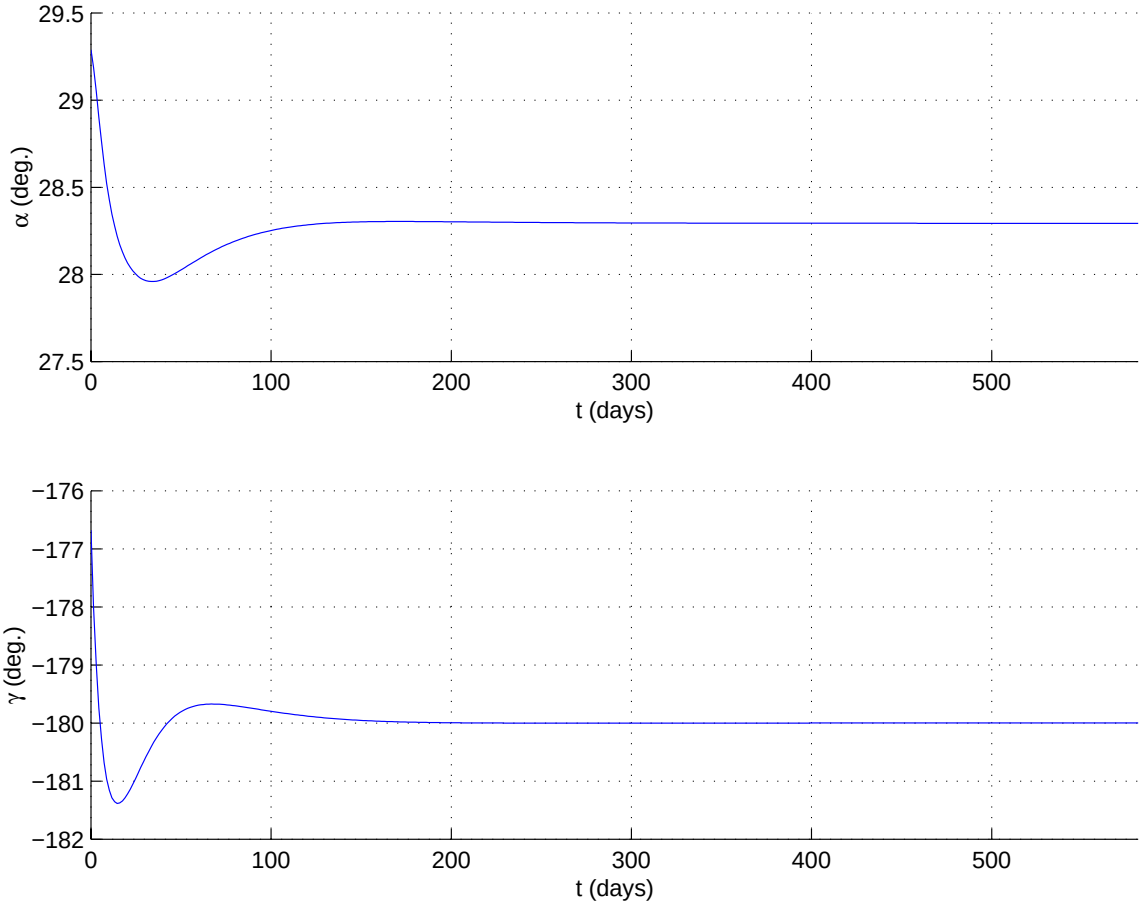

Figure 4.3. Orientation angle time history for the asymptotically stable trajectory

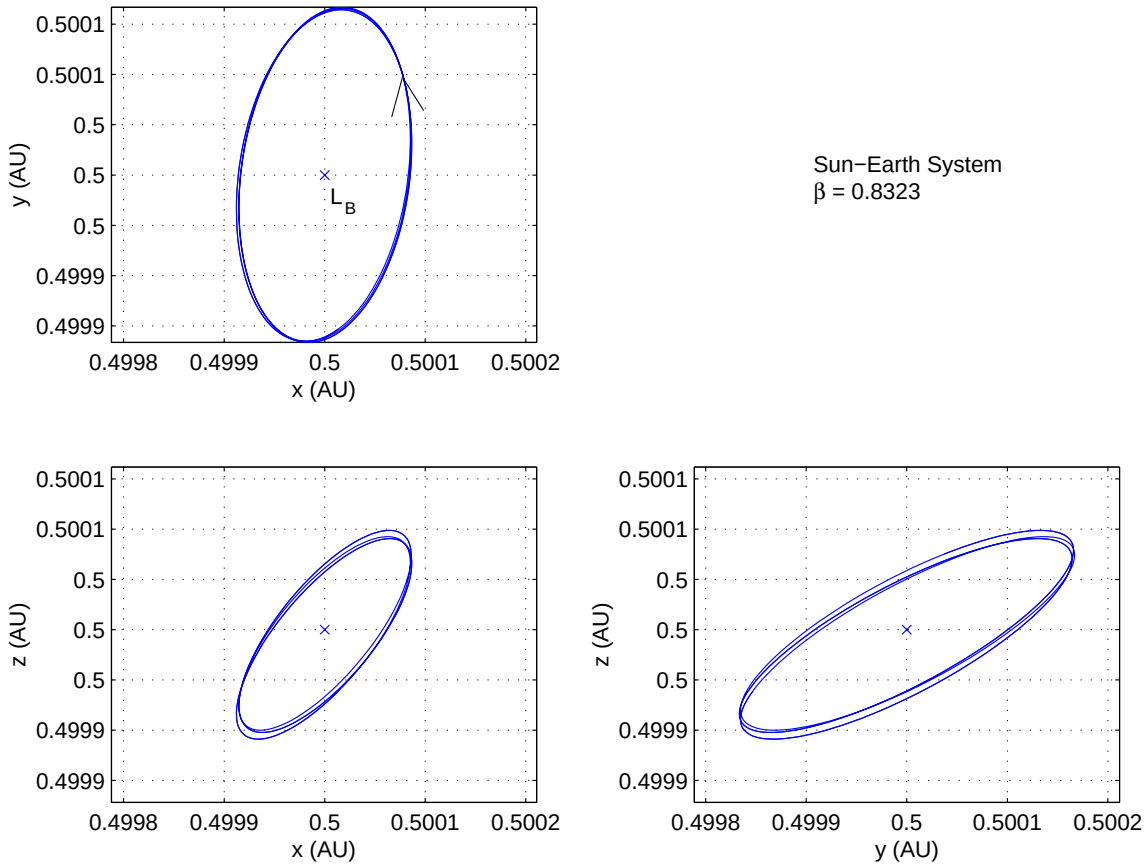

Figure 4.4. Example: quasi-periodic trajectory

Initial state relative to L_B:

$$\begin{aligned}
\xi &= +13,000 \text{ km}, \\
\eta &= +5,000 \text{ km}, \\
\zeta &= +11,000 \text{ km}, \\
\dot{\xi} &= -0.19 \text{ m/s}, \\
\dot{\eta} &= +14.4 \text{ m/s}, \\
\dot{\zeta} &= +5.7 \text{ m/s}.
\end{aligned}$$

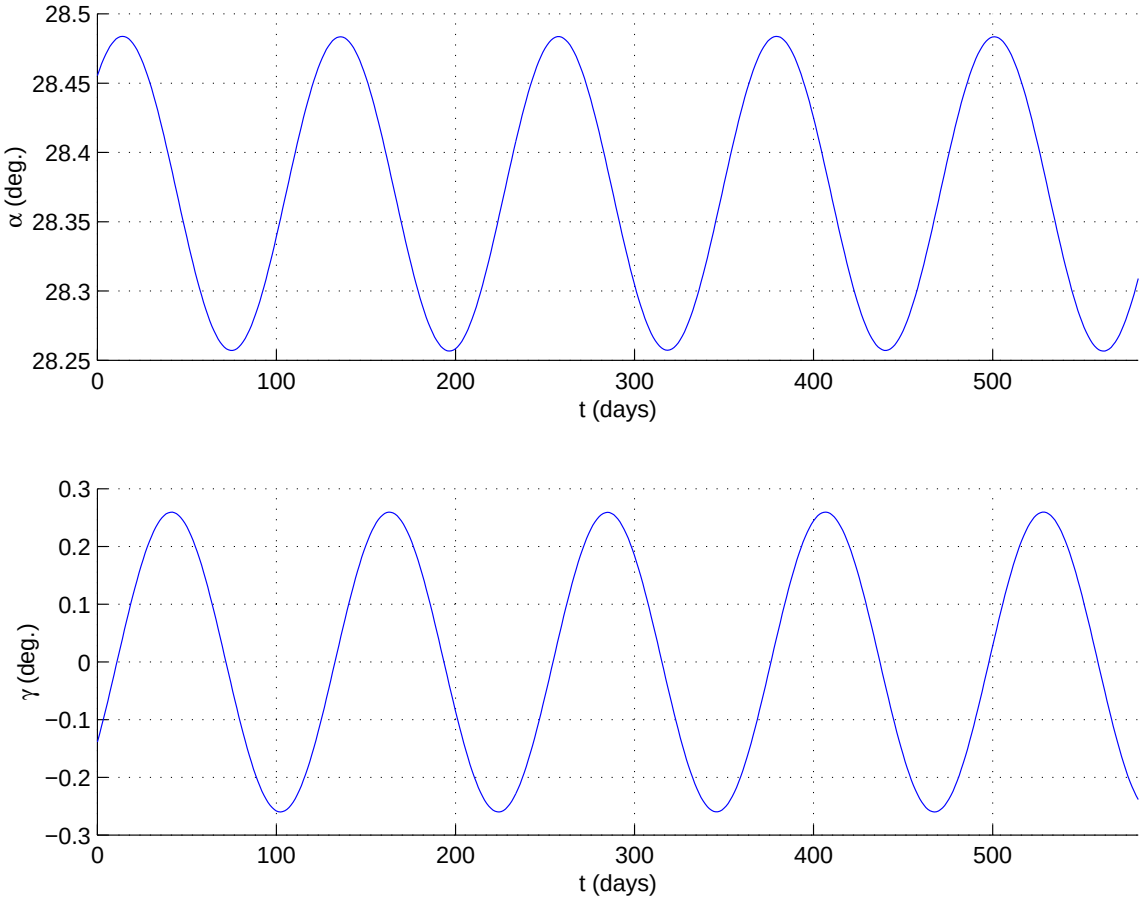

Figure 4.5. Orientation angle time history for the quasi-periodic trajectory

5. Transfers

One challenge in the trajectory design process for an actual mission, is the determination of a transfer that moves the spacecraft from some Earth parking orbit to a desired libration point orbit. The inclusion of a solar sail propulsion system brings with it a large range of available transfer trajectory options. Selecting the optimal transfer involves the solution of a two-point boundary value problem, and is typically accomplished using specialized trajectory optimization software.

The work outlined in this chapter focuses on techniques for developing transfer trajectories between Earth and the periodic orbits that exist in the vicinity of the "on-axis" libration points that, while not optimal, serve as good baseline transfers and are a key component in the conceptual development of an end-to-end trajectory design. The "natural" motion of the spacecraft, that is, the motion with the sail in some fixed attitude and without variations in the orientation, provides a reasonable starting point for the transfer design process. A targeting algorithm is then introduced, one specifically defined to take advantage of the additional flexibility afforded by the inclusion of a solar sail. Transfers to the off-axis libration points or orbits in their vicinity are not examined, although similar techniques could likely be applied in that regime.

5.1 Manifolds

From dynamical systems theory [39], it is known that the stable manifold, W^s, associated with a periodic orbit represents the set of all states in the basin of attraction that converge to the orbit as $t \to \infty$. Ideally, then, a transfer to a periodic orbit should at some point intersect and merge with a trajectory that is a member of W^s; such an asymptotic approach implies zero insertion cost. Similarly, the unstable manifold,

W^u, is the set off all states that converge to the periodic orbit as $t \to -\infty$, and, thus, is associated with departures from the orbit at no cost. Stable and unstable manifolds have been used in the design of transfer trajectories for libration point missions such as Genesis [4, 24] and Triana [5].

Recall that the linear variational equations and the monodromy matrix, defined as the state transition matrix after one period of the orbit, can be used to obtain stability information about a periodic orbit. The eigenvectors of the monodromy matrix that are associated with the stable eigenvalues (i.e., $|\lambda_i^s| < 1$) span the stable subspace E^s. Likewise, the unstable subspace, E^u, is spanned by the eigenvectors associated with the unstable eigenvalues (λ_i^u). Near the fixed point that represents a periodic orbit in a Poincaré section [39], then, W^s and W^u, corresponding to the nonlinear system, are tangent to the subspaces E^s and E^u, respectively. The "local" stable or unstable manifold, that is, the manifold in the vicinity of a fixed point, can, thus, be approximated by the stable or unstable eigenspace. In practice, the approximation for a trajectory that lies on the local stable or unstable manifold associated a fixed point along a periodic orbit is computed by perturbing the orbit state by some small amount, ϵ, in the direction of a vector along the stable or unstable eigenvector at that point. This approximation is then "globalized" by numerically integrating the perturbed state backward and/or forward in time. This procedure is repeated for a set of points around the orbit to gain an understanding of the character of the complete manifold.

Recall that an on-axis "solar sail halo orbit" is generated by fixing the sail orientation such that the sail normal vector ($\hat{n}$) is always parallel to the Sun-spacecraft vector ($\overline{r}_1$), then using a differential corrections process to determine an initial state vector that produces a periodic orbit. For the computation of the stable and unstable manifolds, the "natural" motion of the spacecraft is defined as the trajectory that results when the sail orientation corresponds to that used in the computation of the "solar sail halo orbit." Thus, the globalized manifolds for the on-axis halo orbits are determined for sail angles equal to $\alpha = 0^\circ$ and $\gamma = 0^\circ$ along the entire length

of the trajectory. Stable manifolds corresponding to an L_1 halo orbit of amplitude $A_z = 200,000$km appear in Figure 5.1; this orbit and the set of trajectories representing the stable manifold are computed for a spacecraft *without* a solar sail. Now a sail is introduced through β (for $\alpha = \gamma = 0^\circ$), and the plot in Figure 5.1 can be compared with the plots in Figures 5.2 and 5.3. This comparison demonstrates the effect of an increasing the sail lightness parameter on the stable manifolds for two solar sail influenced $A_z = 200,000$km halo orbits. Obviously, the manifolds drift further from the Earth (represented by the dot at $x = 1$AU, $y = 0$AU) as β increases.

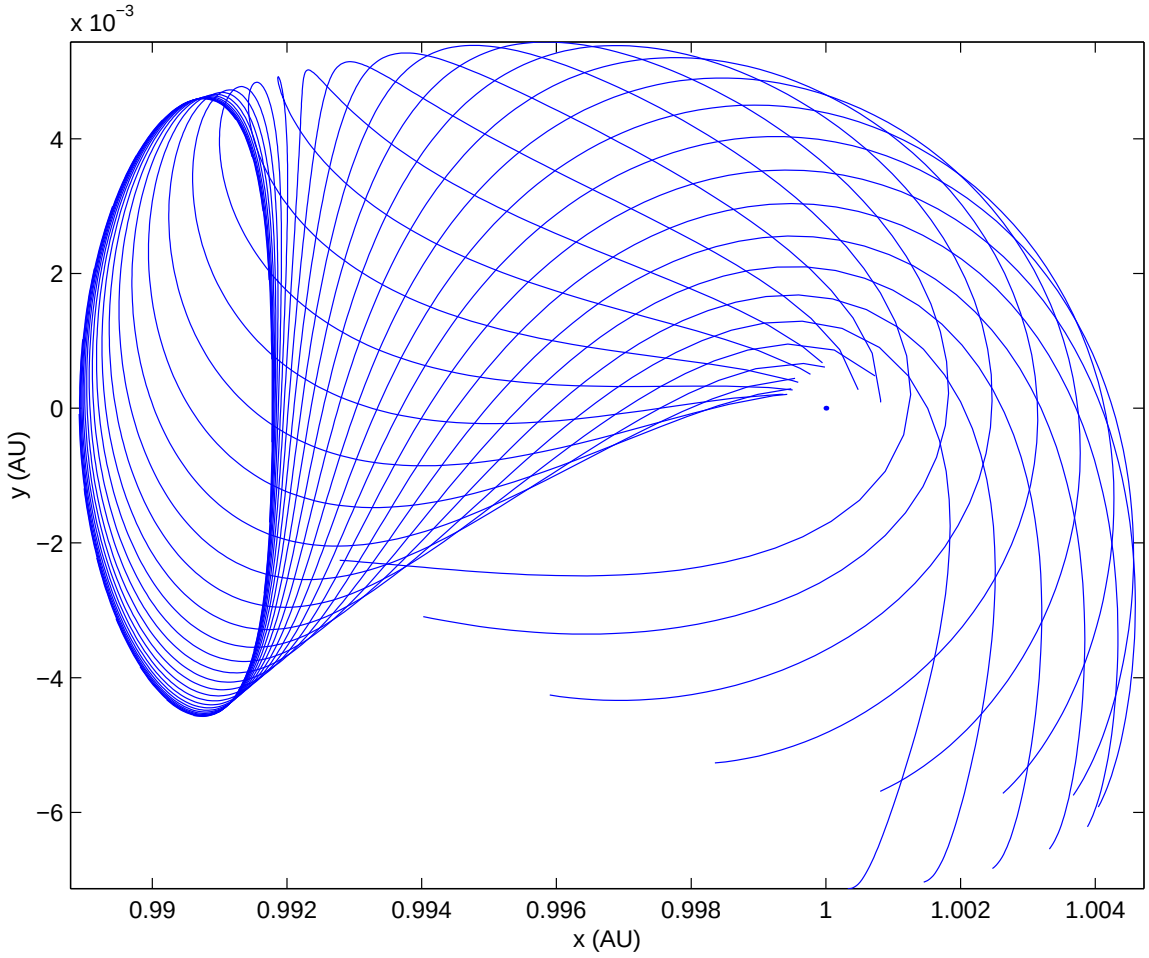

Figure 5.1. Stable manifold for a Sun-Earth L_1 halo (β=0.0)

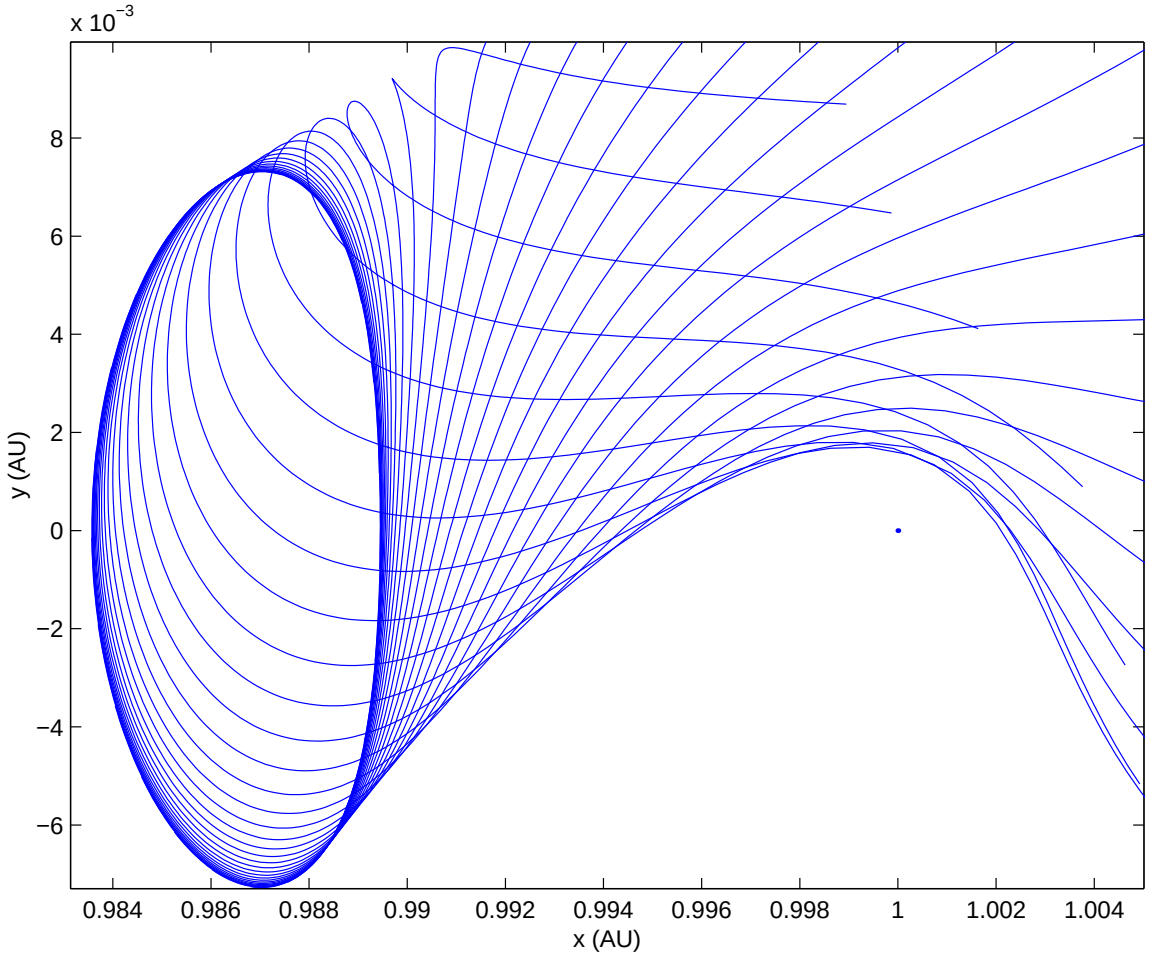

Figure 5.2. Stable manifold for a Sun-Earth L_1 halo (β=0.025)

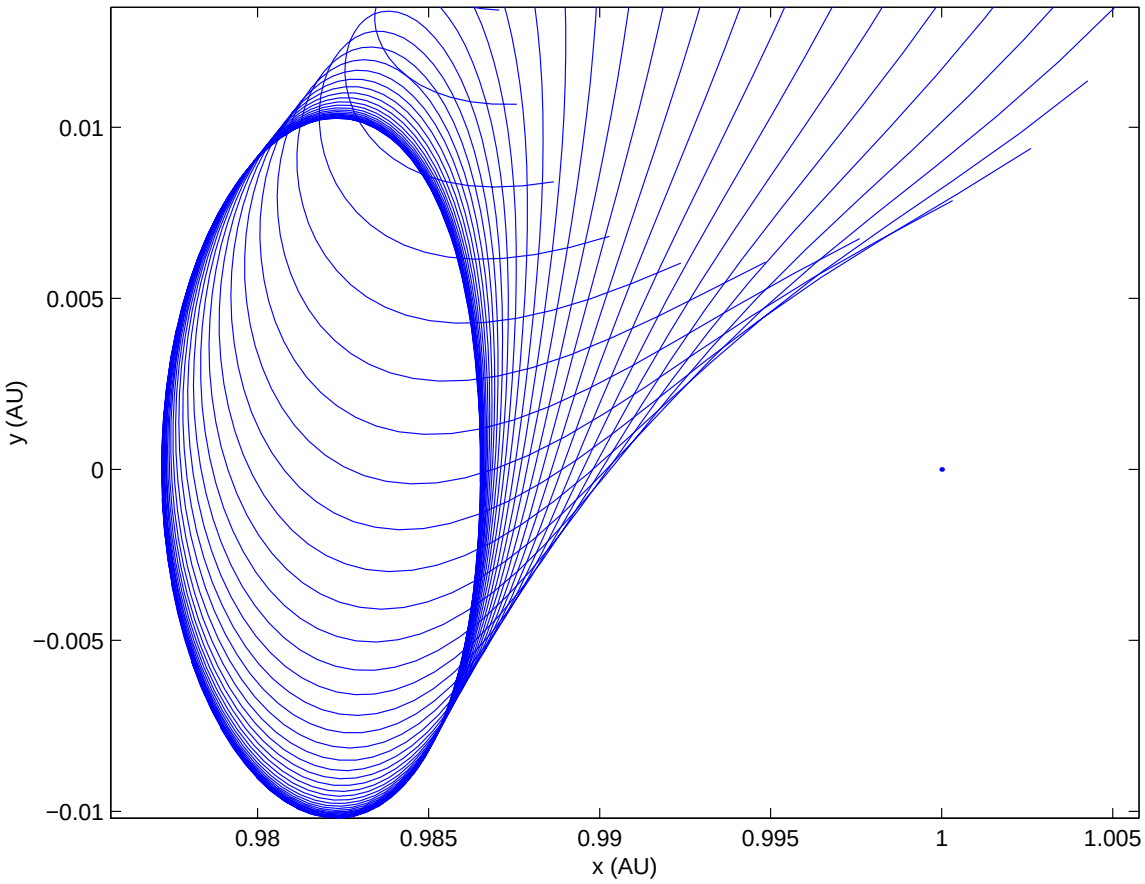

Figure 5.3. Stable manifold for a Sun-Earth L_1 halo (β=0.045)

5.2 Introducing Maneuvers

5.2.1 General Approach

Transfers to and from libration point orbits are constructed via a multi-step process, working "backwards" from the desired halo orbit. The first step is the determination of trajectories that represent the stable or unstable manifolds and pass sufficiently close to Earth such that they are accessible from geocentric parking orbits. This study focuses on transfers *to* a halo orbit, although the same methodology can probably be adapted to generate transfers *from* a halo as well. Barden [48] identified a region along the classical halo family, designated the "Earth-Access Region", that produces "manifold trajectories" useful for transfers. As noted by Nuss [38], and also observed in Figures 5.2 and 5.3, the region of the entire stable manifold surface that passes near the Earth shifts away as the sail lightness is increased. To counter this tendency, maneuvers that steer the spacecraft back towards the Earth must be introduced.

The approach used in this investigation to determine the placement and magnitude of the maneuvers is an adaptation of the "target-point" methodology developed by Howell and Pernicka [22] for the numerical determination of Lissajous trajectories. This is a two-level iterative process intended to create a bounded trajectory that possesses with certain, specified characteristics, and is continuous in position and velocity. Embedded in this scheme is a targeting algorithm that is exploited to design the transfer, incorporating the sail as part of the control scheme.

Initially, a trajectory representing a path along a manifold surface is split into n segments, with the states at the beginning and end of each segment defined as target points (numbered 0 to n). In the first level of the iterative process, the velocity and sail orientation at the beginning of each segment are adjusted to target the appropriate state at the end point of the segment. Thus, the segments are all "patched" together to create an end-to-end trajectory that is continuous in position, although not necessarily in velocity. Note that since the initial guess is a trajectory along a manifold that is already continuous, the first iteration at the first level of this process does not produce

any changes in the trajectory. In the second level of this scheme, a linear correction is applied simultaneously to the position of all target points, while also adjusting the sail orientation at each target point, to reduce any velocity discontinuities and force the terminal point of the trajectory closer to the Earth. Since the first iteration at the first level of the process introduces no velocity discontinuities, the first iteration at the second level produces corrections corresponding only to the desired change in the position of the terminal point of the trajectory. The linear corrections generated by the second level of the process result in a new set of target points, which define new trajectory segments. The first level of the process is then reapplied, to patch together the new trajectory segments. This process repeats until the terminal point of the trajectory, corresponding to the origin of the transfer in the "backwards" design process, is brought to within some acceptable distance of Earth, and the velocity discontinuities are such that the trajectory is essentially continuous. Thus, although five controls (i.e, the $\hat{x}$, $\hat{y}$, and $\hat{z}$ velocity components and the sail orientation angles) are used to allow the targeting process greater flexibility in making the intermediate steps from the initial guess to the final transfer trajectory, ideally the resulting transfer will make use of only two of those controls (i.e., the sail orientation angles). The resulting transfer is, thus, a trajectory that passes from the Earth to a libration point orbit, by altering the sail orientation at the target points, and maintaining constant sail orientation angles along the arcs between target points.

5.2.2 Ensuring Position Continuity

The first level of the iterative process is a straightforward application of a differential corrections method. Recall from equation (2.47) that the relationship between changes in the initial and final states is written

$$\delta\overline{x}(t_f) = \Phi(t_f, t_0)\delta\overline{x}(t_0) + \dot{\overline{x}}(t_f)\delta(t_f - t_0) \; . \tag{5.1}$$

Using the augmented state vector and state transition matrix that include contributions from changes in the sail angle, as defined in Section 3.4, a linear expression for the final position in terms of the initial velocity, the sail orientation, and the flight

time can be extracted from equation (5.1):

$$\overline{b} = \mathbf{V}\overline{u} \; , \tag{5.2}$$

where

$$\begin{aligned}
\mathbf{V} &= [\mathbf{L}_{f0} \quad \mathbf{E}_{f0} \quad \overline{v}] \; , & (5.3)\\
\mathbf{L}_{f0} &= \frac{\partial \overline{r}_{t_f}}{\partial \overline{v}_{t_0}} \; , & (5.4)\\
\mathbf{E}_{f0} &= \frac{\partial \overline{r}_{t_f}}{\partial \overline{\theta}} \; , & (5.5)\\
\overline{u} &= [\delta\dot{x}_0 \quad \delta\dot{y}_0 \quad \delta\dot{z}_0 \quad \delta\alpha \quad \delta\gamma \quad \delta(t_f - t_0)]^T \; , & (5.6)\\
\overline{b} &= [\delta x_f \quad \delta y_f \quad \delta z_f]^T \; , & (5.7)
\end{aligned}$$

and $\overline{v} = [\dot{x} \;\; \dot{y} \;\; \dot{z}]^T$. Then, a result from linear algebra states that the minimum norm solution to equation (5.2) can be computed by evaluation of the expression

$$\overline{u} = \mathbf{V}^T(\mathbf{V}\mathbf{V}^T)^{-1}\overline{b} \; . \tag{5.8}$$

Thus, equation (5.2) yields the changes in the initial velocity, the sail orientation angles, and the integration interval that are required to generate the desired final position. Changes in the initial position are not incorporated since the initial position state is fixed.

From the first target point, the equations of motion and the state transition matrix are numerically integrated over an estimated time interval enroute to the second target point. In general, the final position does not match the target position, and, therefore, requires correction. The initial velocity, the sail orientation, and the estimated integration interval are then adjusted according to equation (5.2). The integration is restarted at t_0 with the new initial state, and proceeds over the new time interval. This procedure is repeated until the final position equals the target position within some small tolerance. Once continuity is achieved between the first two target points, the process is applied to the segment between the second and third target points, and, in turn, all of the other segments that comprise the transfer trajectory. The result is a path that is continuous in position, but includes velocity discontinuities as well as discrete changes in sail orientation.

5.2.3 Enforcing Terminal Constraints and Velocity Continuity

Once position continuity is achieved, the task in the second level of the iterative process is to force the terminal point along the transfer path to meet certain constraints, while simultaneously reducing any velocity discontinuities. These objectives are achieved by manipulating the positions of all $n+1$ target points simultaneously, while also adjusting the sail orientations and segment integration intervals.

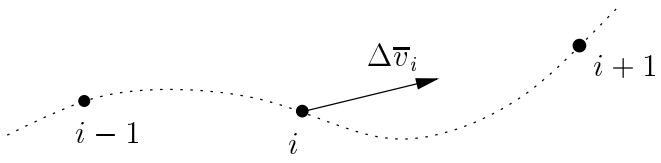

Figure 5.4. Patched transfer trajectory segments

Consider the ith target point as it appears in Figure 5.4. Let the subscript i^+ indicate conditions on the segment $i \to i+1$, and subscript i^- indicate conditions on the segment $i-1 \to i$. From equation (5.1) as well as the augmented state vector and state transition matrix, an expression for the relationship between changes in the initial and final states for the segment $i-1 \to i$ can be written in the form

$$\begin{bmatrix} \delta\overline{r}_{i^-} \\ \delta\overline{v}_{i^-} \end{bmatrix} = \begin{bmatrix} \mathbf{K}_{i,i-1} & \mathbf{L}_{i,i-1} & \mathbf{E}_{i,i-1} \\ \mathbf{M}_{i,i-1} & \mathbf{N}_{i,i-1} & \mathbf{F}_{i,i-1} \end{bmatrix} \begin{bmatrix} \delta\overline{r}_{i-1} \\ \delta\overline{v}_{i-1} \\ \delta\overline{\theta}_{i-1} \end{bmatrix} + \begin{bmatrix} \overline{v}_{i^-} \\ \overline{a}_{i^-} \end{bmatrix} (\delta t_{i^-} - \delta t_{i-1}) \,, \qquad (5.9)$$

where the three-element vectors in equation (5.9) are defined as

$$\begin{aligned} \overline{r} &= [x \quad y \quad z]^T \,, \\ \overline{v} &= [\dot{x} \quad \dot{y} \quad \dot{z}]^T \,, \\ \overline{a} &= [\ddot{x} \quad \ddot{y} \quad \ddot{z}]^T \,, \\ \overline{\theta} &= [\alpha \quad \gamma]^T \,. \end{aligned}$$

Evaluating the first vector equation in terms of $\delta\overline{v}_{i-1}$,

$$\delta\overline{v}_{i-1} = -\mathbf{L}_{i,i-1}^{-1}\mathbf{K}_{i,i-1}\delta\overline{r}_{i-1} - \mathbf{L}_{i,i-1}^{-1}\mathbf{E}_{i,i-1}\delta\overline{\theta}_{i-1}$$

$$- \mathbf{L}_{i,i-1}^{-1}\overline{v}_{i^-}(\delta t_{i^-} - \delta t_{i-1}) \; + \; \mathbf{L}_{i,i-1}^{-1}\delta\overline{r}_{i^-} \; . \tag{5.10}$$

The second vector relationship in equation (5.9) expresses $\delta\overline{v}_{i^-}$ as a function of various variational quantities, including $\delta\overline{v}_{i-1}$. Substituting equation (5.10) into the $\delta\overline{v}_{i^-}$ expression yields

$$\begin{aligned} \delta\overline{v}_{i^-} \;\; = \;\; & (\mathbf{M}_{i,i-1} - \mathbf{N}_{i,i-1}\mathbf{L}_{i,i-1}^{-1}\mathbf{K}_{i,i-1})\delta\overline{r}_{i-1} \; + \; (\mathbf{F}_{i,i-1} - \mathbf{N}_{i,i-1}\mathbf{L}_{i,i-1}^{-1}\mathbf{E}_{i,i-1})\delta\overline{\theta}_{i-1} \\ & + (\overline{a}_{i^-} - \mathbf{N}_{i,i-1}\mathbf{L}_{i,i-1}^{-1}\overline{v}_{i^-})(\delta t_{i^-} - \delta t_{i-1}) \; + \; \mathbf{N}_{i,i-1}\mathbf{L}_{i,i-1}^{-1}\delta\overline{r}_{i^-} \; . \end{aligned} \tag{5.11}$$

Similarly, for the next segment, $i \rightarrow i+1$,

$$\begin{aligned} \delta\overline{v}_{i^+} \;\; = \;\; & -\mathbf{L}_{i+1,i}^{-1}\mathbf{K}_{i+1,i}\delta\overline{r}_i \; - \; \mathbf{L}_{i+1,i}^{-1}\mathbf{E}_{i+1,i}\delta\overline{\theta}_i \\ & - \mathbf{L}_{i+1,i}^{-1}\overline{v}_{i+1}(\delta t_{i+1} - \delta t_{i^-}) \; + \; \mathbf{L}_{i+1,i}^{-1}\delta\overline{r}_{i+1} \; . \end{aligned} \tag{5.12}$$

If the position and time at point i are constrained to be the same for both segments, that is, $\overline{r}_{i^+} = \overline{r}_{i^-}$ and $t_{i^+} = t_{i^-}$, equation (5.11) can be subtracted from equation (5.12) to obtain a general expression for the variation in the velocity discontinuity at i, that is,

$$\delta\Delta\overline{v}_i = \begin{bmatrix} \mathbf{Z}_{r_{i,0}} & \mathbf{Z}_{\theta_{i,0}} & \mathbf{Z}_{t_{i,0}} & \mathbf{Z}_{r_{i,1}} & \mathbf{Z}_{\theta_{i,1}} & \mathbf{Z}_{t_{i,1}} & \mathbf{Z}_{r_{i,2}} & \mathbf{Z}_{\theta_{i,2}} & \mathbf{Z}_{t_{i,2}} \end{bmatrix} \begin{bmatrix} \delta\overline{r}_{i-1} \\ \delta\overline{\theta}_{i-1} \\ \delta t_{i-1} \\ \delta\overline{r}_i \\ \delta\overline{\theta}_i \\ \delta t_i \\ \delta\overline{r}_{i+1} \\ \delta\overline{\theta}_{i+1} \\ \delta t_{i+1} \end{bmatrix} , \tag{5.13}$$

where the $\mathbf{Z}$ submatrices are defined as

$$\begin{aligned}
\mathbf{Z}_{r_{i,0}} &= \mathbf{N}_{i,i-1}\mathbf{L}_{i,i-1}^{-1}\mathbf{K}_{i,i-1} - \mathbf{M}_{i,i-1} \ , \\
\mathbf{Z}_{\theta_{i,0}} &= \mathbf{N}_{i,i-1}\mathbf{L}_{i,i-1}^{-1}\mathbf{E}_{i,i-1} - \mathbf{F}_{i,i-1} \ , \\
\mathbf{Z}_{t_{i,0}} &= \overline{a}_{i^-} - \mathbf{N}_{i,i-1}\mathbf{L}_{i,i-1}^{-1}\overline{v}_{i^-} \ , \\
\mathbf{Z}_{r_{i,1}} &= -\mathbf{L}_{i+1,i}^{-1}\mathbf{K}_{i+1,i} - \mathbf{N}_{i,i-1}\mathbf{L}_{i,i-1}^{-1} \ , \\
\mathbf{Z}_{\theta_{i,1}} &= -\mathbf{L}_{i+1,i}^{-1}\mathbf{E}_{i+1,i} \ , \\
\mathbf{Z}_{t_{i,1}} &= \mathbf{N}_{i,i-1}\mathbf{L}_{i,i-1}^{-1}\overline{v}_{i^-} - \overline{a}_{i^-} + \mathbf{L}_{i+1,i}^{-1}\overline{v}_{i+1} \ , \\
\mathbf{Z}_{r_{i,2}} &= \mathbf{L}_{i+1,i}^{-1} \ , \\
\mathbf{Z}_{\theta_{i,2}} &= \mathbf{0} \ , \\
\mathbf{Z}_{t_{i,2}} &= -\mathbf{L}_{i+1,i}^{-1}\overline{v}_{i+1} \ .
\end{aligned}$$

Since it is generally desired to force $\Delta\overline{v}_i$ to zero, $\delta\Delta\overline{v}_i = -\Delta\overline{v}_i$.

The first target point, $i = 0$, must remain fixed on the trajectory path representing the manifold from which the transfer is initially approximated, to ensure that the spacecraft ultimately injects into the desired halo orbit. Therefore, the three elements of $\overline{r}_0$ are fixed, and the velocity discontinuity at the first target point is computed as $\Delta\overline{v}_0 = \overline{v}_0 - \overline{v}_{manifold}$. As a result, the expression for the variation in the velocity discontinuity at point 0 is written

$$\delta\Delta\overline{v}_0 = \begin{bmatrix} \mathbf{Z}_{\theta_{0,1}} & \mathbf{Z}_{t_{0,1}} & \mathbf{Z}_{r_{0,2}} & \mathbf{Z}_{\theta_{0,2}} & \mathbf{Z}_{t_{0,2}} \end{bmatrix} \begin{bmatrix} \delta\overline{\theta}_0 \\ \delta t_0 \\ \delta\overline{r}_1 \\ \delta\overline{\theta}_1 \\ \delta t_1 \end{bmatrix} \ , \tag{5.14}$$

where, in this case, the submatrices are defined as

$$\begin{aligned}
\mathbf{Z}_{\theta_{0,1}} &= -\mathbf{L}_{1,0}^{-1}\mathbf{E}_{1,0} \ , \\
\mathbf{Z}_{t_{0,1}} &= \mathbf{L}_{1,0}^{-1}\overline{v}_1 \ , \\
\mathbf{Z}_{r_{0,2}} &= \mathbf{L}_{1,0}^{-1} \ , \\
\mathbf{Z}_{\theta_{0,2}} &= \mathbf{0} \ , \\
\mathbf{Z}_{t_{0,2}} &= -\mathbf{L}_{1,0}^{-1}\overline{v}_1 \ .
\end{aligned}$$

Again, since $\delta\overline{r}_0 = 0$, the matrix $\mathbf{Z}_{r_{1,0}}$ is zero and removed from consideration. Ideally, the velocity discontinuity at point 0 converges to zero, indicating a zero-cost HOI (halo orbit insertion) and an asymptotic approach to the halo orbit.

For the purposes of this investigation, it is assumed that the transfer originates from a circular Earth parking orbit. Therefore, the nth target point, which corresponds to the origin of the transfer in the "backward" design process, is positioned at a specified altitude with respect to the Earth. Ideally, the flight path angle at the nth target point will also be zero, thereby minimizing the propellant cost for TTI (transfer trajectory insertion). These constraints can be expressed mathematically in terms of the functions

$$h = \{|\overline{r}_{2_n}| - r_{Earth}\} - h_{desired} \ , \tag{5.15}$$

$$f = \overline{r}_{2_n} \cdot \overline{v}_{2_n} \ , \tag{5.16}$$

where $\overline{r}_{2_n}$ and $\overline{v}_{2_n}$ are the position and velocity vectors of the spacecraft relative to the Earth at target point n; h is the altitude; and, the flight path angle is f. The final target state is achieved when $h = f = 0$. The first variations in these constraints are then

$$\delta h = \frac{\overline{r}_{2_n} \cdot \delta\overline{r}_n}{|\overline{r}_{2_n}|} \ , \tag{5.17}$$

$$\delta f = \overline{v}_n \cdot \delta\overline{r}_n + \overline{r}_{2_n} \cdot \delta\overline{v}_n \ , \tag{5.18}$$

where, from equation (5.11),

$$\begin{aligned} \delta\overline{v}_n = \ & (\mathbf{M}_{n,n-1} - \mathbf{N}_{n,n-1}\mathbf{L}^{-1}_{n,n-1}\mathbf{K}_{n,n-1})\delta\overline{r}_{n-1} \\ & + (\mathbf{F}_{n,n-1} - \mathbf{N}_{n,n-1}\mathbf{L}^{-1}_{n,n-1}\mathbf{E}_{n,n-1})\delta\overline{\theta}_{n-1} \\ & + (\overline{a}_n - \mathbf{N}_{n,n-1}\mathbf{L}^{-1}_{n,n-1}\overline{v}_n)(\delta t_n - \delta t_{n-1}) \ + \ \mathbf{N}_{n,n-1}\mathbf{L}^{-1}_{n,n-1}\delta\overline{r}_n \ . \end{aligned}$$

To generate the desired terminal conditions, the values of h and f must be forced to zero, thus, $\delta h = -h$ and $\delta f = -f$.

The vector equation (5.13) corresponding to each of the target points, equation (5.14) applied at the first target point, as well as the constraint equations (5.17) and

(5.18), can be combined into a single system of linear equations. For compactness, the constraint equations are rewritten as

$$\delta h = \mathbf{Z}_h \delta \overline{r}_n \ , \tag{5.19}$$

$$\begin{aligned} \delta f = {} & \mathbf{Z}_{f,r_{n-1}} \delta \overline{r}_{n-1} + \mathbf{Z}_{f,\theta_{n-1}} \delta \overline{\theta}_{n-1} + \mathbf{Z}_{f,t_{n-1}} \delta t_{n-1} \\ & + \mathbf{Z}_{f,r_n} \delta \overline{r}_n + \mathbf{Z}_{f,t_n} \delta t_n \ , \end{aligned} \tag{5.20}$$

where

$$\begin{aligned} \mathbf{Z}_h &= \frac{\overline{r}_{2_n}^T}{|\overline{r}_{2_n}|} \ , \\ \mathbf{Z}_{f,r_{n-1}} &= \overline{r}_{2_n}^T (\mathbf{M}_{n,n-1} - \mathbf{N}_{n,n-1} \mathbf{L}_{n,n-1}^{-1} \mathbf{K}_{n,n-1}) \ , \\ \mathbf{Z}_{f,\theta_{n-1}} &= \overline{r}_{2_n}^T (\mathbf{F}_{n,n-1} - \mathbf{N}_{n,n-1} \mathbf{L}_{n,n-1}^{-1} \mathbf{E}_{n,n-1}) \ , \\ \mathbf{Z}_{f,t_{n-1}} &= -\overline{r}_{2_n}^T (\overline{a}_n - \mathbf{N}_{n,n-1} \mathbf{L}_{n,n-1}^{-1} \overline{v}_n) \ , \\ \mathbf{Z}_{f,r_n} &= \overline{v}_n^T + \overline{r}_{2_n}^T \mathbf{N}_{n,n-1} \mathbf{L}_{n,n-1}^{-1} \ , \\ \mathbf{Z}_{f,t_n} &= \overline{r}_{2_n}^T (\overline{a}_n - \mathbf{N}_{n,n-1} \mathbf{L}_{n,n-1}^{-1} \overline{v}_n) \ . \end{aligned}$$

Then, the complete system of linear equations has the form

$$\mathbf{Z} \overline{\delta} = \overline{c} \ , \tag{5.21}$$

where the vectors $\overline{\delta}$ and $\overline{c}$ are written as

$$\overline{\delta} = \begin{bmatrix} \delta\overline{\theta}_0 \\ \delta t_0 \\ \delta\overline{r}_1 \\ \delta\overline{\theta}_1 \\ \delta t_1 \\ \delta\overline{r}_2 \\ \delta\overline{\theta}_2 \\ \delta t_2 \\ \vdots \\ \delta\overline{r}_n \\ \delta\overline{\theta}_n \\ \delta t_n \end{bmatrix} \ , \quad \overline{c} = \begin{bmatrix} -\Delta\overline{v}_0 \\ -\Delta\overline{v}_1 \\ -\Delta\overline{v}_2 \\ \vdots \\ -\Delta\overline{v}_{n-1} \\ -h \\ -f \end{bmatrix} \ ,$$

and the matrix $\mathbf{Z}$ has the form

$$\mathbf{Z} = \begin{bmatrix}
\mathbf{Z}_{\theta_{0,1}} & \mathbf{Z}_{t_{0,1}} & \mathbf{Z}_{r_{0,2}} & \mathbf{Z}_{\theta_{0,2}} & \mathbf{Z}_{t_{0,2}} & \mathbf{0} & \mathbf{0} & \mathbf{0} & \cdots & \mathbf{0} \\
\mathbf{Z}_{\theta_{1,0}} & \mathbf{Z}_{t_{1,0}} & \mathbf{Z}_{r_{1,1}} & \mathbf{Z}_{\theta_{1,1}} & \mathbf{Z}_{t_{1,1}} & \mathbf{Z}_{r_{1,2}} & \mathbf{Z}_{\theta_{1,2}} & \mathbf{Z}_{t_{1,2}} & \cdots & \mathbf{0} \\
\mathbf{0} & \mathbf{0} & \mathbf{Z}_{r_{2,0}} & \mathbf{Z}_{\theta_{2,0}} & \mathbf{Z}_{t_{2,0}} & \mathbf{Z}_{r_{2,1}} & \mathbf{Z}_{\theta_{2,1}} & \mathbf{Z}_{t_{2,1}} & \cdots & \mathbf{0} \\
\mathbf{0} & \mathbf{0} & \mathbf{0} & \mathbf{0} & \mathbf{0} & \mathbf{Z}_{r_{3,0}} & \mathbf{Z}_{\theta_{3,0}} & \mathbf{Z}_{t_{3,0}} & \cdots & \mathbf{0} \\
 & \cdot & & & & & & \cdot & & \\
 & & \cdot & & & & & & \cdot & \\
 & & & \cdot & & & & & & \cdot \\
0 \cdots & \mathbf{Z}_{r_{n-1,0}} & \mathbf{Z}_{\theta_{n-1,0}} & \mathbf{Z}_{t_{n-1,0}} & \mathbf{Z}_{r_{n-1,1}} & \mathbf{Z}_{\theta_{n-1,1}} & \mathbf{Z}_{t_{n-1,1}} & \mathbf{Z}_{r_{n-1,2}} & \mathbf{Z}_{\theta_{n-1,2}} & \mathbf{Z}_{t_{n-1,2}} \\
0 \cdots & \mathbf{0} & \mathbf{0} & \mathbf{0} & \mathbf{0} & \mathbf{0} & \mathbf{0} & \mathbf{Z}_h & \mathbf{0} & \mathbf{0} \\
0 \cdots & \mathbf{0} & \mathbf{0} & \mathbf{0} & \mathbf{Z}_{f,r_{n-1}} & \mathbf{Z}_{f,\theta_{n-1}} & \mathbf{Z}_{f,t_{n-1}} & \mathbf{Z}_{f,r_n} & \mathbf{0} & \mathbf{Z}_{f,t_n}
\end{bmatrix}.$$

Assuming $n \geq 2$, matrix $\mathbf{Z}$ is of dimension $(3n+2) \times (6n+3)$, $\overline{\delta}$ is a column vector of length $(6n+3)$, and $\overline{c}$ is a column vector of length $(3n+2)$. The minimum norm solution to the system in equation (5.21) is

$$\overline{\delta} = -\mathbf{Z}^T(\mathbf{Z}\mathbf{Z}^T)^{-1}\overline{c}\,. \tag{5.22}$$

With these updated positions, orientations, and time intervals, the first level of the iterative process is reapplied to generate a modified, but continuous, trajectory, one with reduced velocity discontinuities and a terminal point closer to the desired altitude. This trajectory is then subjected to the second level corrections process again, to further reduce any velocity discontinuities. The process is repeated until a trajectory is generated that is continuous in position and terminates at the desired altitude; the velocity discontinuities are reduced as far as possible.

5.2.4 Preliminary Results

The transfer generation algorithm is implemented as described previously. Trajectories are computed for various numbers of target points ranging between 5 and 30, and using several different manifolds as starting points. To be defined as continuous in position, the maximum allowable deviation from a target point location (i.e., position discontinuity) is 15m; this target is always achieved before the process continues.

The transfer algorithm is generally successful at introducing sail orientation changes to bring the terminal point of the trajectory nearer to the Earth. An example of a transfer generated using 15 target points appears in Figure 5.5. The corresponding time history of the sail orientation angles appears in Figure 5.6, however, note that velocity discontinuities remain at each target point (maneuvers along are numbered in the reverse order of the target points due to the "backwards" design process). (See Table 5.1.) Difficulties with the algorithm do exist, and successful targeting to low Earth altitudes is not yet resolved. Perhaps more target points or simply better placement of the target points is critical, or the development of an alternative corrector is necessary. Nevertheless, the transfer generation algorithm, while not completely successful, appears to have potential, and merits further investigation.

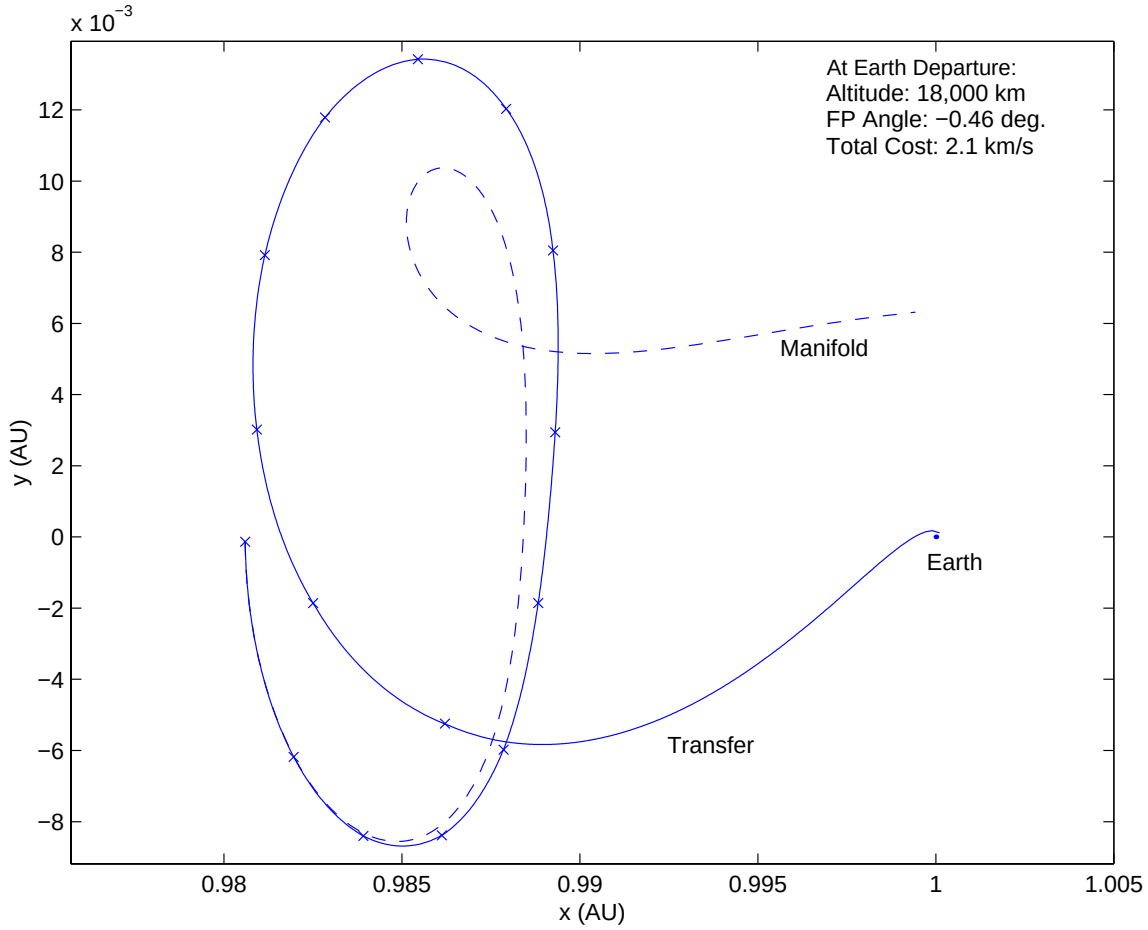

Figure 5.5. Example: transfer to a Sun-Earth L_1 halo (β=0.035)

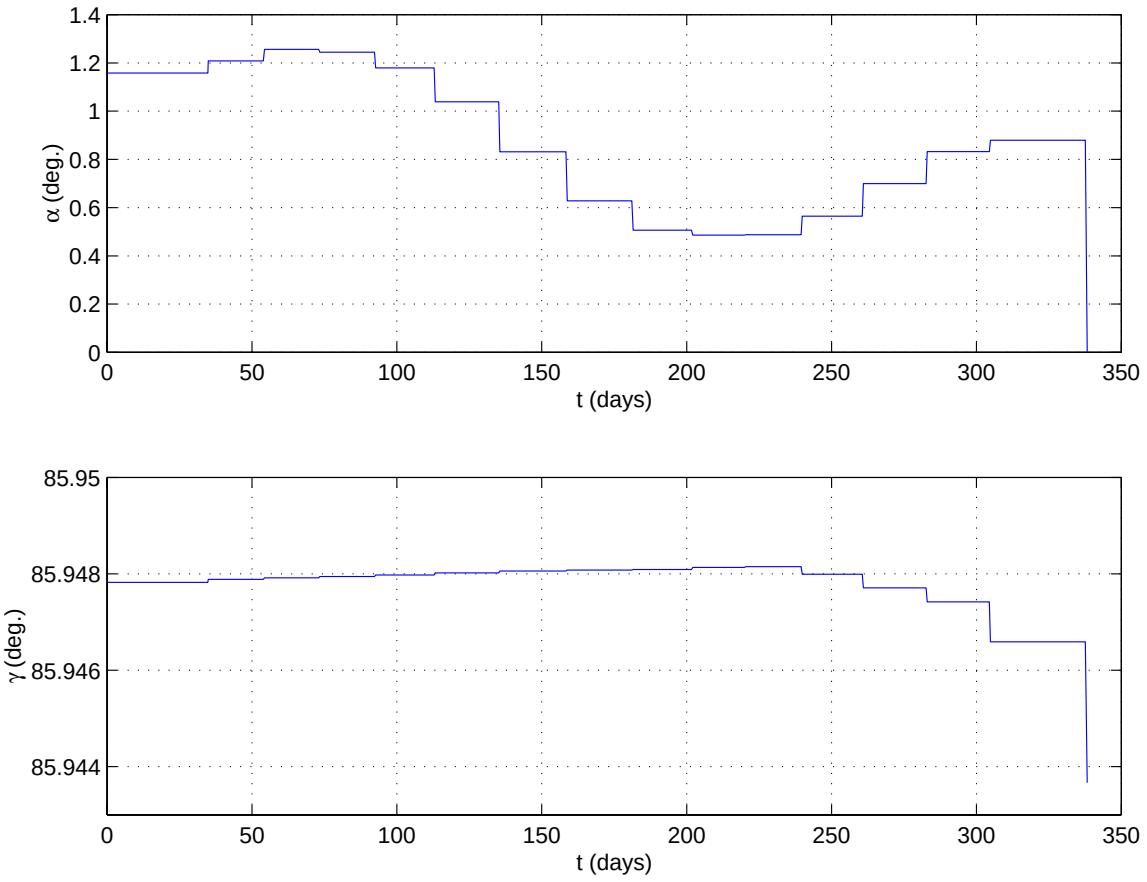

Figure 5.6. Variation in sail orientation angles along the example transfer path

Table 5.1. Δv time history

Transfer Δv's		
Maneuver No.	Elapsed Time (days)	Δv (m/s)
0 (TTI)	0	1890.00
1	34.85	24.96
2	54.30	19.71
3	73.37	20.55
4	92.62	18.89
5	113.21	14.10
6	135.55	4.26
7	158.79	8.74
8	181.54	18.73
9	202.09	21.91
10	220.30	21.31
11	239.84	20.17
12	260.99	15.14
13	283.01	7.41
14	304.84	1.47
15 (HOI)	338.26	0.00

6. Conclusions

6.1 Summary

The addition of a solar sail force to the dynamical model represented in the circular restricted three-body problem enables the generation of a set of "artificial" libration points. These new libration points are parameterized by the sail lightness, and the orientation of the sail relative to the solar radiation. The on-axis libration points are a subset from the total array of artificial points that are available; the on-axis set consists of those libration points that lie along the Sun-Earth line. The collinear libration points of the classical restricted three-body system, of course, serve as a basis for this subset of artificial points. The on-axis libration points retain many of the characteristics of the collinear points from which they originate. The similarity between the on-axis equilibrium points that exist due to the added solar sail force and the classical collinear libration points allows the construction of an analytical approximation for periodic orbits in the vicinity of the new libration points. This approximation is a valuable aid in identifying new families of periodic halo orbits that incorporate a solar sail force, and that differ in shape from the classical halo families.

Variations in the sail orientation can be used to control the spacecraft trajectory. This fact enables a solar sail to be used as a stationkeeping device for maintaining on-axis halo orbits. Additionally, sail orientation control allows the creation of either asymptotically stable artificial libration points that exist off the Sun-Earth line, or trajectories that remain bounded in the vicinity of such an artificial libration point. Changes in sail orientation also appear promising in the generation of transfers to and from the halo orbits.

6.2 Recommendations

There are as yet many unanswered questions concerning the use of solar sails in the three-body problem. A more in depth study of the on-axis halo families could resolve the lingering numerical issues, and begin an exploration of the other new families accessible through the bifurcation points present in the halo families. On-axis trajectories that are not periodic, but remain bounded, i.e. quasi-periodic, as well as trajectories involving periodic variations in sail orientation also suggest new directions for research.

The stationkeeping strategy that is developed in this work can be refined by determining the optimum number of target points, the best practical minimum time between maneuvers, and the appropriate length for each of the time intervals between target points. It is also worthwhile to investigate the use of a variable sail lightness parameter as a control variable, or, more likely, hybrid stationkeeping schemes using both a sail and impulsive maneuvers.

The dynamics in the vicinity of the off-axis libration points clearly require much more study. The control algorithm developed here is a simplistic proof of concept. The application of optimal control theory and nonlinear controllers would undoubtedly lead to improved trajectory design capabilities.

Finally, the transfer generation algorithm outlined in Chapter 5 is not fully functional, but shows much promise. Further analysis of this approach is warranted; it might be further developed to generate initial guesses for more sophisticated optimization schemes. Determination of the optimal number and placement of the target points would improve the performance of the transfer generation algorithm. The application of alternate correctors and different constraints could also lead to further performance improvements. Additionally, allowing the sail orientation angles to vary along each segment (e.g., parameterizing the angles as function of time and iteratively correcting the parameterization coefficients) would increase the versatility of the algorithm. Determination of the time along the transfer trajectory at which the sail should be deployed would make the transfer more representative of a practical

transfer scenario.

6.3 Concluding Remarks

Solar sails offer many new trajectory options for mission designers. In the context of multiple gravitational fields, solar sails allow the extension of existing operational techniques into regions of space not previously amenable to such methods. However, there are many practical issues to be overcome, before such missions can be successfully carried out. New mission design strategies must be developed, and numerous mechanical issues, such as those related to the construction, deployment, and control of sail structures, must be resolved. This study has sought to explore various techniques that may be useful in designing future solar sail missions. However, there are many facets to this problem, and many avenues of investigation remain open.

LIST OF REFERENCES

LIST OF REFERENCES

[1] C.R. McInnes, *Solar Sailing : Technology, Dynamics and Mission Applications*, Springer-Praxis, Chichester, United Kingdom, 1999.

[2] R.W. Farquhar, D.P. Muhonen, C.R. Newman, and H.S. Heuberger, "Trajectories and Orbital Maneuvers for the First Libration-Point Satellite," *Journal of Guidance and Control*, Vol. 3, pp. 549–554, November-December 1980.

[3] P.J. Sharer, D.W. Dunham, S. Jen, C.E. Roberts, A.W. Seacord II, and D.C. Folta, "Double Lunar Swingby and Lissajous Trajectory Design for the WIND Mission," IAF Paper 92-0065, 43rd International Astronautical Congress, Washington D.C., August 28-September 5, 1992.

[4] K.C. Howell, B.T. Barden, R.S. Wilson, and M.W. Lo, "Trajectory Design Using a Dynamical Systems Approach With Applications to Genesis," in *AAS/AIAA Astrodynamics 1997, Advances in the Astronautical Sciences* (F. Hoots, B. Kaufman, P. Cefola, and D. Spencer, eds.), Vol. 97, Part II, pp. 1665–1684, 1997.

[5] M. Beckman and J. Guzman, "Triana Mission Design," AAS Paper 99-400, AAS/AIAA Astrodynamics Specialists Conference, Girdwood, Arkansas, August 1999.

[6] V.G. Szebehely, *Theory of Orbits : The Restricted Problem of Three Bodies*, Academic Press, New York, 1967.

[7] J.V. Breakwell and J.V. Brown, "The 'Halo' Family of 3-Dimensional Periodic Orbits in the Earth-Moon Restricted Three Body Problem," *Celestial Mechanics*, Vol. 20, pp. 389–404, 1979.

[8] R.W. Farquhar and A.A. Kamel, "Quasi-Periodic Orbits About the Translunar Libration Point," *Celestial Mechanics*, Vol. 7, pp. 458–473, 1973.

[9] M.L. Finson and R.F. Probstein, "A Theory of Dust Comets. I - Model and Equations," *Astrophysical Journal*, Vol. 154, pp. 327–352, October 1968.

[10] K. Aksnes, "Short-Period and Long-Period Perturbations of a Spherical Satellite Due to Direct Solar Radiation," *Celestial Mechanics*, Vol. 13, No. 1, pp. 89–91, 1976.

[11] J.D. DeGumbia and Y.K.J. Tsui, "Solar Torque Compensation Determination System for the GOES I-M Series Weather Satellites," in *AAS/GSFC 13th International Symposium on Space Flight Dynamics*, Vol. 2, pp. 887–898, May 1998.

[12] N.A. Eismont, V.V. Khrapchenkov, P. Triska, V. Truhlik, and J. Chum, "Attitude Determination and Control in INTERBALL Project," in *AAS/GSFC 13th International Symposium on Space Flight Dynamics*, Vol. 2, pp. 983–995, May 1998.

[13] V.I. Arnold, V.V. Kozlov, and A.I. Neishtadt, *Mathematical Aspects of Classical and Celestial Mechanics*, Springer-Verlag, Berlin, 2nd ed., 1993.

[14] V.G. Szebehely and H. Mark, *Adventures in Celestial Mechanics*, Wiley-Interscience, New York, 2nd ed., 1997.

[15] H.C. Plummer, "On Oscillating Satellites - 1," *Monthly Notices of the Royal Astronomical Society*, Vol. 63, No. 8, pp. 436–443, 1903.

[16] R.W. Farquhar, *The Control and Use of Libration-Point Satellites*, Ph.D. Dissertation, Department of Aeronautics and Astronautics, Stanford University, Stanford, California, July 1968.

[17] D.L. Richardson and N.D. Cary, "A Uniformly Valid Solution for Motion About the Interior Libration Point of the Perturbed Elliptic-Restricted Problem," AAS Paper 75-021, AIAA/AAS Astrodynamics Specialists Conference, Nassau, Bahamas, July 28-30, 1975.

[18] D.L. Richardson, "Analytic Construction of Periodic Orbits About the Collinear Points," *Celestial Mechanics*, Vol. 22, pp. 241–253, 1980.

[19] K.C. Howell and J.V. Breakwell, "Almost Rectilinear Halo Orbits," *Celestial Mechanics*, Vol. 32, pp. 29–52, 1984.

[20] K.C. Howell, *Three-Dimensional, Periodic 'Halo' Orbits in the Restricted Three-Body Problem*, Ph.D. Dissertation, Department of Aeronautics and Astronautics, Stanford University, Stanford, California, March 1983.

[21] K.C. Howell, "Three-Dimensional, Periodic 'Halo' Orbits," *Celestial Mechanics*, Vol. 32, pp. 53–71, 1984.

[22] K.C. Howell and H.J. Pernicka, "Numerical Determination of Lissajous Trajectories in the Restricted Three-Body Problem," *Celestial Mechanics*, Vol. 41, pp. 107–124, 1988.

[23] K.C. Howell and H.J. Pernicka, "Stationkeeping Method for Libration Point Trajectories," *Journal of Guidance, Control, and Dynamics*, Vol. 16, No. 1, pp. 151–159, 1993.

[24] K.C. Howell, B.T. Barden, and M.W. Lo, "Application of Dynamical Systems Theory to Trajectory Design for a Libration Point Mission," *Journal of the Astronautical Sciences*, Vol. 45, pp. 161–178, April-June 1997.

[25] K.C. Howell and S.C. Gordon, "Orbit Determination Error Analysis and a Station-Keeping Strategy for Sun-Earth L_1 Libration Point Orbits," *Journal of the Astronautical Sciences*, Vol. 42, pp. 207–228, April-June 1994.

[26] C.R. McInnes and J.F.L. Simmons, "Solar Sail Halo Orbits I: Heliocentric Case," *Journal of Spacecraft and Rockets*, Vol. 29, No. 4, pp. 466–471, 1992.

[27] C. Wiley, "Clipper Ships of Space," in *Astounding Science Fiction*, p. 135, May 1951.

[28] R.L. Garwin, "Solar Sailing - A Practical Method of Propulsion Within the Solar System," *Jet Propulsion*, No. 28, pp. 188–190, 1958.

[29] T.C. Tsu, "Interplanetary Travel by Solar Sail," *Journal of the American Rocket Society*, Vol. 29, No. 6, pp. 422–427, 1959.

[30] R.L. Sohn, "Attitude Stabilization by Means of Solar Radiation Pressure," *Journal of the American Rocket Society*, Vol. 29, No. 5, pp. 371–373, 1959.

[31] R.L. Forward, "Statite: A Spacecraft That Does Not Orbit," *Journal of Spacecraft and Rockets*, Vol. 28, No. 5, pp. 606–611, 1991.

[32] C.R. McInnes and J.F.L. Simmons, "Solar Sail Halo Orbits II: Geocentric Case," *Journal of Spacecraft and Rockets*, Vol. 29, No. 4, pp. 472–479, 1992.

[33] C.R. McInnes, "Solar Sail Mission Applications for Non-Keplerian Orbits," *Acta Astronautica*, Vol. 45, No. 4-9, pp. 567–575, 1999.

[34] C.R. McInnes, A.J.C. McDonald, J.F.L. Simmons, and E.W. MacDonald, "Solar Sail Parking in the Restricted Three-Body Problem," *Journal of Guidance, Control, and Dynamics*, Vol. 17, No. 2, pp. 399–406, 1994.

[35] C.R. McInnes, "Passive Control of Displaced Solar Sail Orbits," *Journal of Guidance, Control, and Dynamics*, Vol. 21, No. 6, pp. 975–982, 1998.

[36] C.R. McInnes and J.C. Brown, "The Dynamics of Solar Sails with a Non-Point Source of Radiation Pressure," *Celestial Mechanics and Dynamical Astronomy*, Vol. 9, pp. 249–264, 1990.

[37] J.L. Bell, "The Impact of Solar Radiation Pressure on Sun-Earth L1 Libration Point Orbits," M.S. Thesis, School of Aeronautics and Astronautics, Purdue University, West Lafayette, Indiana, August 1991.

[38] J.S. Nuss, "The Use of Solar Sails in the Circular Restricted Problem of Three Bodies," M.S. Thesis, School of Aeronautics and Astronautics, Purdue University, West Lafayette, Indiana, May 1998.

[39] L. Perko, *Differential Equations and Dynamical Systems*, Springer, New York, 2nd ed., 1996.

[40] D.L. Richardson, "A Note on a Lagrangian Formulation for Motion About the Collinear Points," *Celestial Mechanics*, Vol. 22, pp. 231–236, 1980.

[41] G. Rodriguez, E.L. Marsh, and S.M. Gunter, "Solar Sail Attitude Dynamics and Control," in *Dynamics and Control of Large Flexible Spacecraft* (L. Meirovitch, ed.), pp. 287–302, Virginia Polytechnic Institute and State University, June 13-15, 1977.

[42] E. Kreyszig, *Advanced Engineering Mathematics*, John Wiley and Sons, New York, 7th ed., 1993.

[43] K.T. Alligood, T.D. Sauer, and J.A. Yorke, *Chaos: An Introduction to Dynamical Systems*, Springer-Verlag, New York, 1997.

[44] G. Gómez, K. Howell, J. Masdemont, and C. Simó, "Station-keeping Strategies for Translunar Libration Point Orbits," AAS Paper 98-168, AAS/AIAA Space Flight Mechanics Meeting, Monterey, California, February 1998.

[45] B.N. Agrawal, *Design of Geosynchronous Spacecraft*, Prentice-Hall, Englewood Cliffs, New Jersey, 1986.

[46] M.J. Sidi, *Spacecraft Dynamics and Control: A Practical Engineering Approach*, Cambridge University Press, Cambridge, 1997.

[47] J. Mościński and Z. Ogonowski, *Advanced Control with Matlab and Simulink*, Ellis Horwood Ltd., London, 1995.

[48] B.T. Barden, "Using Stable Manifolds to Generate Transfers in the Circular Restricted Problem of Three Bodies," M.S. Thesis, Purdue University, West Lafayette, Indiana, December 1994.

APPENDICES

APPENDICES

Appendix A: Second Partial Derivatives of the Three-Body Pseudo-Potential

The following are general expressions for the second partial derivatives of U, the pseudo-potential. Each derivative is denoted as $U_{jk} = \frac{\partial U}{\partial_j \partial k}$, where $j, k \in (x, y, z)$.

$$U_{xx} = 1 - \frac{(1-\mu)}{r_1^3} - \frac{\mu}{r_2^3} + \frac{3(1-\mu)(x+\mu)^2}{r_1^5} + \frac{3\mu(x-(1-\mu))^2}{r_2^5}, \quad \text{(A.1)}$$

$$U_{xy} = \frac{3(1-\mu)(x+\mu)y}{r_1^5} + \frac{3\mu(x-(1-\mu))y}{r_2^5}, \quad \text{(A.2)}$$

$$U_{xz} = \frac{3(1-\mu)(x+\mu)z}{r_1^5} + \frac{3\mu(x-(1-\mu))z}{r_2^5}, \quad \text{(A.3)}$$

$$U_{yx} = \frac{3(1-\mu)(x+\mu)y}{r_1^5} + \frac{3\mu(x-(1-\mu))y}{r_2^5}, \quad \text{(A.4)}$$

$$U_{yy} = 1 - \frac{(1-\mu)}{r_1^3} - \frac{\mu}{r_2^3} + \frac{3(1-\mu)y^2}{r_1^5} + \frac{3\mu y^2}{r_2^5}, \quad \text{(A.5)}$$

$$U_{yz} = \frac{3(1-\mu)yz}{r_1^5} + \frac{3\mu yz}{r_2^5}, \quad \text{(A.6)}$$

$$U_{zx} = \frac{3(1-\mu)(x+\mu)z}{r_1^5} + \frac{3\mu(x-(1-\mu))z}{r_2^5}, \quad \text{(A.7)}$$

$$U_{zy} = \frac{3(1-\mu)yz}{r_1^5} + \frac{3\mu yz}{r_2^5}, \quad \text{(A.8)}$$

$$U_{zz} = -\frac{(1-\mu)}{r_1^3} - \frac{\mu}{r_2^3} + \frac{3(1-\mu)z^2}{r_1^5} + \frac{3\mu z^2}{r_2^5}. \quad \text{(A.9)}$$

Appendix B: Coefficients for the Third-Order Analytical Approximation

These equations appear in Richardson [18]. The c_n quantities in the expressions represent coefficients in a Legendre polynomial expansion of the Lagrangian, as outlined in the papers by Richardson [18, 40].

$$a_{21} = \frac{3c_3(k^2-2)}{4(1+2c_2)} , \tag{B.1}$$

$$a_{22} = \frac{3c_3}{4(1+2c_2)} , \tag{B.2}$$

$$a_{23} = -\frac{3c_3\lambda}{4kd_1}\left[3k^3\lambda - 6k(k-\lambda) + 4\right] , \tag{B.3}$$

$$a_{24} = -\frac{3c_3\lambda}{4kd_1}\left[2 + 3k\lambda\right] , \tag{B.4}$$

$$\begin{aligned} a_{31} &= -\frac{9\lambda}{4d_2}\left[4c_3(ka_{23} - b_{21}) + kc_4(4+k^2)\right] \\ &\quad + \frac{(9\lambda^2 + 1 - c_2)}{2d_2}\left[3c_3(2a_{23} - kb_{21}) + c_4(2+3k^2)\right] , \end{aligned} \tag{B.5}$$

$$\begin{aligned} a_{32} &= -\frac{9\lambda}{4d_2}\left[4c_3(ka_{24} - b_{22}) + kc_4\right] \\ &\quad - \frac{3(9\lambda^2 + 1 - c_2)}{2d_2}\left[c_3(kb_{22} + d_{21} - 2a_{24}) - c_4\right] , \end{aligned} \tag{B.6}$$

$$b_{21} = -\frac{3c_3\lambda}{2d_1}(3k\lambda - 4) , \tag{B.7}$$

$$b_{22} = \frac{3c_3\lambda}{d_1} , \tag{B.8}$$

$$\begin{aligned} b_{31} &= \frac{3\lambda}{d_2}\left[3c_3(kb_{21} - 2a_{23}) - c_4(2+3k^2)\right] \\ &\quad + \frac{3(9\lambda^2 + 1 + 2c_2)}{8d_2}\left[4c_3(ka_{23} - b_{21}) + kc_4(4+k^2)\right] , \end{aligned} \tag{B.9}$$

$$\begin{aligned} b_{32} &= \frac{9\lambda}{d_2}\left[c_3(kb_{22} + d_{21} - 2a_{24}) - c_4\right] \\ &\quad + \frac{3(9\lambda^2 + 1 + 2c_2)}{8d_2}\left[4c_3(ka_{24} - b_{22}) + kc_4\right] , \end{aligned} \tag{B.10}$$

$$d_{21} = -\frac{c_3}{2\lambda^2} , \tag{B.11}$$

$$d_{31} = \frac{3}{64\lambda^2}\left[4c_3a_{24} + c_4)\right] , \tag{B.12}$$

$$d_{32} = \frac{3}{64\lambda^2}\left[4c_3(a_{23} - d_{21}) + c_4(4+k^2))\right] , \tag{B.13}$$

where

$$d_1 = \frac{3\lambda^2}{k}\left[k(6\lambda^2-1)-2\lambda\right] , \tag{B.14}$$

$$d_2 = \frac{8\lambda^2}{k}\left[k(11\lambda^2-1)-2\lambda\right] , \tag{B.15}$$

$$k = \frac{1}{2\lambda}(\lambda^2+1+2c_2) , \tag{B.16}$$

and the linearized frequency λ is the solution to the following equation:

$$\lambda^4+(c_2-2)\lambda^2-(c_2-1)(1+2c_2)=0 . \tag{B.17}$$

For the amplitude constraint relationship,

$$l_1 = 2\lambda^2 s_1-\frac{3}{2}c_3(2a_{21}+a_{23}+5d_{21})-\frac{3}{8}c_4(12-k^2) , \tag{B.18}$$

$$l_2 = 2\lambda^2 s_2+\frac{3}{2}c_3(a_{24}-2a_{22})+\frac{9}{8}c_4 , \tag{B.19}$$

$$\Delta = \lambda^2-c_2 , \tag{B.20}$$

where,

$$s_1 = \frac{\frac{3}{2}c_3[2a_{21}(k^2-2)-a_{23}(k^2+2)-2kb_{21}]-\frac{3}{8}c_4[3k^4-8k^2+8]}{2\lambda[\lambda(1+k^2)-2k]} , \tag{B.21}$$

$$s_2 = \frac{\frac{3}{2}c_3[2a_{22}(k^2-2)+a_{24}(k^2+2)+2kb_{22}+5d_{21}]+\frac{3}{8}c_4[12-k^2]}{2\lambda[\lambda(1+k^2)-2k]} . \tag{B.22}$$

Appendix C: Second Partial Derivatives of the On-Axis "Modified Pseudo-Potential"

The expressions below represent the second partial derivatives of Ω, the "modified pseudo-potential" that incorporates the effects of a solar sail with $\alpha = 0°$.. The notation is $\Omega_{jk} = \frac{\partial \Omega}{\partial_j \partial k}$, where $j, k \in (x, y, z)$.

$$\Omega_{xx} = 1 - \frac{(1-\mu)(1-\beta)}{r_1^3} - \frac{\mu}{r_2^3} + \frac{3(1-\mu)(1-\beta)(x+\mu)^2}{r_1^5} + \frac{3\mu(x-(1-\mu))^2}{r_2^5}, \tag{C.1}$$

$$\Omega_{xy} = \frac{3(1-\mu)(1-\beta)(x+\mu)y}{r_1^5} + \frac{3\mu(x-(1-\mu))y}{r_2^5}, \tag{C.2}$$

$$\Omega_{xz} = \frac{3(1-\mu)(1-\beta)(x+\mu)z}{r_1^5} + \frac{3\mu(x-(1-\mu))z}{r_2^5}, \tag{C.3}$$

$$\Omega_{yx} = \frac{3(1-\mu)(1-\beta)(x+\mu)y}{r_1^5} + \frac{3\mu(x-(1-\mu))y}{r_2^5}, \tag{C.4}$$

$$\Omega_{yy} = 1 - \frac{(1-\mu)(1-\beta)}{r_1^3} - \frac{\mu}{r_2^3} + \frac{3(1-\mu)(1-\beta)y^2}{r_1^5} + \frac{3\mu y^2}{r_2^5}, \tag{C.5}$$

$$\Omega_{yz} = \frac{3(1-\mu)(1-\beta)yz}{r_1^5} + \frac{3\mu yz}{r_2^5}, \tag{C.6}$$

$$\Omega_{zx} = \frac{3(1-\mu)(1-\beta)(x+\mu)z}{r_1^5} + \frac{3\mu(x-(1-\mu))z}{r_2^5}, \tag{C.7}$$

$$\Omega_{zy} = \frac{3(1-\mu)(1-\beta)yz}{r_1^5} + \frac{3\mu yz}{r_2^5}, \tag{C.8}$$

$$\Omega_{zz} = -\frac{(1-\mu)(1-\beta)}{r_1^3} - \frac{\mu}{r_2^3} + \frac{3(1-\mu)(1-\beta)z^2}{r_1^5} + \frac{3\mu z^2}{r_2^5}. \tag{C.9}$$

Appendix D: Partial Derivatives of the Solar Sail Acceleration Terms Relative to Position

The expressions below are the partial derivatives of the scalar solar sail acceleration components with respect to the sail position coordinates. The notation is consistent, $a_{jk} = \frac{\partial a_j}{\partial k}$, where $j, k \in (x, y, z)$. It is assumed that the sail cone and clock angles, α and γ, are independent of position.

$$a_{xx} = \frac{\beta(1-\mu)\cos^2\alpha}{r_1^2}\left\{-\frac{2(x+\mu)n_x}{r_1^2} + \frac{\cos\alpha(y^2+z^2)}{r_1^3} - \frac{\sin\alpha\sin\gamma\ y(x+\mu)}{|\overline{r}_1\times\hat{z}|^3} + \frac{\sin\alpha\cos\gamma\ z((x+\mu)^4 - y^2z^2 - y^4)}{|(\overline{r}_1\times\hat{z})\times\overline{r}_1|^3}\right\}, \quad \text{(D.1)}$$

$$a_{xy} = \frac{\beta(1-\mu)\cos^2\alpha}{r_1^2}\left\{-\frac{2y\ n_x}{r_1^2} - \frac{\cos\alpha(x+\mu)y}{r_1^3} + \frac{\sin\alpha\sin\gamma\ (x+\mu)^2}{|\overline{r}_1\times\hat{z}|^3} + \frac{\sin\alpha\cos\gamma\ (x+\mu)yz(2(x+\mu)^2+2y^2+z^2)}{|(\overline{r}_1\times\hat{z})\times\overline{r}_1|^3}\right\}, \quad \text{(D.2)}$$

$$a_{xz} = \frac{\beta(1-\mu)\cos^2\alpha}{r_1^2}\left\{-\frac{2z\ n_x}{r_1^2} - \frac{\cos\alpha(x+\mu)z}{r_1^3} - \frac{\sin\alpha\cos\gamma\ (x+\mu)((x+\mu)^2+y^2)^2}{|(\overline{r}_1\times\hat{z})\times\overline{r}_1|^3}\right\}, \quad \text{(D.3)}$$

$$a_{yx} = \frac{\beta(1-\mu)\cos^2\alpha}{r_1^2}\left\{-\frac{2(x+\mu)n_y}{r_1^2} - \frac{\cos\alpha(x+\mu)y}{r_1^3} - \frac{\sin\alpha\sin\gamma\ y^2}{|\overline{r}_1\times\hat{z}|^3} + \frac{\sin\alpha\cos\gamma\ (x+\mu)yz(2(x+\mu)^2+2y^2+z^2)}{|(\overline{r}_1\times\hat{z})\times\overline{r}_1|^3}\right\}, \quad \text{(D.4)}$$

$$a_{yy} = \frac{\beta(1-\mu)\cos^2\alpha}{r_1^2}\left\{-\frac{2y\ n_y}{r_1^2} + \frac{\cos\alpha((x+\mu)^2+z^2)}{r_1^3} + \frac{\sin\alpha\sin\gamma\ y^2}{|\overline{r}_1\times\hat{z}|^3} - \frac{\sin\alpha\cos\gamma\ z((x+\mu)^2(z^2+(x+\mu)^2) - y^4)}{|(\overline{r}_1\times\hat{z})\times\overline{r}_1|^3}\right\}, \quad \text{(D.5)}$$

$$a_{yz} = \frac{\beta(1-\mu)\cos^2\alpha}{r_1^2}\left\{-\frac{2z\ n_y}{r_1^2} - \frac{\cos\alpha\ zy}{r_1^3}\right.$$

$$- \frac{\sin\alpha\cos\gamma\ y((x+\mu)^2+y^2)^2}{|(\overline{r}_1\times\hat{z})\times\overline{r}_1|^3}\Bigg\}\ , \tag{D.6}$$

$$\begin{aligned} a_{zx} &= \frac{\beta(1-\mu)\cos^2\alpha}{r_1^2}\Bigg\{-\frac{2(x+\mu)n_z}{r_1^2}\ -\ \frac{\cos\alpha(x+\mu)z}{r_1^3} \\ &\quad + \frac{\sin\alpha\cos\gamma\ (x+\mu)z^2((x+\mu)^2+y^2)}{|(\overline{r}_1\times\hat{z})\times\overline{r}_1|^3}\Bigg\}\ , \end{aligned} \tag{D.7}$$

$$\begin{aligned} a_{zy} &= \frac{\beta(1-\mu)\cos^2\alpha}{r_1^2}\Bigg\{-\frac{2y\ n_z}{r_1^2}\ -\ \frac{\cos\alpha\ yz}{r_1^3} \\ &\quad + \frac{\sin\alpha\cos\gamma\ yz^2((x+\mu)^2+y^2)}{|(\overline{r}_1\times\hat{z})\times\overline{r}_1|^3}\Bigg\}\ , \end{aligned} \tag{D.8}$$

$$\begin{aligned} a_{zz} &= \frac{\beta(1-\mu)\cos^2\alpha}{r_1^2}\Bigg\{-\frac{2z\ n_z}{r_1^2}\ +\ \frac{\cos\alpha\ ((x+\mu)^2+y^2)}{r_1^3} \\ &\quad - \frac{\sin\alpha\cos\gamma\ z((x+\mu)^2+y^2)^2}{|(\overline{r}_1\times\hat{z})\times\overline{r}_1|^3}\Bigg\}\ . \end{aligned} \tag{D.9}$$

Appendix E: Partial Derivatives of the Solar Sail Acceleration Terms Relative to Orientation

The expressions below represent the partial derivatives of the scalar solar sail acceleration components with respect to the sail orientation angles. The partials are denoted such that $a_{jk} = \frac{\partial a_j}{\partial k}$, where $j \in (x, y, z)$, and $k \in (\alpha, \gamma)$.

$$a_{x\alpha} = \frac{\beta(1-\mu)\cos\alpha}{r_1^2}\left\{-\frac{3\cos\alpha\ \sin\alpha(x+\mu)}{r_1^2} + \frac{(1-3\sin^2\alpha)\sin\gamma\ y}{|\overline{r}_1 \times \hat{z}|^3} - \frac{(1-3\sin^2\alpha)\cos\gamma\ (x+\mu)z}{|(\overline{r}_1 \times \hat{z}) \times \overline{r}_1|^3}\right\}, \tag{E.1}$$

$$a_{y\alpha} = \frac{\beta(1-\mu)\cos\alpha}{r_1^2}\left\{-\frac{3\cos\alpha\ \sin\alpha\ y}{r_1^2} - \frac{(1-3\sin^2\alpha)\sin\gamma\ (x+\mu)}{|\overline{r}_1 \times \hat{z}|^3} - \frac{(1-3\sin^2\alpha)\cos\gamma\ yz}{|(\overline{r}_1 \times \hat{z}) \times \overline{r}_1|^3}\right\}, \tag{E.2}$$

$$a_{z\alpha} = \frac{\beta(1-\mu)\cos\alpha}{r_1^2}\left\{-\frac{3\cos\alpha\ \sin\alpha\ z}{r_1^2} + \frac{(1-3\sin^2\alpha)\cos\gamma(y^2+(x+\mu)^2)}{|(\overline{r}_1 \times \hat{z}) \times \overline{r}_1|^3}\right\}, \tag{E.3}$$

$$a_{x\gamma} = \frac{\beta(1-\mu)\cos^2\alpha}{r_1^2}\left\{\frac{\sin\alpha\cos\gamma\ y}{|\overline{r}_1 \times \hat{z}|^3} + \frac{\sin\alpha\sin\gamma\ (x+\mu)z}{|(\overline{r}_1 \times \hat{z}) \times \overline{r}_1|^3}\right\}, \tag{E.4}$$

$$a_{y\gamma} = \frac{\beta(1-\mu)\cos^2\alpha}{r_1^2}\left\{-\frac{\sin\alpha\cos\gamma\ (x+\mu)}{|\overline{r}_1 \times \hat{z}|^3} + \frac{\sin\alpha\sin\gamma\ yz}{|(\overline{r}_1 \times \hat{z}) \times \overline{r}_1|^3}\right\}, \tag{E.5}$$

$$a_{z\gamma} = \frac{\beta(1-\mu)\cos^2\alpha}{r_1^2}\left\{-\frac{\sin\alpha\sin\gamma(y^2+(x+\mu)^2)}{|(\overline{r}_1 \times \hat{z}) \times \overline{r}_1|^3}\right\}. \tag{E.6}$$